

4-2021

## DEVELOPMENT OF PIEZOELECTRIC ENERGY HARVESTING SYSTEM FOR LOW-FREQUENCY VIBRATIONS

Mai Rabie Mahmoud Ismail

Follow this and additional works at: [https://scholarworks.uaeu.ac.ae/all\\_theses](https://scholarworks.uaeu.ac.ae/all_theses)



Part of the [Mechanical Engineering Commons](#)

---

### Recommended Citation

Mahmoud Ismail, Mai Rabie, "DEVELOPMENT OF PIEZOELECTRIC ENERGY HARVESTING SYSTEM FOR LOW-FREQUENCY VIBRATIONS" (2021). *Theses*. 816.

[https://scholarworks.uaeu.ac.ae/all\\_theses/816](https://scholarworks.uaeu.ac.ae/all_theses/816)

This Thesis is brought to you for free and open access by the Electronic Theses and Dissertations at Scholarworks@UAEU. It has been accepted for inclusion in Theses by an authorized administrator of Scholarworks@UAEU. For more information, please contact [mariam\\_aljaberi@uaeu.ac.ae](mailto:mariam_aljaberi@uaeu.ac.ae).



United Arab Emirates University

College of Engineering

Department of Mechanical Engineering

DEVELOPMENT OF PIEZOELECTRIC ENERGY HARVESTING  
SYSTEM FOR LOW FREQUENCY VIBRATIONS

Mai Rabie Mahmoud Ismail

This thesis is submitted in partial fulfilment of the requirements for the degree of  
Master of Science in Mechanical Engineering

Under the Supervision of Dr. Farag K. Omar

April 2021

### Declaration of Original Work

I, Mai Rabie Mahmoud Ismail, the undersigned, a graduate student at the United Arab Emirates University (UAEU), and the author of this thesis entitled “*Development of Piezoelectric Energy Harvesting System for Low Frequency Vibrations*”, hereby, solemnly declare that this thesis is my own original research work that has been done and prepared by me under the supervision of Dr. Farag K. Omar in the College of Engineering at UAEU. This work has not previously been presented or published, or formed the basis for the award of any academic degree, diploma or a similar title at this or any other university. Any materials borrowed from other sources (whether published or unpublished) and relied upon or included in my thesis have been properly cited and acknowledged in accordance with appropriate academic conventions. I further declare that there is no potential conflict of interest with respect to the research, data collection, authorship, presentation and/or publication of this thesis.

Student's Signature:     *Mai Rabie Ismail*                          Date:     30/5/2021

Copyright © 2021 Mai Rabie Mahmoud Ismail  
All Rights Reserved



## **Advisory Committee**

1) Advisor: Dr. Farag K. Omar

Title: Associate Professor

Department of Mechanical Engineering

College of Engineering

2) Co-advisor: Dr. Rafic Ajaj

Title: Assistant Professor

Department of Aerospace Engineering

College of Engineering

Khalifa University of Science, Technology and Research, UAE

## Approval of the Master Thesis


This Master Thesis is approved by the following Examining Committee Members:

1. Advisor (Committee Chair): Dr. Farag K. Omar

Title: Associate Professor

Department of Mechanical Engineering

College of Engineering

Signature 


Date 25-4-2021

2. Member: Dr. Tariq Darabseh

Title: Associate Professor

Department of Mechanical Engineering

College of Engineering

Signature 

Date 25/4/2021


- 3) Member (External Examiner): Dr. Peter Glynne-Jones

Title: Associate Professor

Department of Mechanical Engineering

Institution: University of Southampton, United Kingdom

on behalf of external examiner

Signature 

Date 25/4/2021

This Master Thesis is accepted by:

Dean of the College of Engineering: Professor James Klausner

Signature James F. Klausner Date 18/6/2021

Dean of the College of Graduate Studies: Professor Ali Al-Marzouqi

Signature Ali Hassan Date 18/6/2021

Copy \_\_\_\_ of \_\_\_\_

## Abstract

Harvesting energy from vibration sources has attracted the interest of researchers for the past three decades. Researchers have been working on the potential of achieving self-powered MEMS scale devices. Piezoelectric cantilever harvesters have caught the attention in this field because of the excellent combination of high-power density and compact structure. The main objective of this thesis is to develop a novel and optimum piezoelectric harvester system using lumped parameter model (LPM) for given vibration sources. Finite element model (FEM) is used in this work as an original approach to be utilized for optimal design optimization. Three types of validations are accomplished to solidify the use of FEM in mimicking the distributed parameter model (DPM) for linearly tapered piezoelectric cantilevers. The first two validations are accomplished using beam deflection and relative transmissibility functions. Comparisons between the FEM and the DPM developed by the literature are performed. The third validation is carried for an electromechanical piezoelectric cantilever in FEM. Results confirmed the effectiveness of the developed FEM. Number of significant contributions are achieved while fulfilling the aim of this work. First, a dimensionless parameter, Power Factor (PF), is derived and used to understand the impact of the geometry on the piezoelectric harvester performance. The PF showed an optimum performance at a taper ratio of 0, taking the full length of the cantilever and thickness ratio of 0.7. Second, the accuracy of the LPM for linearly tapered piezoelectric harvesters and optimal design are investigated. Results indicated that the percentage of the deflection error between the LPM and the FEM reaches 9% when the taper ratio is zero. However, when tip-mass to cantilever ratios are larger than 2, the error decreases to less than 0.5% leading to more accurate results in the vibrational response of the beam. Further studies on the accuracy are accomplished using the relative transmissibility function. Results showed that as the taper ratio decreases towards zero, the percentage error of using the LPM to predict the vibration response increases significantly to 55%. These results lay the foundation for the third contribution of developing correction factors for tapered and optimal piezoelectric cantilever harvesters using FEM. Comparisons of the corrected LPM and FEM for different configurations are examined. Results indicated that as the taper ratio decreases, the surface power density increases. However, the developed optimal

design exhibits the highest surface power density of  $1.40 \times 10^4$  [(mW/g<sup>2</sup>)/ m<sup>2</sup>] which is 16.4% more than the best following shape of a taper ratio 0.2 and 58% more than the taper ratio 1. Furthermore, a parametric study of the optimal design is performed to scrutinize the effect of various parameters on the harvester performance. Finally, detailed criteria for designing the optimal piezoelectric harvester for different conditions are structured.

**Keywords:** Energy harvesting, optimal piezoelectric harvester, correction factor, lumped parameter model, finite element model, analytical analysis.

## Title and Abstract (in Arabic)

### تطوير نظام حصاد الطاقة الكهروضغية للاهتزازات منخفضة التردد

#### الملخص

جذب حصاد الطاقة من مصادر الاهتزاز اهتمام الباحثين على مدار العقود الثلاثة الماضية. عمل الباحثون على إمكانية تحقيق أجهزة استشعار كهروميكانيكية دقيقة (MEMS) ذاتية قوة التشغيل. جذبت "حاصدات الكابول الكهروضغية" الانتباه في هذا المجال بسبب تركيبها الممتاز الذي يجمع بين كثافة الطاقة العالية والهيكل المدمج. الهدف الرئيسي من هذه الأطروحة هو تطوير نظام حاصدة كهروضغية جديد ومثالي باستخدام نموذج المعلمة المجمع (LPM) لمصادر اهتزاز معينة. تم استخدام نموذج العناصر المحدودة (FEM) في هذا البحث ليساهم في تطوير التصميم للشكل الأمثل. وبهذا الصدد أُنجرت ثلاثة أنواع من عمليات التحقق لترسيخ استخدام نموذج FEM في محاكاة نموذج المعلمة الموزعة (DPM) لحاصدات الكابول الكهروضغية المستدقة طولياً. تم إجراء عمليتي التحقق الأولى والثانية باستخدام دالة انحراف العارض و دالة النقل النسبية. تم إجراء مقارنات بين في نموذج FEM و نموذج DPM التي طورتهما الأبحاث السابقة. كما تم إجراء التحقق الثالث باستخدام الخصائص الكهروميكانيكية لحاصدات الكابول الكهروضغية في نموذج FEM. أكدت نتائج التحققات الثلاث فعالية نموذج FEM المطور. تم تحقيق هدف هذا البحث عبر مجموعة من المساهمات الهامة. أولاً، تم اشتقاق مقياس بلا أبعاد يسمى بمعامل القدرة (PF) واستخدامه لفهم تأثير التكوين الجيوميتري على أداء الحاصدة الكهروضغية. أظهر PF الأداء الأمثل عند نسبة استدقاق 0 أخذين في عين الاعتبار الطول الكلي للكابول ونسبة سماكة قدرها 0.7. ثانياً، تم الفحص والكشف عن درجة الدقة لنموذج LPM للحاصدات الكهروضغية مستدقة الطرف بالإضافة إلى الحاصدة ذات التصميم الأمثل. أشارت النتائج إلى أن نسبة خطأ الانحراف بين LPM و FEM تصل إلى 9% عندما تكون نسبة الاستدقاق 0. ولكن، عندما تكون نسب الكتلة إلى الكابول أكبر من 2، ينخفض الخطأ إلى أقل من 0.5% مما يؤدي إلى نتائج أكثر دقة في الاستجابة الاهتزازية للكابول. تم إجراء المزيد من الدراسات حول دقة النموذج LPM باستخدام دالة النقل النسبية، حيث أظهرت النتائج أنه مع انخفاض نسبة الاستدقاق نحو 0، فإن النسبة المئوية للخطأ في استخدام LPM للتنبؤ باستجابة الاهتزاز تزداد بشكل كبير إلى 55%. تضع هذه النتائج الأساس للمساهمة الثالثة لتطوير عامل تصحيح لحاصدات الكابول الكهروضغية المدببة طولياً وكذلك الحاصدات ذات التصميم الأمثل باستخدام FEM. تم عمل مقارنات بين نموذج المعلمة المجمع المصحح C-LPM و FEM لأشكال وتكوينات هندسية مختلفة، وأشارت النتائج إلى أنه مع انخفاض نسبة الاستدقاق، تزداد كثافة قدرة/طاقة السطح. مع ذلك، يُظهر التصميم الأمثل المطور أعلى كثافة طاقة سطحية بلغت  $1.40 \times 10^4$  [ميغاواط/جرام<sup>2</sup>/م<sup>2</sup>] والتي تزيد بنسبة 16.4% عن أفضل

شكل تالي بنسبة استدقاق 0.2 و 58% أكثر عن الشكل الذي نسبة استدقاقه 1. علاوة على ذلك ، تم إجراء دراسة بارامترية للتصميم الأمثل لفحص تأثير العوامل المختلفة على أداء الحاصد. أخيرًا ، تم وضع معايير تفصيلية لتصميم الحصادات الكهروإجهادية الأمثل لظروف مختلفة.

**مفاهيم البحث الرئيسية:** حصاد الطاقة، حاصد الطاقة الكهروضغطية المثالي، عامل تصحيح، نموذج المعلمة المجمعة، نموذج العناصر المحدودة، التحليل النظري.

## **Acknowledgements**

I am indebted to show and convey my acknowledgement to all who supported me to achieve this master thesis. I would like to express my gratitude to my main advisor, Dr. Farag Omar, for his immense knowledge, insightful comments and patience during the master period. I extend my special thanks to my co-advisor, Dr. Rafic Ajaj, whose creative ideas and great suggestions enriched this work significantly. This work would not have been accomplished without their continuous support and guidance. It was indeed a privilege to work under their supervision. I would also like to thank the engineers who are working in the mechanical labs for their assistance in building my experimental setup. This master work was performed and funded within the framework of UAEU/SQU joint research project grant.

I would like to give my sincere gratitude to Dr. Filippo Genco who believed in me and enlightened my educational path with his valuable guidance.

I wish to express my appreciation to all my friends. I would like to especially thank my beloved childhood friends: Marah Omar, Nora Almansoori, Maha Elsiwy and Hedaia Mujahed for their precious friendship, immeasurable support and understanding during this journey. I can't express how thankful I am to my best friend, Eng. Doaa Al-Yafeai, for being a great friend and a true supporter, and for the priceless memories that we shared throughout the master years.

My genuine love and deepest gratitude to my family, who have been the first and forever supporters and motivators in my life. To my parents, thank you for all the love, sacrifices, and perpetual encouragement that you have done for me to be the person who I am today. My sister, Fatin and my brother, Mustafa, thank you for being the best caring and loving siblings. I am blessed to have such a wonderful family.



## **Dedication**

*To my lovely parents,  
For their infinite love, compassion and support*

## Table of Contents

Title .....	i
Declaration of Original Work .....	ii
Copyright .....	iii
Advisory Committee .....	iv
Approval of the Master Thesis .....	v
Abstract .....	vii
Title and Abstract (in Arabic) .....	ix
Acknowledgements .....	xi
Dedication .....	xii
Table of Contents .....	xiii
List of Tables .....	xvi
List of Figures .....	xvii
List of Abbreviations .....	xxi
Chapter 1: Introduction .....	1
1.1 Motivation.....	1
1.2 Problem statement.....	2
1.3 Objectives .....	5
1.4 Methodology .....	5
1.5 Thesis structure .....	6
Chapter 2: Literature Review .....	8
2.1 Energy harvesting from ambient sources.....	8
2.2 Vibration energy harvesting.....	11
2.2.1 Vibration energy harvesting transductions.....	12
2.3 Fundamentals of piezoelectric harvesters .....	16
2.3.1 Modes of piezoelectric harvesters .....	18
2.3.2 Piezoelectric material .....	23
2.3.3 Piezoelectric configurations .....	26
2.4 Modeling of piezoelectric cantilever beam.....	30
2.5 Design optimization of piezoelectric cantilever beam.....	32
2.6 Electric circuit of piezoelectric energy harvesting system .....	40
2.7 Application of piezoelectric energy harvesters.....	43
2.7.1 Energy harvested from human body .....	44
2.7.2 Energy harvested from infrastructure and automobiles .....	49
2.7.3 Energy harvested from environmental sources .....	51
Chapter 3: Mathematical Model.....	53

3.1 LPM for linearly tapered piezoelectric cantilever .....	54
3.1.1 Electromechanical coupling .....	57
3.1.2 Static deflection and equivalent stiffness $K_{eq}$ .....	61
3.1.3 Equivalent mass $M_{eq}$ .....	63
3.1.4 Equivalent damping $C_{eq}$ .....	66
3.1.5 Natural frequency $\omega_n$ .....	67
3.2 Electric circuit .....	67
3.3 Power factor .....	68
3.4 Relative transmissibility function of the piezoelectric cantilever harvester models .....	71
3.4.1 Rectangular piezoelectric cantilever harvesters .....	71
Chapter 4: Experimental Setup .....	75
4.1 Experimental process .....	75
4.2 Piezoelectric cantilever beam setup .....	77
4.3 Data acquisition system (DAQ) .....	79
4.4 Validation using experimental analysis .....	79
Chapter 5: Finite Element Analysis (FEA) .....	83
5.1 Mechanical modeling .....	83
5.2 Electromechanical modeling .....	86
5.3 Validation of the FEM .....	92
5.3.1 Validation using beam deflection .....	92
5.3.2 Validation using beam relative transmissibility function .....	94
5.3.3 Validation using integrated piezoelectric cantilever beam in FEM .....	95
Chapter 6: Design Optimization and Modeling of a Piezoelectric Harvester; Results and Discussions .....	98
6.1 The development of an optimal piezoelectric harvester design .....	98
6.1.1 Design optimization .....	99
6.1.2 FEM verification of the optimal piezoelectric harvester design .....	105
6.2 The accuracy of modeling tapered piezoelectric harvester using LPM .....	106
6.2.1 The accuracy of the LPM for linearly tapered piezoelectric cantilever .....	107
6.2.2 The accuracy of the LPM for optimal piezoelectric cantilever (irregular shape) .....	111
6.3 The development of correction factor for the LPM of tapered piezoelectric harvester .....	113
6.3.1 Correction factor of linearly tapered piezoelectric cantilever .....	114
6.3.2 Correction factor of optimal piezoelectric cantilever (irregular shape) .....	123

6.4 Verification of the C-LPM for an electromechanical piezoelectric harvester .....	126
6.4.1 Verification of the integrated linearly tapered piezoelectric harvester in FEM.....	126
6.4.2 Verification of the integrated optimal tapered piezoelectric harvester in FEM.....	130
6.5 Parametric study on optimal piezoelectric harvester .....	133
6.5.1 Load resistance effect.....	134
6.5.2 Tip mass ratios effect .....	138
6.5.3 Piezoelectric material effect .....	141
6.6 Design criteria and limitations of the optimal piezoelectric harvester.....	143
Chapter 7: Conclusion and Recommendations .....	148
7.1 Conclusion .....	148
7.2 Recommendations for future research .....	151
References .....	153
List of Publications .....	176

## List of Tables

Table 1: Comparison of the available energy harvesting sources.....	10
Table 2: Frequency and acceleration of different vibration sources.....	12
Table 3: Advantages and disadvantages of different energy harvesting transductions .....	14
Table 4: Advantages and disadvantages of material types used in piezoelectric harvesters.....	23
Table 5: Properties of piezoelectric materials .....	26
Table 6: Comparison between application usage of piezoelectric ceramics and polymers.....	26
Table 7: Geometrical and material properties of PZT-5H bimorph cantilever used in the experiment .....	78
Table 8: Mechanical properties of piezoelectric cantilever beam used in simulation.....	86
Table 9: Geometric specifications of piezoelectric cantilever beam used in simulation.....	86
Table 10: Material properties of piezoelectric harvester in FEM .....	88
Table 11: Electromechanical properties used in ANSYS for piezoelectric materials.....	91
Table 12: Material and geometrical parameters of a piezoelectric cantilever harvester.....	100
Table 13: Natural frequency of LPM and FEM with the corresponding error between the two models .....	118
Table 14: Correction factor for the fundamental vibration mode of linearly tapered piezoelectric beams subjected to different mass ratios.....	120
Table 15: Correction factor for the fundamental vibration mode of the optimal design subjected to different mass ratios.....	125
Table 16: Error of FEM and C-LPM frequencies for optimal design with load resistance of 470 k $\Omega$ subjected to different tip mass ratios .....	132
Table 17: Properties of different piezoelectric materials used in the parametric study .....	141
Table 18: Specification of the optimal piezoelectric harvester.....	146

## List of Figures

Figure 1: Power consumption and energy harvesting .....	2
Figure 2: Energy harvesting sources available in the environment .....	9
Figure 3: Number of publications of different vibration energy harvesting transductions between year 2003 and 2013 .....	15
Figure 4: Different configurations of the piezoelectric cantilever harvester with tip mass .....	16
Figure 5: Direction of index of piezoelectric material element .....	18
Figure 6: Representation of the polarization in $d_{31}$ and $d_{33}$ modes .....	18
Figure 7: Two different electrode patterns for operating modes of piezoelectric harvesters.....	19
Figure 8: Piezoelectric harvester implemented in a car door latch .....	20
Figure 9: Schematic of a shear stress harvester of $d_{15}$ mode .....	21
Figure 10: Representation of $d_{15}$ series structure piezoelectric harvester .....	21
Figure 11: ZnO nanoribbons .....	22
Figure 12: Unimorph and bimorph piezoelectric cantilevers.....	27
Figure 13: Cymbal piezoelectric harvester .....	28
Figure 14: Piezoelectric stack .....	29
Figure 15: Different shapes of piezoelectric harvesters.....	33
Figure 16: Configurations and results of piezoelectric cantilever harvesters .....	34
Figure 17: Linear and quadratic piezoelectric cantilever harvesters.....	35
Figure 18: Stress distribution for rectangular and optimized shapes of piezoelectric harvesters.....	36
Figure 19: Piezoelectric energy harvesters .....	38
Figure 20: Strain distribution of rectangular, trapezoidal and triangular piezoelectric cantilever beams.....	39
Figure 21: Electric circuit diagram of piezoelectric energy harvester .....	40
Figure 22: Conditioning circuits of the piezoelectric cantilever harvester .....	41
Figure 23: Imbedded piezoelectric harvester in shoes .....	45
Figure 24: Insole piezoelectric harvester .....	45
Figure 25: Experimental setup of embedded piezoelectric harvester in a shoes .....	46
Figure 26: Knee joint piezoelectric harvester .....	47
Figure 27: Piezoelectric backpack harvester.....	48
Figure 28: Implementable piezoelectric harvester in the heart .....	49
Figure 29: Piezoelectric roadway harvester .....	50
Figure 30: Ocean energy piezoelectric harvester setup.....	52
Figure 31: Bimorph piezoelectric cantilever harvester with tip mass and its corresponding mass spring damper model representation.....	54
Figure 32: LPM of a piezoelectric cantilever harvester .....	54
Figure 33: A schematic of a piezoelectric element .....	58

Figure 34: Electric circuit schematics of the piezoelectric harvester.....	67
Figure 35: Experimental setup of the piezoelectric cantilever harvester .....	75
Figure 36: Process flow diagram of experimental piezoelectric energy harvesting.....	76
Figure 37: Close-up picture of piezoelectric cantilever harvester setup attached to a shaker.....	77
Figure 38: PZT-5H bimorph piezoelectric cantilever and its corresponding dimensions from the factory .....	78
Figure 39: A screenshot of LABVIEW software.....	79
Figure 40: Input peak-peak acceleration of 1g used in the experiment .....	80
Figure 41: Logarithmic decrement function of rectangular piezoelectric cantilever .....	81
Figure 42: Voltage response to base acceleration of rectangular piezoelectric cantilever with damping ratio 0.011 .....	81
Figure 43: Analytical and experimental results of rectangular piezoelectric cantilever under open circuit conditions.....	82
Figure 44: FEM of linearly tapered piezoelectric cantilever beam with tip mass .....	84
Figure 45: Electromechanical coupling of a tapered piezoelectric cantilever harvester FEM .....	87
Figure 46: Meshing of tapered piezoelectric beam in ANSYS.....	89
Figure 47: Modes of a tapered piezoelectric cantilever harvester using FE .....	90
Figure 48: Normalized deflection of EFM and DPM for rectangular piezoelectric cantilever beam with different tip mass ratios of $a = 0, 0.5, 2$ and $5$ .....	93
Figure 49: Normalized deflection of FEM and DPM for different tapered piezoelectric cantilever beams of $r = 1, 0.8, 0.6, 0.4, 0.2$ and $0$ with no tip mass.....	94
Figure 50: Relative transmissibility functions of DPM and FEM for transverse rectangular piezoelectric cantilever beam with no tip mass .....	95
Figure 51: Comparison between the developed FEM and the peak results of DPM and experimental measurements taken from [19] for $R = 33 \text{ k}\Omega$ .....	96
Figure 52: Comparison between the developed FEM and the peak results of DPM and experimental measurements taken from [19] for $R = 470 \text{ k}\Omega$ .....	97
Figure 53: 3D plot of the power factor (PF) for different taper ratios and aspect ratios of a bimorph piezoelectric beam.....	101
Figure 54: Schematic of a piezoelectric cantilever beam with a middle section.....	101
Figure 55: 3D plot of power factor for different middle point positions of a bimorph piezoelectric beam.....	102

Figure 56: 3D plot of power factor for different thickness ratios and taper ratios of a bimorph piezoelectric beam.....	103
Figure 57: Schematic of different configurations of piezoelectric cantilevers harvesters .....	103
Figure 58: Normalized stress of different taper ratios and optimal design of the piezoelectric cantilever beam .....	105
Figure 59: Surface power density for different geometrical designs of piezoelectric cantilever harvester with load resistance of 470 k $\Omega$ using FEM .....	106
Figure 60: Comparison between the normalized deflection of the FEM and the LPM for different tapered piezoelectric cantilevers .....	108
Figure 61: Percentage error of the normalized deflection of a triangular piezoelectric cantilever beam ( $r = 0$ ) with no tip mass .....	109
Figure 62: Maximum percentage error of the normalized deflection of different tapered piezoelectric cantilever beams with no tip mass.....	110
Figure 63: The maximum percentage error of the normalized deflection of different tapered piezoelectric cantilever beams with different tip mass ratios .....	111
Figure 64: Comparison between the normalized deflection of the FEM and the LPM for the optimal piezoelectric cantilever design.....	112
Figure 65: Percentage error of the normalized deflection for the optimal piezoelectric cantilever beam with no tip mass .....	112
Figure 66: The maximum percentage error of the normalized deflection of the optimal piezoelectric cantilever subjected to different tip mass ratios .....	113
Figure 67: Relative tip displacement transmissibility function of the LPM for linearly tapered piezoelectric cantilever beam with no tip mass .....	114
Figure 68: Relative tip displacement transmissibility function of the FEM for different tapered piezoelectric cantilever beams with no tip mass .....	116
Figure 69: Relative error of LPM for different linearly tapered ratios of a piezoelectric cantilever beam with no tip mass given for $\zeta = 0.01$ .....	118
Figure 70: Correction factor for the first mode of different linearly tapered piezoelectric ratios subjected to different mass ratios .....	119
Figure 71: Relative tip displacement transmissibility functions obtained from FEM, C-LPM and LPM for different taper ratios for given $\zeta = 0.01$ .....	122
Figure 72: Relative tip displacement transmissibility function for the optimal piezoelectric beam with no tip mass.....	123
Figure 73: Relative error of LPM for the optimal piezoelectric cantilever beam with no tip mass for $\zeta = 0.01$ .....	124



Figure 74: Correction factor of the optimal design for different tip mass ratios developed by FEM.....	125
Figure 75: Relative tip displacement transmissibility functions obtained from FEM, C-LPM and LPM for the optimal piezoelectric cantilever design given $\zeta = 0.01$ .....	126
Figure 76: Comparison between C-LPM and FEM for rectangular piezoelectric beam ( $r = 1$ ) with load resistance of 470 k $\Omega$ .....	127
Figure 77: Comparison between C-LPM and FEM for tapered piezoelectric beam of ratio ( $r = 0.8$ ) with load resistance of 470 k $\Omega$ .....	128
Figure 78: Comparison between C-LPM and FEM for tapered piezoelectric beam of ratio ( $r = 0.6$ ) with load resistance of 470 k $\Omega$ .....	128
Figure 79: Comparison between C-LPM and FEM for tapered piezoelectric beam of ratio ( $r = 0.4$ ) with load resistance of 470 k $\Omega$ .....	129
Figure 80: Comparison between C-LPM and FEM for tapered piezoelectric beam of ratio ( $r = 0.2$ ) with load resistance of 470 k $\Omega$ .....	130
Figure 81: Comparison between C-LPM and FEM for optimal design with load resistance of 470 k $\Omega$ .....	131
Figure 82: Comparison between voltage output of FEM and C-LPM for optimal design with load resistance of 470 k $\Omega$ subjected to different tip mass ratios .....	132
Figure 83: FRF of optimal design with different load resistance magnitudes for damping ratio of $\zeta = 0.027$ and tip mass $Mt = 0.012$ kg.....	134
Figure 84: FRF of the optimal design with different load resistance magnitudes for damping ratio of $\zeta = 0.027$ and tip mass $Mt = 0.012$ kg .....	135
Figure 85: FRF of the optimal design with load resistance for short and open circuit resonance frequencies.....	137
Figure 86: FRF of the optimal piezoelectric cantilever design with tip mass of $Mt = 0.012$ at $R_{opt}$ .....	138
Figure 87: FRF of optimal design subjected to different tip mass ratios at $R_{opt}$ .....	140
Figure 88: FRF of the optimal design for three different piezoelectric materials with tip mass $Mt = 0.012$ at load resistance of 470 k $\Omega$ .....	142
Figure 89: FRF of the optimal design of three different piezoelectric materials with tip mass $Mt = 0.012$ at $R_{opt}$ .....	143
Figure 90: Surface power density for different aspect ratios of the optimal design for a given vibration source.....	145
Figure 91: Tip mass thickness for different aspect ratios of the optimal design.....	146
Figure 92: FRF of optimal piezoelectric harvester with tip mass $Mt = 0.0056$ kg .....	147
Figure 93: Stress and strain of the optimal piezoelectric harvester with tip mass $Mt = 0.0056$ kg .....	147

## List of Abbreviations

AC	Alternating Current
BC	Boundary Condition
CF	Correction Factor
C-LPM	Corrected Lumped Parameter Model
DAQ	Data Acquisition System
DC	Direct Current
DPM	Distributed Parameter Model
DSSH	Double Synchronized Switch Harvesting
FBD	Free Body Diagram
FEA	Finite Element Analysis
FEM	Finite Element Model
FRF	Frequency Response Function
IDE	Interdigitated Electrode
LPM	Lumped Parameter Model
MEMS	Micro Electromechanical Systems
PF	Power Factor
PMN-PT	Lead Magnesium Niobate- Lead Titanate
PVDF	Polyvinylidene Fluoride
PZT	Lead Zirconate Titanate
PZT-PT	Lead Zirconate Niobate- Lead Titanate
RF	Radio Frequency
RFID	Radio Frequency Identification

RMS	Root Mean Square
RMSHI	Random Mechanical Switching Harvesting on Inductor
SDOF	Single Degree of Freedom
SECE	Synchronized Electric Charge Extraction
SSHI	Synchronized Switch Harvesting on Inductor
SSPB	Single Supply Pre-Biasing Circuit
TBE	Top and Bottom Electrodes
TWh	Tera Watt Hour
ZnO	Zinc Oxide
$A$	Surface Area ( $m^2$ )
$a$	Tip Mass Ratio
$a_r$	Aspect Ratio
$b(x)$	Width Function (m)
$C$	Damping Coefficient (N.s/m)
$c$	Elastic Stiffness Coefficient
$C_p$	Piezoelectric Capacitor (F)
$D$	Electrical Displacement ( $C/m^2$ )
$d_{31}$	Piezoelectric Coefficient (m/V) or (C/N)
$E$	Young's Modulus of Elasticity ( $N/m^2$ )
$E_3$	Electric Field in the Z direction (N/C)
$EI(x)$	Bending Stiffness ( $N.m^2$ )
$F$	Force (N)
$G$	Amplification Factor
$h$	Thickness (m)

$I$	Moment of Inertia ( $\text{kg.m}^2$ )
$i$	Current (A)
$K$	Stiffness (N/m)
$KE$	Kinetic Energy ( $\text{kg.m}^2 / \text{s}^2$ ) Or (J)
$l$	Length of the Piezoelectric Cantilever Beam (m)
$M$	Bending Moment (N.m)
$M_{eq}$	Equivalent Mass (kg)
$M_t$	Tip Mass (kg)
$m$	Beam Mass Per Unit Length (kg/m)
$m_b$	Equivalent Beam Mass (kg)
$P$	Power (W)
$Q$	Electric Charge (C)
$R$	Resistor ( $\Omega$ )
$r$	Taper Ratio
$S$	Mechanical Strain (m/m)
$s$	Elastic Compliance Coefficient ( $\text{m}^2/\text{N}$ )
$T$	Transmissibility Function
$\hat{T}$	Reduced Transmissibility Function
$t_p$	Thickness Ratio
$V$	Voltage (V)
$v$	Velocity (m/s)
$Y_0$	Base Displacement Amplitude (m)
$y_m$	Absolute Displacement of the Mass (m)
$y(t)$	Harmonic Base Displacement (m)

$y(x)$	Deflection at Any Section of the Beam (m)
$z$	Relative Tip Displacement (m)
$\alpha$	Electromechanical Coupling (C/N)
$\delta$	Delta
$e$	Piezoelectric Coefficient (C/m)
$\epsilon_{33}$	Permittivity (F/m)
$\zeta$	Damping Ratio
$\theta$	Slope of the Free Vibration
$\lambda$	Dimensionless Frequency Parameter
$\mu$	Correction Factor of the Rectangular Piezoelectric Cantilever
$\rho$	Density (kg/m <sup>3</sup> )
$\sigma$	Mechanical Stress (N/m <sup>2</sup> )
$\phi$	Eigenfunction
$\Omega$	Normalized Frequency
$\omega$	Excitation Frequency (Hz)
$\omega_n$	Fundamental Natural Frequency of the Cantilever (Hz)
$\omega_r$	Undamped Natural Frequency (Hz)

## Superscripts:

$DPM$	Distributed Parameter Model
$LPM$	Lumped Parameter Model
$S$	Strain
$T$	Stress

## Subscripts:

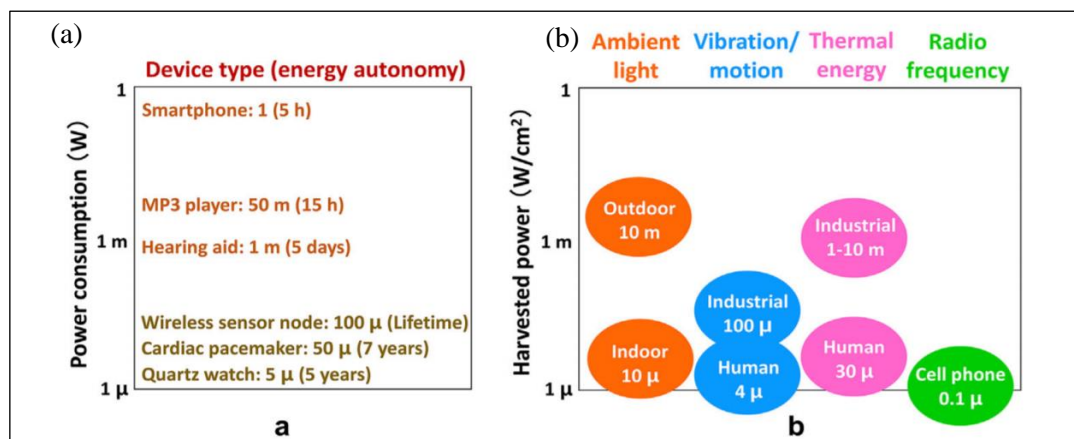
0	Beam base
---	-----------

<i>abs</i>	Absolute
<i>avg</i>	Average
<i>b</i>	Beam
<i>Eq</i>	Equivalent
<i>l</i>	Beam Tip
<i>m</i>	Middle Section
<i>n</i>	Normalized
<i>opt</i>	Optimal
<i>p</i>	Piezoelectric
<i>r</i>	rth Mode Shape
<i>rel</i>	Relative
<i>rms</i>	Root Mean Square
<i>tot</i>	Total

## Chapter 1: Introduction

### 1.1 Motivation

Energy has always been the fundamental key of civilization around the world. Global energy demand has increased dramatically in the last decade. According to the world energy statistics, the primary energy consumption in 2018 has seen a surge at a rate of 2.9% which is the fastest and the highest growth since 2010 [1]. Electricity power consumption increased as well by 3.5% in 2018. In vast growing countries like the United Arab Emirates, electricity consumption has grown rapidly from 38 TWh in 2000 to 118 TWh in 2019 [1]. Thus, governments worldwide invested in research and development to harvest energy from alternative sources other than conventional sources like fossil fuels. The three primary available energy sources are non-renewable sources, nuclear sources and renewable sources. Non-renewable energy sources include oil, coal and natural gas. Renewable energy sources have shown great potential lately. In 2019, 27% of the electricity production around the world was produced using renewable energy technologies [2]. The most known types of renewable energy systems are solar energy, wind energy, biomass energy, geothermal energy and hydropower energy [3]. However, harvesting energy from vibration sources is considered to be one of the hot research topics of sustainable energy over the past three decades. The power produced by different sustainable ambient energy sources varies from 1  $\mu$ W to 1 W power output, as shown in Figure 1(b) [4]. This wide-ranging harvested energy is utilized based on the power need and the size limitation of applications in the industry. For example, Figure 1(a) clarifies the power consumption of different battery-based devices which mostly consume power in the range of  $\mu$ W~mW. Thus, the best candidate for such types of devices is vibration energy harvesters.



(a) Power consumption of different devices

(b) Harvested power from different ambient energy harvesting sources

Figure 1: Power consumption and energy harvesting. Reproduced with permission from [4], © WILEY-VCH Verlag GmbH & Co., 2017.

Different mechanisms were developed in order to capture the energy from vibration and turn it to useful electrical output. Piezoelectric energy harvesters are the most efficient vibration energy harvesters due to their high energy conversion compared to other mechanisms [5]. The great properties of piezoelectric harvesters as well as the easy system fabrication and the ability to implement them in size restricted areas give the researchers a very solid and wide area of application [6], [7].

## 1.2 Problem statement

MEMS have shown great potential in many applications like monitoring in health and industrial sectors. However, the use of batteries in powering MEMS had limited their capacity. Hazardous risks, high maintenance cost and limited lifetime are some of the serious issues associated with using batteries in MEMS [8]. The idea of powering MEMS through piezoelectric harvesters has caught great attention in the



field. Self-powered MEMS devices have the ability to be implemented in remote and critical environments with low cost and high reliability.

Modeling the piezoelectric harvester constitutes the primary step towards understanding the dynamics behavior of this vibration energy scavenger. The early efforts in modeling the piezoelectric harvesters used the single degree of freedom (SDOF) lumped parameter model (LPM) [5], [9], [10]. The simple form of the lumped parameters gave an initial idea of the mechanical performance of piezoelectric harvesters. However, researchers investigated the ability of this model to precisely describe the dynamic behavior of the harvester. Several limitations in using the LPM were stated by Erturk et al. [11], some of which are crucially critical that it can affect the power assumption generated by the piezoelectric harvester. Problems in LPM include ignoring the electromechanical coupling, predicting exclusively the first mode and not taking strain distribution into consideration [11]. This had urged the researchers to develop a distributed parameter model (DPM) using the Rayleigh-Ritz discretization method for more accurate results [12], [13]. Further progress was done to derive an exact analytical solution for piezoelectric harvesters using Euler-Bernoulli beam theory [14]–[16]. Erturk et al. then stated all the issues associated with the attempts of developing a piezoelectric harvester model [17]. Later Erturk et al. developed an exact analytical solution for unimorph and bimorph piezoelectric harvester using DPM which represented the vibration dynamics precisely [18], [19]. However, the fact that much of the literature work was based on the LPM had led Erturk et al. to develop a correction factor for the LPM for better accuracy in power prediction [11].

Scientists have explored many different approaches to improve the performance of piezoelectric harvesters for better efficiency and higher power production. The Literature highlighted three main aspects in increasing the power generation of piezoelectric harvesters: material enhancement [20]–[22], electric circuits development [23]–[25] and configuration and design improvement [8], [26]. The configuration of piezoelectric harvesters affects the electrical output greatly. Piezoelectric cantilever beams are one of the most used configurations in the literature. Studies proposed a lot of creative and innovative designs which amplified the power production of the piezoelectric harvesters.

The aforementioned studies showed a great improvement in modeling and increasing the performance of piezoelectric cantilever harvesters. However, this thesis work aims to fill some important gaps where the literature lacked to investigate it clearly. The main contributions of this work can be summarized as follows: First, design an optimum scalable piezoelectric harvester based on a developed comparison parameter. Second, investigate the error of using the LPM in linearly tapered piezoelectric harvesters. Third, implement new approaches like finite element model (FEM) to improve the LPM accuracy. Fourth, develop a correction factor for different configurations other than the rectangular shape. Fifth, perform a parametric study to understand the effect of different parameters on the developed optimal design. Finally, build full and detailed criteria for designing the optimal piezoelectric harvester for different conditions.

### **1.3 Objectives**

The core objective of this thesis is to develop a novel and optimum piezoelectric harvester system using lumped parameter model (LPM) for a given source of vibration. The following are the main goals of the work:

- Conduct a comprehensive system-level analysis to obtain optimal configuration for the piezoelectric harvester system. The analysis will involve design, modeling and optimization studies.
- Assess the performance of the novel piezoelectric harvesting system at different given conditions.
- Structure complete criteria to build the best piezoelectric harvester for any chosen frequency input or desired power output.

### **1.4 Methodology**

The above objectives are accomplished by applying comprehensive, engineering-based procedures. The methodology of this thesis work included conducting a literature review of relevant research and sources of information relevant to the different aspects highlighted in the objectives above. After critically reviewing the collected relevant literature, appropriate methods and concepts are studied to finalize the right transduction method for the right frequency vibration. Modeling the mechanical configuration is developed along with choosing the right piezoelectric material and geometrical parameters for the optimum power output. The next step is building a simulation model using MATLAB for the chosen design based on the developed model. FEM is then integrated in the study to solidify the work outcome. Validations of the analytical and FEM models are then accomplished. Further

verification using an experimental test of the electromechanical model is done in the lab. The accuracy of the LPM for different configurations of the piezoelectric cantilever harvester is then carried. Based on the investigated results of the accuracy study, correction factors of the LPM are developed. A parametric study is performed as well to set the criteria for an optimal piezoelectric harvester working under different conditions. Results are presented and critically discussed. Conclusions and recommendations are drawn based on the conducted study and results.

### **1.5 Thesis structure**

This thesis is divided into seven main chapters. Chapter 1 includes the introduction where the motivation behind this thesis work is stated as well as the objectives, methodology and thesis structure. Chapter 2 is the literature review that encapsulates all the piezoelectric energy harvesters' studies that were done previously on modeling and designing the optimum piezoelectric scavengers. Furthermore, vibration harvesting transductions, piezoelectric fundamentals, electric circuits and applications of piezoelectric harvesters are defined and discussed. A detailed mathematical model of the piezoelectric cantilever beam is available in chapter 3. Chapter 4 presents the experimental setup of the piezoelectric cantilever beam associated with all the geometrical and material specifications used in the experiment. Chapter 5 introduces the FEM analysis used in developing an optimal piezoelectric cantilever beam. It includes all the geometrical and material properties used in modeling the piezoelectric cantilever using different FE programs. Moreover, all the validations of the FEM using space domain and frequency domain are stated in the same. Chapter 6 presents the design optimization process and the modeling of the piezoelectric cantilever harvester. This chapter presents the results and discussions that

signify the primary contributions of the thesis. It consists of six sections that discuss the following: design optimization, modeling accuracy, correction factor, integrated FEM validation, parametric study and design criteria and limitations. Finally, chapter 7 presents the conclusions for this work and the recommendations for future work.

## Chapter 2: Literature Review

### 2.1 Energy harvesting from ambient sources

Numerous researches studied and reviewed different sources that can be used to harvest energy for diverse applications. There are important considerations that should be taken when studying and classifying ambient sources such as: power production, scavengers' mechanism, efficiency and cost. Sources of energy harvesting are divided into four main types which are: RF electromagnetic radiation, sound energy, wind energy and mechanical/vibration energy [27]. Electromagnetic radiation includes light, RF and thermal energies. Light energy can be captured from the sun using solar cells or panels. Power production can reach up to  $100 \text{ mW/cm}^2$  when direct sun is applied to the photovoltaic panel. Another type of electromagnetic radiation is thermal energy where energy can be harvested from the heat available in the environment as well as heat generated from any manmade process. The Thermoelectric effect like Peltier and pyroelectric effects are used in harvesting thermal energy. The efficiency of energy harvested from thermal sources depends on the temperature differences between the source and the environment, in addition to the energy conversion efficiency. However, the main drawback of thermal energy is the low temperature differences which lead to low voltage production and weak energy conversion. Radio frequency (RF) is another source of energy harvesting. RF energy harvesting is to harvest energy from an electromagnetic field and convert it into electrical output. RF energy harvesting is utilized in communications networks like Wifi routers and mobile towers [28]. RF energy has a very low power production of about  $1 \mu\text{W/cm}^2$ . Wind energy is another promising energy harvesting source. It can be harvested using wind turbines. The energy harvested from wind depends mainly on

the speed and direction of the wind. The power produced by harvesting wind energy is about  $177 \mu\text{W}/\text{cm}^2$  [28]. Acoustic noise is available around us in the ambient environment. Thus, sound energy can be extracted and converted into a useful electrical output [29]–[31]. Mechanical energy harvesting has shown great interest from researchers recently. It can be harvested by converting the kinetic energy into valuable electrical output that can be used in many applications. The mechanical energy can be in the form of vibration of any moving structure or working industrial machine as well as body movements and fluid motions. Figure 2 display a deep insight into all the available sources in the environment which can be utilized for power generation [32]. Major and minor division in this chart indicates the volume of power production of each energy harvesting source.

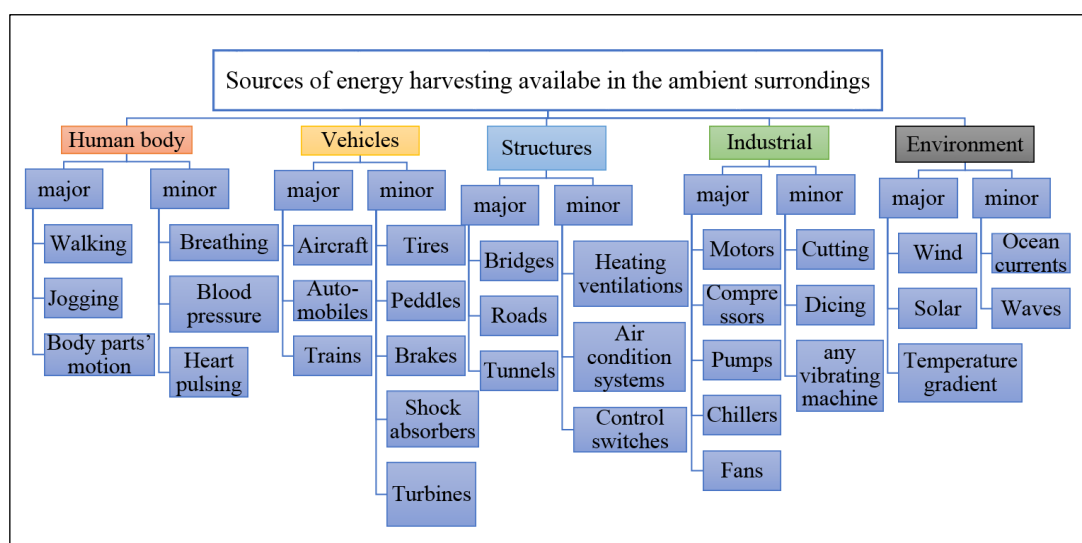


Figure 2: Energy harvesting sources available in the environment

All the discussed energy harvesting sources have been utilized in different applications according to the power energy needed for each application. Table 1 shows a comparison between some of the available energy harvesting sources taken from the literature [28], [33]–[36].

Table 1: Comparison of the available energy harvesting sources [28], [33]–[36]

	Solar energy		Thermal energy		Wind Energy	RF energy	Vibration energy	
	Outdoors	Indoors	Human	Industry			Human	Machine
Power output	100 mW/cm <sup>3</sup>	100 μW/cm <sup>3</sup>	60 μW/cm <sup>2</sup>	10 mW/cm <sup>2</sup>	177 μW/cm <sup>2</sup>	150 μW/m <sup>2</sup>	4 μW/cm <sup>3</sup>	100 μW/cm <sup>3</sup>
Overall efficiency	6% ~ 35%	3% ~ 7%	0.8% ~ 4%	1% ~ 7%	7% ~ 20%	5% ~ 25%	10% ~ 30%	20% ~ 40%
Harvesting method	Photovoltaic cells and panels		Thermoelectric		Wind Turbines	Petch antenna	Piezoelectric/ electrostatic and electromagnetic	
Available time/ condition	Day time 4 ~ 8 Hours		Continuous		Windy times and regions	Continuous	Activity-dependent	
Pros	<ul style="list-style-type: none"> <li>• Large energy production</li> </ul>		<ul style="list-style-type: none"> <li>• Continuous source</li> </ul>		<ul style="list-style-type: none"> <li>• Cost-effective</li> </ul>	<ul style="list-style-type: none"> <li>• Always available</li> </ul>	<ul style="list-style-type: none"> <li>• High power to volume output</li> <li>• Lightweight</li> <li>• Easy installation in devices</li> </ul>	
Cons	<ul style="list-style-type: none"> <li>• Large area for panel installation</li> <li>• Intermittent source of energy</li> </ul>		<ul style="list-style-type: none"> <li>• Requires large area</li> <li>• Low energy production</li> <li>• Rigid and brittle</li> </ul>		<ul style="list-style-type: none"> <li>• Noise pollution</li> <li>• The fatality of birds and bats</li> </ul>	<ul style="list-style-type: none"> <li>• Requires large area</li> </ul>	<ul style="list-style-type: none"> <li>• High variable output</li> </ul>	



## 2.2 Vibration energy harvesting

Vibration is a continuous source of energy that is available everywhere and at any time unlike any other source of energy [37]. Vibration can be harvested effectively from industrial machines, structures like bridges and buildings, automobiles like cars and trains to household appliances such as blenders and fridges. Later, researchers focused on harvesting energy from human body activities like walking, running as well as internal organs activities like breathing and heart pulses. Table 2 shows different vibration sources, their frequencies and amplitude accelerations [7], [34]. The power harvested from vibration sources ranges between  $\mu\text{W}$  to  $\text{mW}$  output.

On the other hand, MEMS applications took great attention from researchers in the last two decades. The traditional way of powering the MEMS devices is through batteries which cause a lot of constraints in the development of these applications. There are major risks associated with using batteries in MEMS devices. One of the main drawbacks is the explosions that might happen due to the high temperatures. Reliability is another main factor in using batteries where failures can be caused because of the long-time batteries used in harsh environments as well as the limitations associated with the short lifetime and low power efficiency [37],[38]. The low power consumption of MEMS devices that acquire  $\mu\text{W}\sim \text{mW}$  power supply gave the vibration energy harvesting sources the potential to replace the high-risk batteries with self-powered MEMS devices. This shift in the MEMS powering system paved the way for different MEMS applications to be used under critical and harsh conditions which were deprived of access when batteries were used earlier.

Table 2: Frequency and acceleration of different vibration sources [7], [34]

Vibration source	Frequency (Hz)	Acceleration amplitude (m/s <sup>2</sup> )
Car instrument panel	13	3
Casing of kitchen blender	121	6.4
Clothes dryer	121	3.5
HVAC vents in an office building	60	0.2-1.5
Car engine compartment	200	12
Refrigerator	240	0.1
Human walking	2-3	2-3
Windows next to a busy road	100	0.7
Second story floor of a busy office	100	0.2

### 2.2.1 Vibration energy harvesting transductions

Energy harvesting from vibration sources requires a mechanism to convert the kinetic energy into electrical energy output. There are four main transductions methods to convert the mechanical vibration from the ambient sources into electrical output: electromagnetic harvesters [39]–[42], electrostatic harvesters [43]–[47], magnetostrictive harvesters [4], [48], [49] and piezoelectric harvesters [50]–[53]. Faraday first discovered the electromagnetic transduction concept in 1830. It is essentially a current produced as a result of moving coil through a magnetic field. The current output can be due to the coil and magnetic movement or the change of magnetic field. An application of this type of transduction is a cantilever beam where the permanent magnet or the coil can be set to be on the cantilever while the other is fixed [45], [54]. Electrostatic harvester's main idea is the use of variable capacitor structures also named varactors. The transducer is a capacitor consists of two plates that are

electrically isolated from each other; the charging of plates by the battery gives an equal opposite charge. The vibration induces a displacement of the charged plates, and then the mechanical energy is converted to an electrical energy because of the relative motion between the two plates. This type of harvester requires a voltage source which is a weak point when comparing it with other harvesting scavengers [55], [56]. Magnetostrictive transducer converts the magnetic energy into mechanical energy by utilizing the magnetostrictive material properties. The principle of this transduction method depends on the change of permeability of ferromagnetic materials when they are subjected to strain like Ni for example. This strain changes the magnetic field that can be converted into mechanical energy. The drawback of this method is the high nonlinear behavior [7]. Piezoelectric harvesters are considered by the studies the most efficient type of vibration transduction for MEMS applications [57], [58]. Prior researches have shown the significant advantages of piezoelectric harvesters. One of the most important benefits is the high-power density ability of piezoelectric harvesters compared to electrostatic and electromagnetic harvesters. Also, the high electromechanical coupling in piezoelectric harvesters has led to higher power output. Unlike the electrostatic harvesters, piezoelectric harvesters don't require an external voltage source. Furthermore, the ability to harvest energy using piezoelectric harvesters under a wide range of frequencies increased the usage and the popularity of this kind of transduction mechanism [7]–[9]. Table 3 shows a comparison between the four main vibration transductions reviewed by the literature [23],[52].

Table 3: Advantages and disadvantages of different energy harvesting transductions [23],[52]

Transduction type	Advantages	Disadvantages
Piezoelectric	<ul style="list-style-type: none"> <li>• High efficiency</li> <li>• Long lifetime</li> <li>• No need for external voltage source</li> <li>• Compact setup structure</li> <li>• High electromechanical coupling</li> <li>• Easy to integrate with MEMS applications</li> <li>• High efficiency system</li> </ul>	<ul style="list-style-type: none"> <li>• Brittleness of the material</li> <li>• Depolarization</li> </ul>
Electrostatic	<ul style="list-style-type: none"> <li>• No smart material needed</li> <li>• Voltage output 2~10</li> </ul>	<ul style="list-style-type: none"> <li>• Need of external voltage source</li> <li>• The small size lead to a high increase in the capacitance</li> <li>• Difficulty in adjusting the coupling effect</li> </ul>
Electromagnetic	<ul style="list-style-type: none"> <li>• No smart material needed</li> <li>• High output current</li> <li>• No external voltage sources</li> <li>• Long lifetime</li> </ul>	<ul style="list-style-type: none"> <li>• Very low voltage of maximum 0.1V</li> <li>• Incompatible with MEMS</li> </ul>
Magnetostrictive	<ul style="list-style-type: none"> <li>• High coupling coefficient</li> <li>• Compatible for high frequency ranges</li> </ul>	<ul style="list-style-type: none"> <li>• Complexity in material fabrication</li> <li>• Nonlinearity problems</li> </ul>

The discussed advantages of piezoelectric harvesters have caught the researcher's attention which resulted in an exponential growth in the number of piezoelectric energy harvesting publications in the last two decades, as shown in Figure 3 [62].

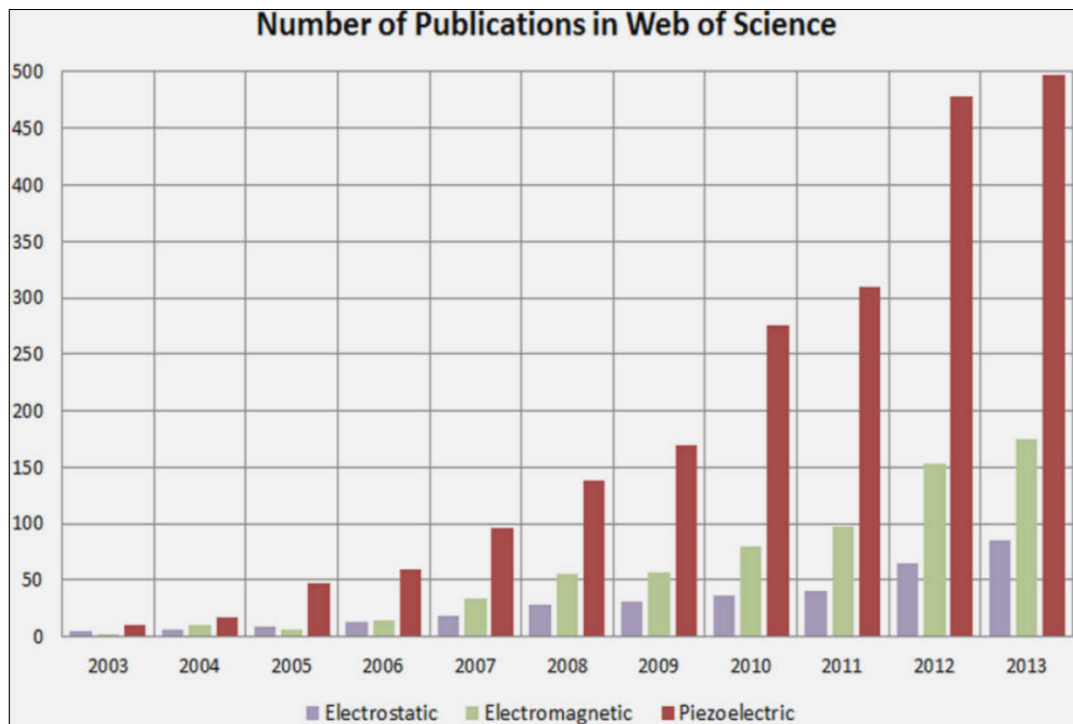


Figure 3: Number of publications of different vibration energy harvesting transductions between year 2003 and 2013. Reproduced with permission from [62], Elsevier, 2017.

One of the simplest and efficient setups of piezoelectric harvesters is the cantilever beams. It consists of two layers of piezoelectric material separated by a metal substrate. A tip mass is usually attached to the tip to control the frequency of the piezoelectric harvester. This piezoelectric cantilever setup is called bimorph piezoelectric cantilever. Surface electrodes are attached to the piezoelectric layers. The two layers are electrically connected in either series or parallel to convert the vibration energy to electrical energy through the piezoelectricity effect. The direct piezoelectricity effect is the ability of the material to convert the mechanical stress into an electrical output [8]–[10]. Figure 4 shows a typical bimorph piezoelectric cantilever harvester with tip mass. More about the piezoelectric fundamentals and configurations are discussed in detail in the following section.

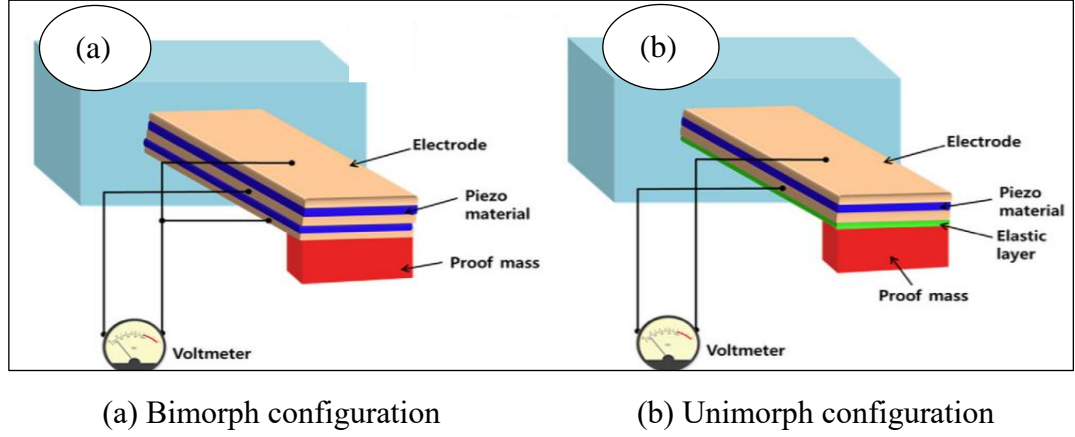


Figure 4: Different configurations of the piezoelectric cantilever harvester with tip mass. Reproduced with permission from [65], Physics Report, 2018.

### 2.3 Fundamentals of piezoelectric harvesters

The piezoelectric effect or piezoelectricity was first discovered by Curie brothers in 1880. The unique characteristics of piezoelectric materials lie in the electromechanical coupling effect where the material can generate electrical energy from applied stress and vice versa. There are two different effects of piezoelectric materials: the direct and the inverse effects. The direct piezoelectric effect happens when mechanical stress is applied to the piezoelectric material and generates electrical output. In contrast, the inverse piezoelectric effect applies when an applied electric field causes the material to strain [51], [66]. The following two equations are the fundamentals of piezoelectricity and it describes the direct and inverse piezoelectric effects as follows [67]:

$$D_i = d_{ij}\sigma_j + \varepsilon_{ii}^T E_i \text{ or } D_i = e_{ij}S_j + \varepsilon_{ii}^S E_i \quad (1)$$

$$S_j = s_{ij}^E \sigma_j + d_{ij} E_i \text{ or } T_j = c_{ij}^E S_j - e_{ij} E_i \quad (2)$$

Where  $D_i$  is the electrical displacement,  $S_j$  and  $\sigma_j$  are mechanical strain and stress respectively.  $E_i$  is the electric field.  $c_{ij}$  and  $s_{ij}$  the elastic stiffness coefficient and elastic compliance coefficient respectively.  $\epsilon_{ii}$  is the permittivity. The superscripts ‘s’, ‘E’ and ‘T’ represent the constant parameters used.  $d_{ij}$  and  $e_{ij}$  are piezoelectric coefficients.

From a material point of view, piezoelectric material is a crystal lattice structure. This structure consists of a balanced positive and negative polarization. when the stress is applied, the charge in the material is disturbed, this disturbance is a form of energy that will create a current in the crystal which can be harvested. This describes the direct piezoelectric effect. The indirect piezoelectric effect happens when the crystalline material is applied to an electrical charge that will cause an imbalance in the natural charge of the crystalline which will result in a strained material [51].

Piezoelectric materials are anisotropic materials where the property of piezoelectric materials depends on the direction of the applied forces as well as the polarization and electrodes orientation. Each piezoelectric material property consists of two subscripts ‘ $ij$ ’ as shown in equation (1). These subscripts specify the direction of the mechanical and electrical parameters. Figure 5 represents the direction of index of piezoelectric materials. 1, 2, 3 indicates the direction of properties along X, Y, Z axes and 4, 5, 6 is the shear constant [67], [68]. Based on this specific index notation, piezoelectric materials have different operational modes which are discussed in detail in the next subsection.

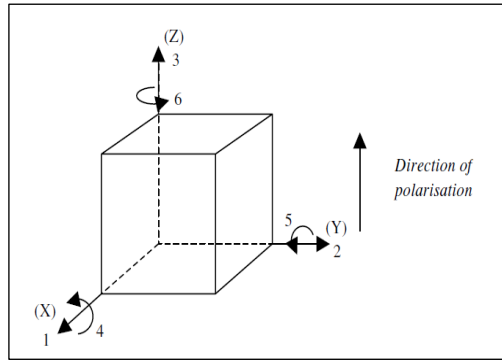


Figure 5: Direction of index of piezoelectric material element. Reproduced with permission from [45], IOP Publishing Ltd., 2006.

### 2.3.1 Modes of piezoelectric harvesters

Piezoelectric harvesters operate under three different modes:  $d_{31}$ ,  $d_{33}$  and  $d_{15}$  modes. Each mode depends on the direction of the applied force and the induced electrical field. Thus, each piezoelectric harvester application uses a suitable operational mode which assures the maximum efficiency of the system.  $d_{31}$  mode operates when the applied stresses along direction 1 cause an induced electrical output in direction 3 of the piezoelectric material. The piezoelectric material in  $d_{31}$  is sandwiched between the two electrodes. In  $d_{33}$  mode the electrical field is produced in the same direction of the applied stress along the piezoelectric material. Figure 6 shows  $d_{31}$  and  $d_{33}$  mode of the piezoelectric harvester.

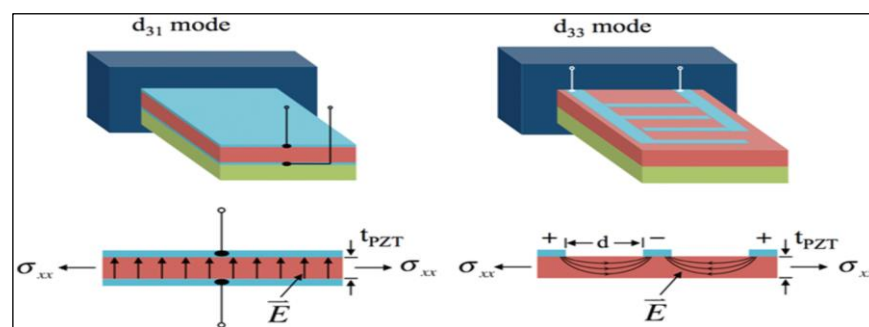


Figure 6: Representation of the polarization in  $d_{31}$  and  $d_{33}$  modes. Reproduced with permission from [67].



Studies have shown that the voltage output of the  $d_{33}$  mode of piezoelectric harvester is higher than  $d_{31}$  mode. This is because the voltage coefficient  $g_{33}$  is twice higher than  $g_{31}$  [51], [69]. Researchers recommended the use of an interdigitated electrode pattern (IDE) as a replacement of the top and bottom electrode (TBE) used in  $d_{31}$  harvesters as displayed in Figure 7 [70]. This electrode pattern will allow the harvester to operate under  $d_{33}$  mode by letting direction 3 coincides to match the orientation of the harvester length.

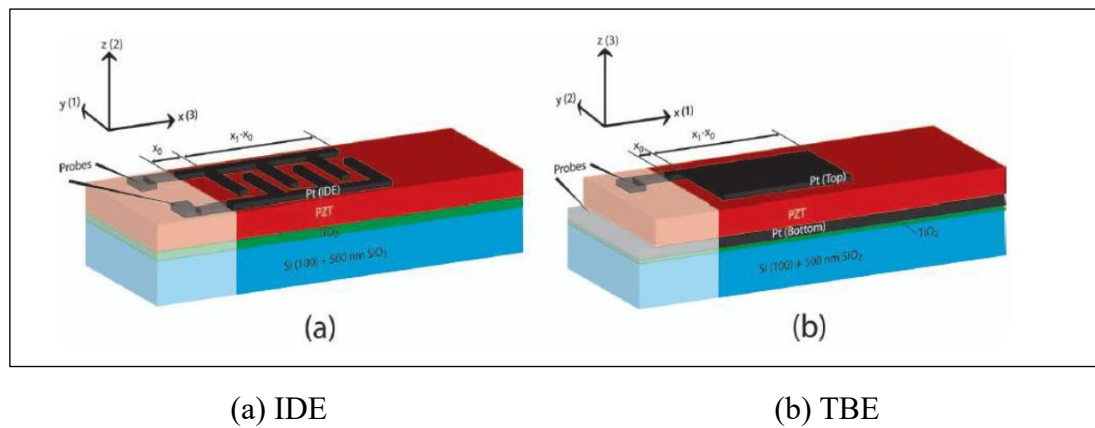


Figure 7: Two different electrode patterns for operating modes of piezoelectric harvesters. © 2012 IEEE.

Studies have been comparing between  $d_{31}$  and  $d_{33}$  modes in terms of power generation. Kim and his colleagues compared between piezoelectric harvesters operating under  $d_{31}$  mode and  $d_{33}$  modes [71]. Both piezoelectric cantilevers had the same dimensions and the resonance frequency of the excited systems was 243 Hz. Both analytical and experimental results showed that the piezoelectric cantilever of  $d_{31}$  mode generated  $2.15 \mu\text{W}$  while the  $d_{33}$  mode generated  $2.33 \mu\text{W}$ . A further analysis on the IDE dimensions of  $d_{33}$  mode was done. Results showed that the power output of the piezoelectric harvester operating under  $d_{33}$  mode depends on the width of the electrodes in IDE. However, the IDE doesn't allow a good polarization of the

PZT material which is indicated by the curved polarization arrows in Figure 6. This drawback will affect the power output as well as the efficiency of the piezoelectric harvesters of mode  $d_{33}$  [67]. One application has been developed for a piezoelectric harvester implemented in a car door latch system using  $d_{33}$  operating system [51]. The operating frequency of the door latch is between 0 and 10 Hz with a repetitive displacement of maximum 1 mm. A proposed design of  $d_{33}$  PZT electromechanical system can be coupled with the closure part of the door latch to produce energy as shown in Figure 8.

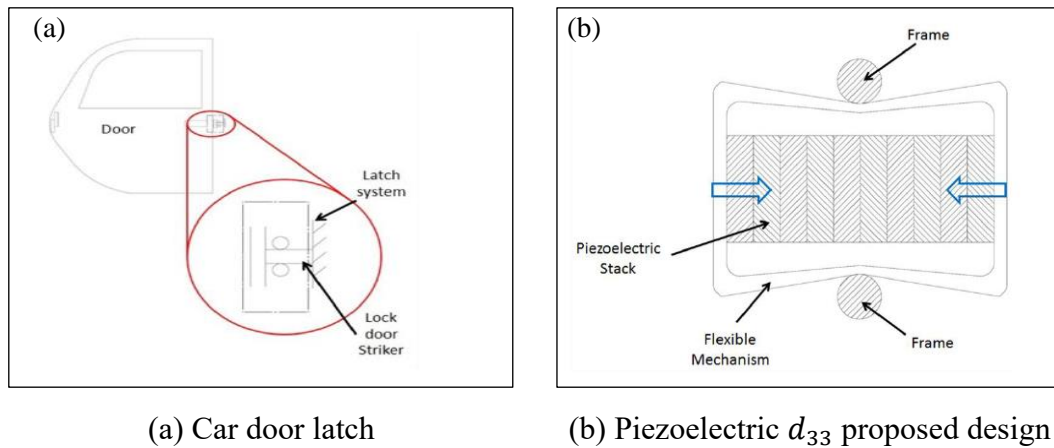


Figure 8: Piezoelectric harvester implemented in a car door latch [51]

$d_{15}$  mode in piezoelectric harvesters are associated with the shear stress denoted by  $\sigma_{31}$  where the electrical output will be normal to the polarization and the shear stress which are along direction 1 as shown in Figure 9 [51].

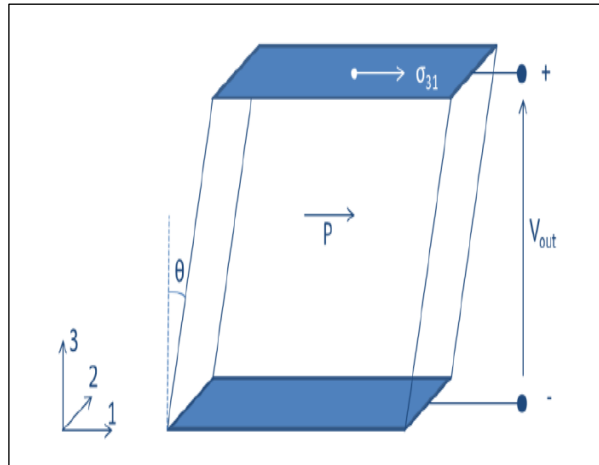


Figure 9: Schematic of a shear stress harvester of  $d_{15}$  mode [51]

Authors have driven further development in harvesting energy from shear stress harvesters. Zhao et al. developed a new setup of  $d_{15}$  mode piezoelectric harvester [72]. Two PZT-51 elements operating using  $d_{15}$  mode were connected in series as shown Figure 10. They have compared their setup with another  $d_{15}$  mode single PZT-51 element. Experimental and FE results showed that the peak to peak voltage of the developed setup reached 25.4 V whereas the traditional  $d_{15}$  mode harvester harvested 15.6 V. The findings of this work showed that the  $d_{15}$  mode with a series connection structure has a great potential in generating more power output than the traditional  $d_{15}$  structure.

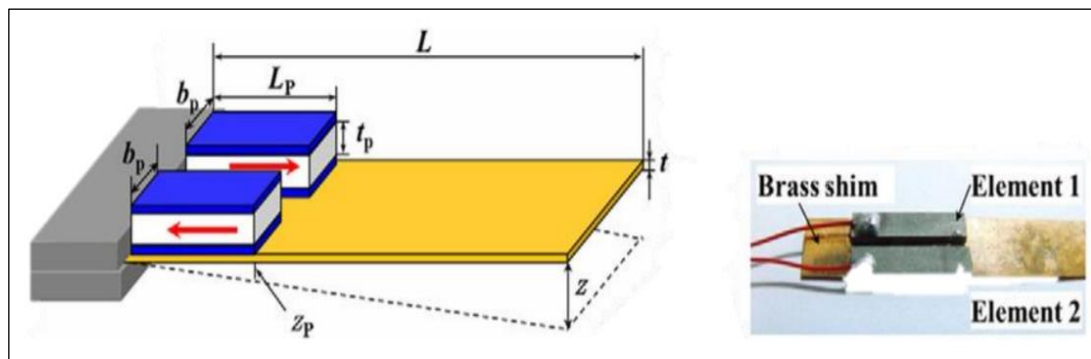


Figure 10: Representation of  $d_{15}$  series structure piezoelectric harvester. Reproduced with permission from [72], IOP Publishing, 2012.

Another  $d_{15}$  mode piezoelectric harvester was designed by Wang and Liu [73]. They used a shear mode PZT-5H element laid on a nickel diaphragm that vibrates using pressurized water flow. The power generated using their harvester was about 0.45 nW. Majidi et al. proposed a new design of ZnO nanoribbons piezoelectric harvester [74]. Their analysis showed that through the shear mode of the vertically arranged ZnO nanoribbons, an electrical output could be harvested due to the lateral deformation of these ribbons in Figure 11. They predicted that their design could generate up to 100 nW/mm<sup>3</sup>.

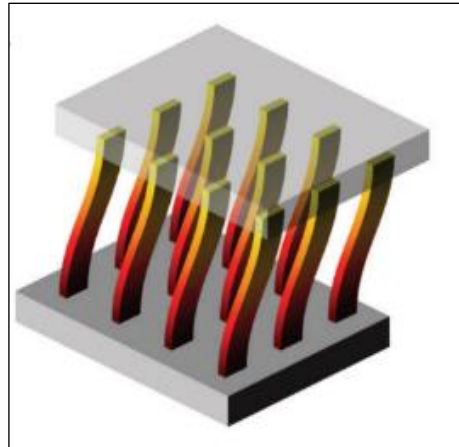


Figure 11: ZnO nanoribbons. Reproduced with permission from [74], IOP Publishing, 2010.

Generally, the three operational modes of piezoelectric harvesters have been used in different applications as discussed in the literature. Nevertheless,  $d_{31}$  is the most used mode because of its easy fabrication process as well as its ability to be implemented in various applications.  $d_{33}$  and  $d_{15}$  showed a great potential in harvesting higher voltage and power, however, the complicated fabrication process and electrode positioning constraints had limited their usage to a specific number of applications.

### 2.3.2 Piezoelectric material

Piezoelectric materials are a combination of materials that can convert the applied stress into an electrical output and vice versa. Researchers have produced an excellent reviews related to piezoelectric materials [20]–[22]. Piezoelectric materials are divided into four main types based on their structural properties: ceramics, single crystals, polymers and composites [7], [75]. Table 4 shows the advantages and disadvantages of each material type used in piezoelectric harvesters. Ceramics are the most known and used material in piezoelectric harvesters. They provide a high output voltage which can reach up to 100 V.

Table 4: Advantages and disadvantages of material types used in piezoelectric harvesters [7], [38]

Material type	Advantages	Disadvantages
Ceramics	<ul style="list-style-type: none"> <li>• Low cost</li> <li>• Good piezoelectric properties</li> <li>• Easy implementation in applications</li> <li>• high electromechanical coupling constant</li> <li>• High energy conversion rate</li> </ul>	<ul style="list-style-type: none"> <li>• Brittle material</li> <li>• High density</li> </ul>
Single Crystals	<ul style="list-style-type: none"> <li>• Excellent piezoelectric properties</li> <li>• High strain constants</li> </ul>	<ul style="list-style-type: none"> <li>• Complicated fabrication</li> <li>• High cost</li> <li>• Brittle material</li> </ul>
Polymers	<ul style="list-style-type: none"> <li>• Flexible</li> <li>• Easy to form</li> <li>• Easy implementation in micro devices</li> </ul>	<ul style="list-style-type: none"> <li>• Low coupling</li> </ul>
Composites	<ul style="list-style-type: none"> <li>• Flexibility</li> <li>• Ease of fabrication on curved structures</li> <li>• Ability to fabricate thin layers</li> </ul>	<ul style="list-style-type: none"> <li>• High cost</li> </ul>

The affordable cost of ceramics fabrication allowed the material to be used in many MEMS applications. The most popular type of piezoelectric ceramics is the PZT because of its excellent electromechanical properties and high Curie temperature.

Curie temperature is the critical temperature which beyond it the material will lose its piezoelectricity effect. The most known types of PZT ceramics are the PZT-5A and PZT-5H families. Depending on piezoelectric applications, piezoelectric ceramics can be configured in different shapes. Plates, thin and thick films are usually to harvest energy from low vibrational sources whereas piezoelectric stacked ceramics are used to harvest energy from high impact mechanical sources [7], [38]. Piezoelectric single crystals are the single crystalline isotopes of piezoelectric ceramics elements. The most used single crystals materials are lead magnesium niobate/lead titanate (PMN-PT) also known as ferroelectric single crystals and lead zirconate niobate/lead titanate (PZN-PT). These two types have shown an excellent piezoelectricity effect. Due to the super aligned negative and positive ions in PMN-PT, their strain constant is higher than ceramics. Also, the Young's Modulus of Elasticity is less than ceramics that it can be used for lower frequency applications with small scale piezoelectric harvesters. Beda et al. studied the performance of single crystals in comparison to ceramics. The study used PMN-25% PT single crystal with ceramics and compared the power output of each material used while keeping the two cantilever harvesters at the same volume. The power output of PMN-25% PT piezoelectric cantilever beam was 4 mW while the ceramic piezoelectric cantilever gave 0.2 mW of power output [76]. Mo et al. investigated the performance of PMN-33% PT single crystal and PZT-5H ceramics of a circular diaphragm harvester. Using a frequency of 1 Hz and the same volume for both harvesters, the power output was compared. Results showed that single crystal material of PMN-33% PT harvester gave around 4 mW, whereas the PZT-5H harvester gave 0.3 mW [77]. Some recent studies showed that single crystals piezoelectric materials can revolutionize the performance of piezoelectric harvesters [78],[79]. Yet, the complexity of the fabrication process, high costs and brittleness can certainly limit

the number of applications that can be used by single-crystal piezoelectric harvesters. Polymers are another type of piezoelectric materials. Polymers are repetitive chains of carbon-based molecules. The most popular type of polymers used in piezoelectric harvesters is polyvinylidene difluoride (PVDF). This type of piezo materials is known of its flexibility and high deformation. Thus, it is mostly used in wearable piezoelectric harvester applications [7], [38]. As shown in Table 5, the density of piezoelectric polymers is less than ceramics, hence the lightweight. In terms of the frequencies and power output polymers compared to ceramics, Table 6 shows a simple performance comparison of the two materials. One of the main drawbacks of PVDF polymers is the low coupling effect. Thus, researchers worked on the idea of increasing the electromechanical coupling effects of PVDF polymers. In 2015, Pan et al. proposed an idea of increasing the coupling of PVDF using the near-field electrospinning method [80]. Their findings showed that the coupling of PVDF material was doubled. A recent study was done by Harsted and his colleagues to improve the coupling of PVDF material [81]. They increased the  $\beta$ -phase percentage in the material which is directly proportional to the electrotechnical coupling coefficient. Ceramics and polymers can be combined to form an excellent piezoelectric properties and flexible structural material that is called piezoelectric ceramic-polymer composites. The structure of the material will consist of particles, fibers and rods of ceramics and the rest of the material space will be filled by polymers [7]. PZT fibers are the most used type in composites. Researchers have heavily explored the use of composites in different piezoelectric harvesting applications. Hu et al. replaced the digital watch battery with a zinc-oxide (ZnO) nanocomposite generator [82]. Churchill and his colleagues used a fiber-based film composite to design a piezoelectric harvester that

can power wireless sensors [83]. Their experimental results showed that the film could produce up to 0.75 mW which can operate a radio wireless transmitter.

Table 5: Properties of piezoelectric materials [7]

Property	PZT-5H	PMN-32PT	PZT rod-polymer composite	PVDF (polymer)
Density (g/cm <sup>3</sup> )	7.65	8.10	3.08	1.78
Dielectric constant $\epsilon_r$	3250	7000	380	6
Young's Modulus of Elasticity $Y_{33}$ (Gpa)	71.4	20.3	-	2
Mechanical quality factor $Q_m$	32	-	-	10
Piezoelectric charge constant $d_{33}$ (pC/ N)	590	1620	375	25
Piezoelectric charge constant $d_{31}$ (pC/ N)	-270	-760	-	12-23
Electromechanical coupling factor $k_{33}$	0.75	0.93	-	0.22

Table 6: Comparison between application usage of piezoelectric ceramics and polymers

Piezoelectric material	Preferable frequency range application	Power output magnitude
Ceramics	> 50 Hz	Milliwatts
Polymers	< 10 Hz	Microwatts and nanowatts

### 2.3.3 Piezoelectric configurations

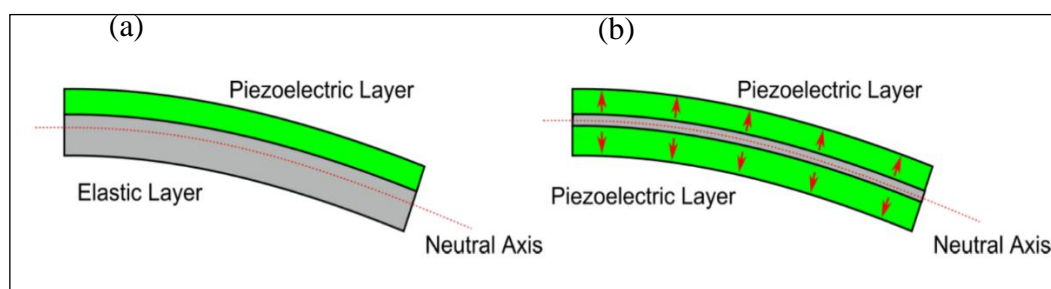
Researchers have always been interested in the structural design of piezoelectric harvesters to maximize the ability to harvest energy depending on different applications. Piezoelectric harvester configurations can be in the setup of:



cantilever [84]–[88], cymbal [89]–[94], stack [66], [95]–[97], diaphragm [98]–[102] and shear mode configuration [73], [103]–[105].

- Piezoelectric cantilever harvesters

Piezoelectric cantilever beam harvesters are the most used configurations because they can work with medium to high frequency ranges and they are suitable for applications with low input excitations. Their setup consists of a metal layer covered by a piezoelectric layer clamped at the root and free at the end. The root is attached to the input excitation. A tip mass is usually attached at the free end of the cantilever beam to control the frequency of the system. There are two structures of piezoelectric cantilever beams: unimorph and bimorph beams as shown in Figure 12. The unimorph structure is one layer of the piezoelectric material lies on the substrate layer. Bimorph cantilever is when the metal substrate is sandwiched between two piezoelectric material layers which double the voltage output in comparison to the unimorph type [20].



(a) Unimorph cantilever

(b) Bimorph cantilever

Figure 12: Unimorph and bimorph piezoelectric cantilevers. Reproduced with permission from [20], Royal Society of Chemistry, 2013.

- Piezoelectric cymbal harvesters

Cymbal harvester structure consists of a piezoelectric disc covered with two metal end-caps from both sides made of steel usually because of its high yield strength [7]. Cymbal configurations are usually used for low frequency applications (below 10 Hz) and they can handle high loads. Figure 13 shows the design of a piezoelectric cymbal harvester [94]. The working principle of this harvesters is amplifying and converting the applied axial stress to radial stress in the piezoelectric disc. Hence,  $d_{31}$  and  $d_{33}$  modes are coupled together to form the cymbal piezoelectric constant as [106]:

$$d_{cymbal} = d_{33} + G|d_{31}| \quad (3)$$

Where  $G$  is an amplification factor.

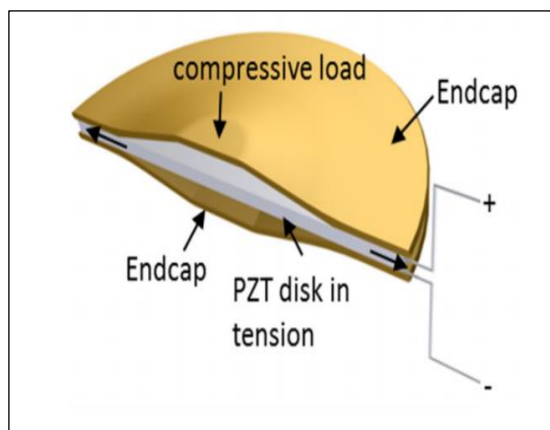


Figure 13: Cymbal piezoelectric harvester. Reproduced with permission from [94], IOP Publishing, 2017.

Kim et al. developed a piezoelectric harvester using a ceramic disk of 29 mm diameter and a thickness of 1 mm. The harvester was tested under an applied force of 7.8 N and 70 N. At a resonance frequency of 100 Hz; the piezoelectric cymbal shaped harvester produced a power output of 39 mW and 52 mW [106].

- Piezoelectric stack harvesters

When piezoelectric elements are stacked together in layers and operate under  $d_{33}$  mode it is called piezoelectric stack harvesters. Figure 14 shows a schematic of piezoelectric stack. Piezoelectric stacks are shown to give a higher power density than the cantilever types, yet they need a very high compressive force because of their high stiffness [66]. An experimental study was developed by Xu et al. using piezoelectric stack harvester that consists of 300 layers of PZT material. The output indicated that the power density produced by the stack configuration is higher than the cantilever shape for the weight and size of the harvester [107].

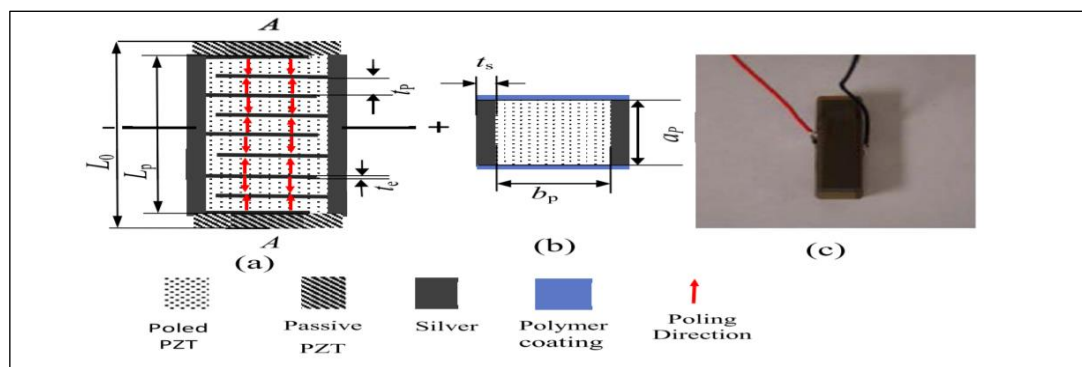


Figure 14: Piezoelectric stack (a) Schematic of piezoelectric stack (b) Cross section of PZT stack (c) A piezoelectric stack used in experimental setup. Reproduced with permission from [107], IOP Publishing, 2013.

- Piezoelectric diaphragm harvesters

The structure of piezoelectric diaphragm consists of a ceramic disc attached to a metal shim. Diaphragm harvesters work under  $d_{31}$  operating system like cantilever harvesters. They are best to work for high acceleration and unsteady pressure conditions [98]–[102].

- Piezoelectric shear-mode harvesters

Shear mode configuration has shown to give a higher voltage output than the rest of the configurations because of its electromechanical coupling which is different than the other discussed configurations [73], [103]–[105].

## **2.4 Modeling of piezoelectric cantilever beam**

It is of crucial importance to scrutinize the vibration response of the piezoelectric cantilever harvesters to understand the power capability of the piezoelectric harvesters. As a result, researchers have been developing different modeling techniques and methods to understand the dynamics of piezoelectric cantilever harvesters. Examples of these models are the mass spring damper model, equivalent circuit model, finite element model (FEM) and thermal analogy methods [54], [108]. However, most of the work done in this area was based on two main models; the lumped parameter model (LPM) which is mainly a single degree of freedom model (SDOF), and the distributed parameter model (DPM). The distributed parameter model is based on the lateral forced vibration of the piezoelectric cantilever beam which is rather a comprehensive and accurate estimation of the vibration response of the piezoelectric harvesters [109]. However, researchers prefer the LPM for its simplicity. The LPM treats the cantilever beam as a spring-mass-damper system located at the beam tip. The piezoelectric resistive force is placed parallel with the spring and damper forces. The piezoelectric forces and induced current are related through the piezoelectric constitutive equations and a suitable coupled electromechanical expression can be derived for the LPM [14]. The LPM parameters are estimated using Rayleigh-Ritz and Euler-Bernoulli beam theory [9], [110]. This model gives an initial perspective of the vibration response using simple mathematical

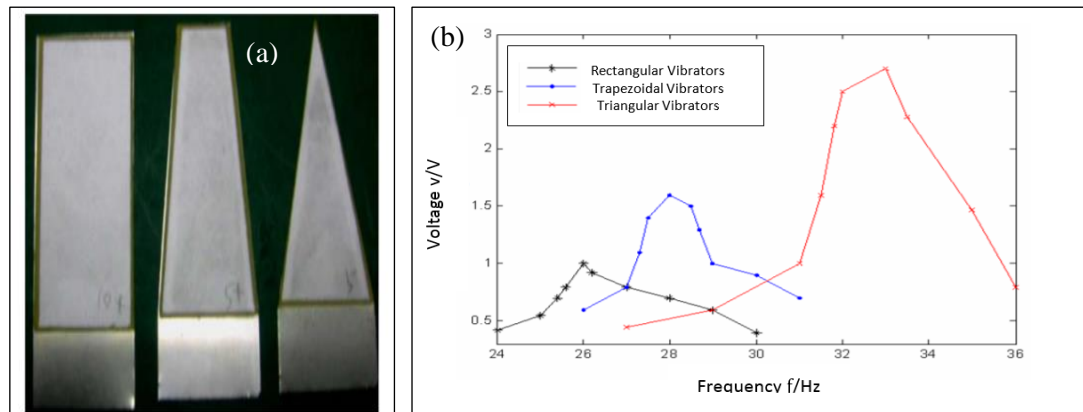
closed form. However, it was noticed that the simplifications in modeling the piezoelectric harvesters using the LPM have led to critical errors in estimating the vibration response of the harvesters [9], [110]. These critical errors are due to the limitation of using the first mode shape strictly and the improper strain distribution along the cantilever beam. These issues resulted in an underestimation of the vibration response of the harvester, which in consequence affected the electrical output and gave an inaccurate power generation prediction of the piezoelectric cantilever harvesters. It is worth mentioning that the results were significantly deviated in the systems with very low or no tip mass [17]–[19]. Later, Erturk and Inman presented the response of the Euler Bernoulli beam to vibrational base. They improved the damping term in the model by separating the viscous damping from the structural damping which resulted in a more accurate representation of the model. They used the transmissibility function to investigate the error of the LPM as compared to the DPM. The relative displacement transmissibility function is the ratio of tip displacement to the base displacement. The comparison showed an error in predicting the tip motion of more than 35% using the LPM irrespective of the damping ratio. As a result, they developed a correction factor for both transverse and longitudinal piezoelectric cantilever harvesters. The effect of tip mass to beam mass ratio on the vibration response was also investigated. The correction factor of a transverse piezoelectric cantilever beam is estimated to be around 1.566 for no tip mass attached on the piezo beam. Also, results showed that as the tip to beam mass ratio increases the correction factor approaches unity and thus, uncorrected lumped model can be considered for high tip to beam mass ratio cases [109]. An experimental validation of the correction factor was done to confirm the accuracy of the correction factor calculations. Wang et al. introduced an improved lumped parameter model where he took in consideration the effect of the dynamic

mode and the distribution of the strain in transverse piezoelectric cantilever harvesters. Results were verified experimentally and showed that the improved lumped model gives an exact first natural frequency like the coupled distributed model [111].

## **2.5 Design optimization of piezoelectric cantilever beam**

Scientists have been developing different designs and geometries to increase the power production of piezo harvesters. They found that geometry has a great effect on the harvesting ability of the piezoelectric cantilever beam.

In 2005, Mateu et al. developed an analytical comparison between rectangular and triangular piezoelectric cantilever beams. A uniform stress along the width of the cantilever beams was assumed. The study showed that the triangular piezoelectric cantilever beam gives a higher average strain and larger deflection in comparison to the referenced rectangular piezoelectric cantilever. This led to an increase in the power density of the new proposed shape [112]. Simon et al. studied the effect of tapering the width of piezoelectric cantilever at the free end with  $0.3^\circ$  slope angle. The results showed that the power production increased 69% more than the rectangular shape in [113]. Chen et al. examined the effect of different geometries on the power production of piezoelectric harvesters by forming a strain distribution model for rectangular, trapezoidal and triangular shapes [114]. Results from the finite element model and experiment showed that the strain distribution affects the voltage output. The study proved that a triangular shaped piezoelectric cantilever gives the best strain distribution and thus the highest voltage output compared to trapezoidal and rectangular shapes as shown in Figure 15.

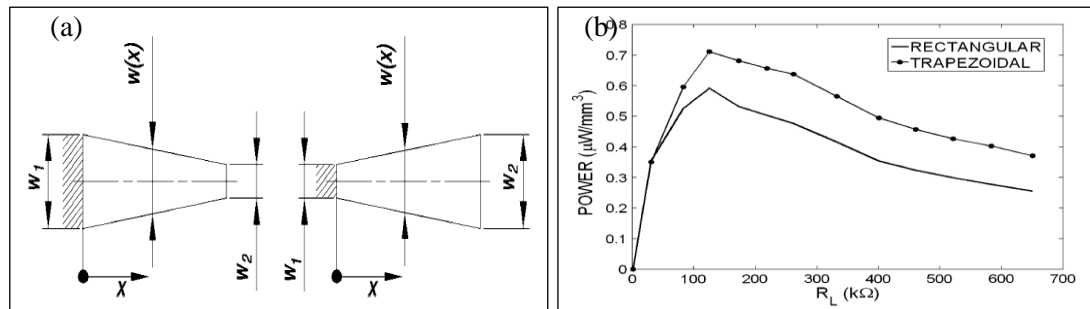


(a) Rectangular, trapezoidal and triangular piezoelectric harvesters

(b) Voltage outputs of the three piezoelectric cantilevers' shapes

Figure 15: Different shapes of piezoelectric harvesters [114]. © 2009 IEEE.

Similarly, Benasciutti et al. investigated the stress and strain distribution of trapezoidal and inverse trapezoidal piezoelectric bimorph harvesters with a tip mass [115]. Their main aim was to design an optimized shape that maximizes the power output per unit volume in piezoelectric harvesters. Finite element modeling was used to evaluate the analytical formulation. Results showed that the trapezoidal shape gives more uniform stress and strain distribution than the regular rectangular shape. However, the reversed trapezoidal shape has a larger localized maximum stress magnitude than the trapezoidal shape. This high stress could easily surpass the ultimate strength of the piezo material and hence may cause fatigue. As a result, only the trapezoidal shape was considered and compared with the rectangular shape experimentally. The preliminary results confirmed that the trapezoidal shape gives a higher power per unit volume magnitude than the rectangular shape harvesters as shown in Figure 16.



(a) Schematic of trapezoidal and reversed trapezoidal piezoelectric cantilever (b) Power density for rectangular and trapezoidal piezoelectric harvester

Figure 16: Configurations and results of piezoelectric cantilever harvesters. Reproduced with permission from [115], Springer Nature, 2009.

Dietl et al. developed an analytical solution for tapered width piezoelectric beam with tip mass [116]. He tracked the same method done by Sodano et al. in [12] by using the Hamiltonian principle to model a coupled electromechanical system. Dietl re-derived the system of Sodano but for varying width piezoelectric beam. This study didn't consider the damping effect in the model. However, the developed model was validated experimentally. Their proposed optimized beam gave 0.52% higher power than the normal rectangular beam. The results also showed that the power begins to increase when the taper ratio increases. Samah Ben Ayed et al. examined the effect of variable shapes on the power production [117]. They derived an electromechanical model of linear and quadratic shape width variation of a unimorph piezoelectric beam with tip mass at the free end. Figure 17 shows the linear and quadratic schematic of piezoelectric harvester. The analytical solution was done based on differential quadrature method for the quadratic shape and Galerkin discretization for the linear rectangular shape. Results showed that the quadratic shape gave a normalized power output twice higher than the linear shape for specific load resistance.



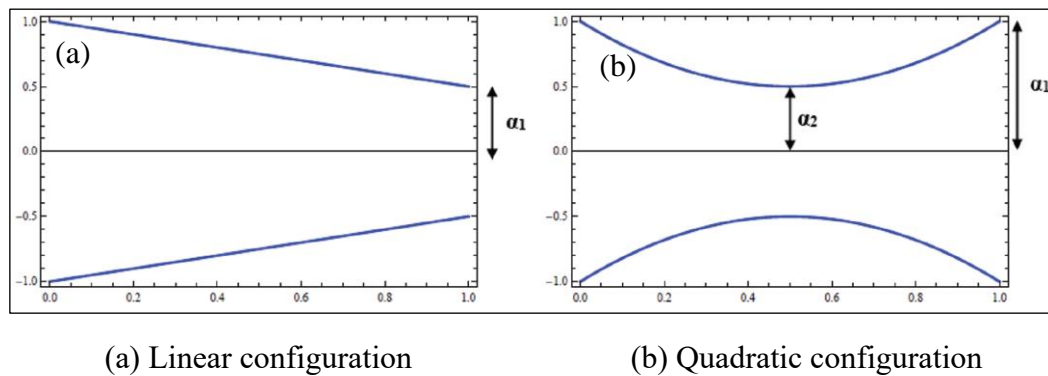


Figure 17: Linear and quadratic piezoelectric cantilever harvesters. Reproduced with permission from [117], SAGE Publications, 2014.

Rosa and De Marqui later improved the varying-width piezoelectric beam model by adding damping [118]. The model was first validated with the analytical solution of Inman in [19] for rectangular shape. Experimental verification was then carried for tapered bimorph piezoelectric beam with tip mass and showed a good agreement with the developed analytical model. Later, Sushanta Kundu et al. studied the effect of tapering the thickness of bimorph piezoelectric cantilever with tip mass on the stress distribution that affects the power output [119]. Comparison between constant and tapered thickness piezoelectric cantilevers was done using COMOSOL Multiphysics Software. The tapered piezoelectric beam was done by reducing 50% thickness at the free end and increasing 50% of the thickness at the fixed end to keep the total volume constant as the constant thickness piezoelectric cantilever. Results indicated that the tapered thickness showed more uniform stress along the piezoelectric cantilever beam. Power output of the piezoelectric cantilever harvester under 1 g excitation acceleration was 21.95 mW for constant thickness and 28.83 mW for tapered thickness. Muthalif et al. derived an analytical model for unimorph piezoelectric harvester based on the Euler Bernoulli beam theory and energy method [120]. The main goal of the developed model was to estimate the voltage output of the

harvester. A simulation was done using Matlab and COMSOL software to understand the influence of geometry on the voltage response. From the strain distribution simulation analysis, it was shown that the triangular shape has a double strain magnitude compared to the rectangular shape. Experimental validation was done for the completeness of the study and verified that the triangular shape harvesters produce more power output compared to the referenced rectangular shape. Chung Ket et al. developed a new approach of piezoelectric cantilever optimization method to find the best design in piezoelectric harvesters [121]. Their objective was to find the optimum design that gives the maximum power output and the minimum structural volume of the piezoelectric cantilever harvester. A FE comparison was done between the rectangular shape and the proposed optimum design. Results showed that the optimum shape have a better stress distribution than the rectangular shape as displayed in Figure 18. Theoretical, FEM and experimental studies was carried in their research. Results showed that the novel design developed by their optimization technique gave a power of  $4.62 \mu\text{W}/\text{mm}^2$  for a structural volume of  $60.97 \text{ mm}^3$  compared to a power of  $4.49 \mu\text{W}/\text{mm}^2$  for a structural volume of  $61.3 \text{ mm}^3$  in the triangular shape piezoelectric beam.

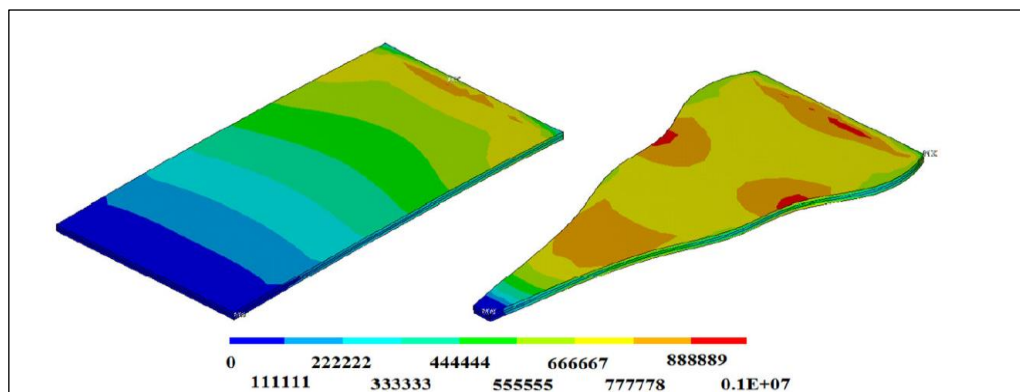


Figure 18: Stress distribution for rectangular and optimized shapes of piezoelectric harvesters done by [121]

Sarafraz et al. conducted a finite element analysis to understand the geometrical effect on the power production of the bimorph piezoelectric cantilever harvesters [122]. Seven main shapes were investigated: rectangular, trapezoidal, reversed trapezoidal, triangular, comb-shaped and both convex and concave parabola. Their work also included a parametric study of beam length, thickness and width and their effects on frequency, electric voltage and power. The simulation showed that the frequency was the lowest in the reversed trapezoidal shape. The paper stated that since the frequency is inversely proportional to the power, then the reversed trapezoidal has the maximum power output however, the published work lacks analytical or experimental validation. In 2018, Raju et al. derived an analytical solution for a piezoelectric unimorph cantilever beam based on the DPM [123]. Their work focused on increasing the power production of piezoelectric harvesters using innovative beam geometries. Various geometry alterations such as tapered width, tapered thickness and double taper (both in width and thickness) geometries were performed as shown in the schematic of Figure 19. Outcomes showed that when a piezoelectric patch is placed on a double tapered shaped cantilever beam, it gives 126% higher voltage compared to the normal rectangular beam. Also, an innovative idea of creating rectangular and trapezoidal cavities in the beams was proposed. Both analytical and experimental results validated that a piezoelectric patch placed on a double tapered beam with a trapezoidal cavity gives the highest power output.

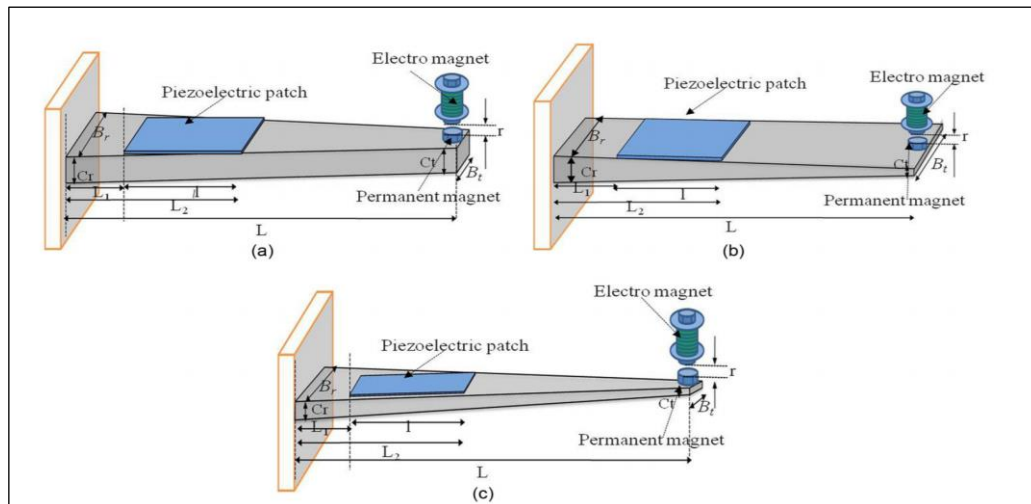


Figure 19: Piezoelectric energy harvesters for (a) width tapered beam (b) thickness tapered beam (c) both width and thickness tapered beam. Reproduced with permission from [123], SAGE Publications, 2018.

N. Aboulfotouh et al. developed an analytical solution based on LPM to estimate the power production of bimorph piezoelectric beam with a tip mass [124]. The estimated power depends on the geometrical shape of the piezoelectric beam. Moreover, an optimal load resistance of resonant frequency formulation was derived to give the maximum power gain. Effects of thickness ratio, length and mass ratio are evaluated using a parametric study. The resonance frequency of the harvester was kept constant throughout the study. Experimental verification was conducted to check on the correctness of the proposed mathematical solution. One of the highlighted results from this work is that increasing the tip to beam mass ratio will increase the power output considerably more than increasing the free length of the beam. Also, increasing the thickness ratio (defined as substrate thickness to piezoelectric thickness) will increase the electromechanical coupling significantly, thus it would increase the overall power production of the piezo harvester. Hosseini et al. worked on the development of an analytical model based on the distributed parameter model for bimorph tapered width piezoelectric harvester [125]. The study intended to find the

power production improvement of trapezoidal and triangular geometries compared to the rectangular piezoelectric shape. Rayleigh method is used in the derivation process to estimate the natural frequency of the tapered harvester. A closed form expression of the voltage output of tapered piezoelectric beam was obtained. In order to validate the analytical results, finite element modeling in ABAQUS software was developed. The strain analysis formed by the finite element model showed that the strain distribution of the triangular beam is uniform throughout the beam length as it is clarified in Figure 20. This result lead into a growth in the voltage, power output and efficiency of the harvester.

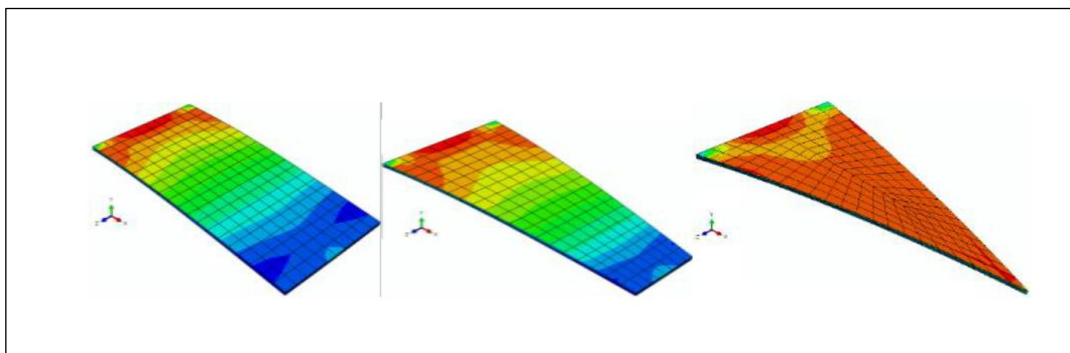


Figure 20: Strain distribution of rectangular, trapezoidal and triangular piezoelectric cantilever beams [125]

Salmani et al. derived an exact solution for an exponentially unimorph and bimorph tapered piezoelectric harvester with a tip mass [126]. They used the finite element approach to verify the derived analytical solution but for no tip mass case. The error between the finite element and the analytical solution was about 3.6%. An experimental validation was conducted and showed a good agreement with the analytical solution and an excellent match with a solution taken from [18], [19]. Parametric study was done in the same work to understand the tapering effect on the voltage response. The study concluded that the more tapered the beam, the higher

voltage output. Another comparison between the linearly tapered harvester from [118] and exponentially tapered harvester was done. The results showed that the voltage output of the exponentially tapered is less than the rectangular geometry. Later Salmani and Fakharian proposed an improved LPM for exponentially tapered piezoelectric beam with tip mass. Comparing the lumped parameter model and distributed parameter model using transmissibility ratio lead them to introduce a correction factor to reduce the error produced by the lumped model. The correction factor of tapering parameter of  $c= 11.55$  is estimated to be 1.677 for the first mode shape with no tip mass. Effect of tip mass was then added to the study and showed that as you increase the mass ratio the correction factor goes to unity. The validation was done by pushing the tapering ratio to be zero which gave a rectangular shape. The results showed the same correction factor derived by Erturk and Inman in [109]. Different correction factors was then estimated for different exponential tapered ratios and mass ratios [127].

## 2.6 Electric circuit of piezoelectric energy harvesting system

Electrical circuit is a fundamental part of any energy harvesting system. Three main components can generally identify any energy harvesting circuit: AC-DC rectifier, voltage regulator and an energy storing device as it is shown in Figure 21 clarifies [7].

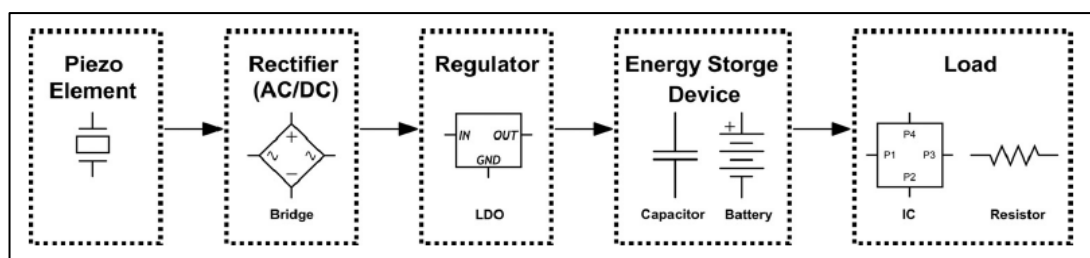


Figure 21: Electric circuit diagram of piezoelectric energy harvester [7]

In the piezoelectric harvesting system, AC voltage output from piezo material should be rectified to DC to supply energy for different devices. A voltage regulator is then needed to regulate the DC power [128], [129]. The energy-storing device is used to store the harvested energy for the desired applications.

Researchers have paid great efforts in developing piezoelectric harvesters' interface circuit to extract the maximum power output. There are four main conditioning circuits used in piezoelectric energy harvesters: diode bridge rectifier circuit, SECE circuit, parallel SSHI circuit and series SSHI circuit (Figure 22).

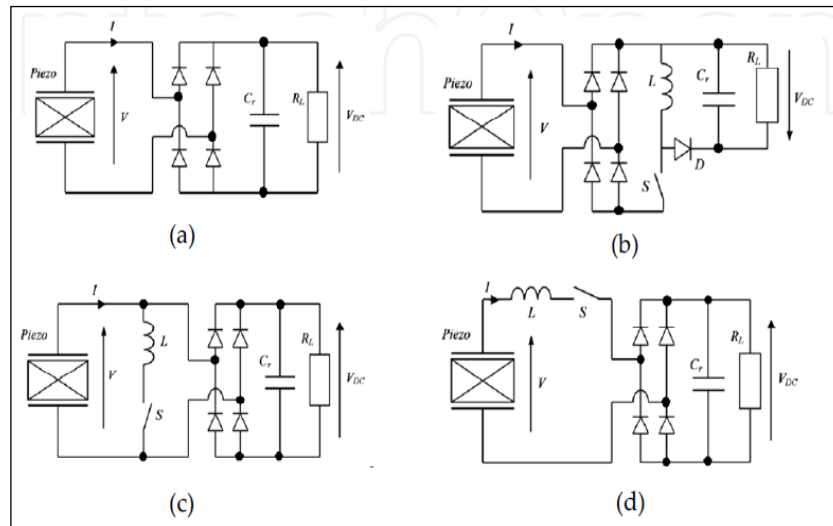


Figure 22: Conditioning circuits of the piezoelectric cantilever harvester (a) standard (rectifier) (b) SECE (c) parallel SSHI (d) series SSHI [130]

Diode bridge rectifier is the simplest and most used circuit in piezoelectric harvesting systems [51]. The disadvantage of this type that it lacks of voltage regulator which makes it inadequate for storing the harvested energy [38]. In 2005, Lefeuvre et al. proposed the synchronous electric charge extraction circuit (SECE) [131]. It works by transferring the electrical energy of the capacitor to the inductor when the switch is closed and vice versa when the switch is opened. Results indicated that the SECE

circuit has increased the energy conversion 4 times more than the direct rectifier circuit. Researchers then added an inductor to the SECE circuit and named it the synchronous switch harvesting on inductor circuit (SSHI). The inductor is placed between the piezoelectric harvester and the rectifier.

Parallel SSHI (synchronized switch harvesting on inductor) circuit is an inductor switch connected in parallel with the piezoelectric material element. A bridge rectifier is placed after the parallel SSHI. Researchers found that using this type of circuit increases the electromechanical coupling which by result maximizes the power output [132]–[135]. Series-SSHI is another type of circuit where the inductor switch is placed before the rectifier and connected with the piezoelectric material element in series.

E. Lefeuvre and colleagues examined the four different types of circuits experimentally to estimate their power production [136]. Results showed that the four circuits gave the same power output at different electromechanical coefficients. SECE circuit type gave the same power at the lowest electromechanical coupling. This indicates that the SECE circuit can reduce the piezoelectric material usage in the harvester since it is directly proportional to the electromechanical coupling. Lefeuvre et al. conducted an analytical and experimental research on Parallel-SSHI. Results indicated that the efficiency of this type of circuit has improved by 400% more than the standard rectifier bridge circuit [137]. Yu-Yin Chen et al. compared between three condition circuits which are: diode bridge rectifier, series- SSHI and SECE [138]. The comparison was done using circuit simulation on MATLAB. Results showed that series- SSHI type maximized the power four times more than SECE type and twice more than the bridge rectifier. Their experimental work showed a good agreement with



the simulation results. Lallert et al. proposed DSSH (double synchronous switch harvesting) interface circuit through analytical and experimental study [139]. Findings confirmed that the power extracted using DSSH circuit type is 500% more than the original rectifier circuit. Alwyn Elliott et al. studied the power production of piezoelectric harvesters that use SSPB (single supply pre-biasing) circuit [140]. The proposed circuit showed that it can harvest power up to six times more than the standard rectifier diode circuit. Recently, Giusa et al. proposed a novel circuit named RMSHI (random mechanical switching harvesting on inductor) which can extract voltage from weak arbitrary vibrations [141]. The circuit consists of a rectifier diode, inductor and capacitor and a mechanical switch. The mechanical switch consists of two stoppers placed below and above the piezoelectric cantilever harvester. When the displacement of the piezoelectric cantilever reaches the maximum, the switch is closed. Analytical, numerical and experimental studies were carried in this work and showed that this type of circuit can extract very low voltage unlike the usual diode rectifier circuit.

## **2.7 Application of piezoelectric energy harvesters**

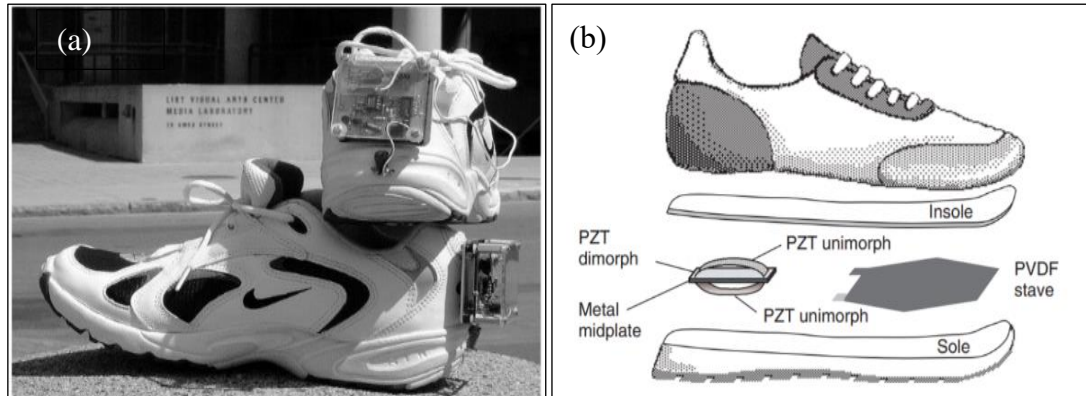
Recently, MEMS usage have been increased intensively in monitoring sectors, medical fields and even human lifestyle development. The great focus on this technology came from the ability to power these devices with a sufficient power density produced by ambient waste energy. Piezoelectric harvesters have been used in many applications. The applications can be categorized based on the source of vibration. The vibration sources are generally divided into three main sources: human body, manmade infrastructures and automobiles and the natural vibration from environmental sources

## **2.7.1 Energy harvested from human body**

The energy harvested from the human body can be used to power two types of devices: wearable devices and implementable devices. The wearable devices work based on the physical human activities whereas the implementable devices work based on the internal biological activities.

### **2.7.1.1 Wearable devices**

Further development in the efficiency of the biomedical devices was done in order to reduce their power consumption. With this growth, it has become achievable to harvest energy from major human activities like walking, running and typing, up to the small actions like breathing and muscle movements in order to derive these systems [68], [142]. A harvester that can convert the human actions into electrical output is called the wearable energy harvesting systems. These systems include a rectifying circuit to regulate the power output as well as a capacitor to store the power harvested [143]. Sheck and Paradiso have developed an innovative shoe piezoelectric harvester with a rectifier circuit as shown in Figure 23 [144]. PZT material was implemented in two main places in the shoes. First, PVDF stave was placed under the ball foot part. Second, piezoelectric bimorph was placed right under the foot heel. The energy harvested from the movement of the body through the mounted piezoelectric shoes was then used to activate a radio frequency identification tag (RFID).



(a) Mounted piezoelectric shoes for RFID applications usage (b) Installation of piezoelectric bimorph and PVDF stave in the shoes

Figure 23: Imbedded piezoelectric harvester in shoes. © 2001 IEEE.

Another piezoelectric shoes application was developed by Koichi Ishida et al. where they implemented a piezoelectric harvester with 2 V organic circuit in an insole pedometer [145]. As shown in Figure 24 one of the PVDF is for pulse detection and the other is to generate energy and power the pedometer. The organic circuit usage is to count number of steps detected.

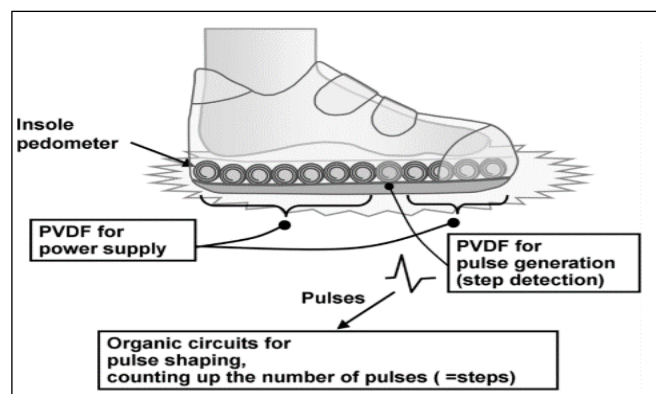


Figure 24: Insole piezoelectric harvester. © 2013 IEEE.

Furthermore, Yingzhou Han et al. showed an innovative design for piezoelectric harvesters embedded in a shoe insole. The stresses caused by the footstep on the insole will compress the piezoelectric harvester which will induce an electrical

output. Theoretical and experimental validation was done in this study and it showed that the insole can power up to  $100 \mu\text{W}$  which can feasibly power a smart band [146]. Zhao et al. designed another shoe embedded piezoelectric harvester that can generate up to  $1 \text{ mW}$  power at a frequency of  $1 \text{ Hz}$  of human walking [147]. Xie et al. proposed another harvester that can harvest energy from human walking activity at a low frequency [148]. The harvester device consists of bimorph piezoelectric configuration working at mode-31 with an amplification mechanism. A  $50 \times 40 \times 23 \text{ mm}^3$  device is embedded in a shoe insole. As the foot strikes the device in the shoe, the piezoelectric material is strained and an electrical output is produced. Figure 25 shows the experimental setup of the proposed harvester. Results from the experiment showed that a power output of  $18.6 \text{ mW}$  was produced from  $1 \text{ Hz}$  which represents the slow walking whereas  $27.5 \text{ mW}$  was produced from  $1.5 \text{ Hz}$  which indicates a fast walking.

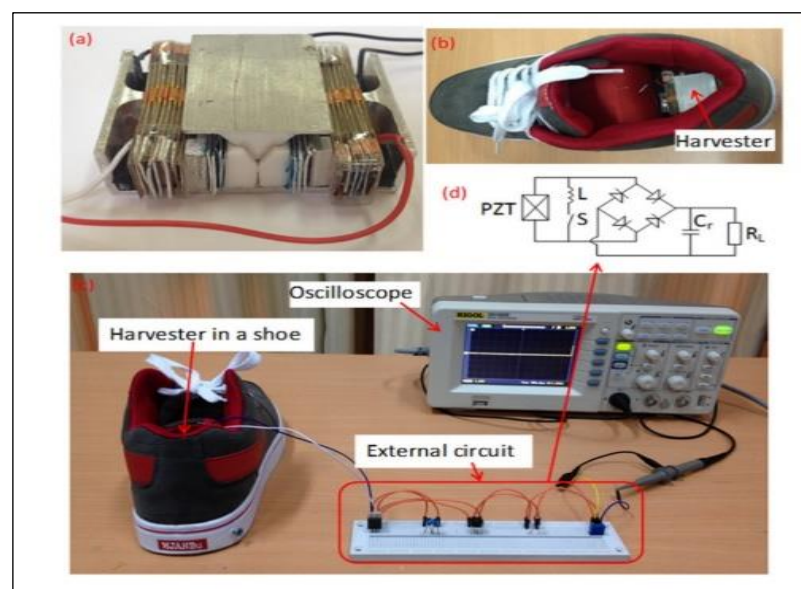


Figure 25: Experimental setup of embedded piezoelectric harvester in a shoes [148]

Pozzi et al. introduced a piezoelectric energy harvester device from knee joint movement of a human body [149]. The device setup is shown in Figure 26. The device structure is an outer ring attached to it 74 plectra and 4 PZT-5H bimorph piezoelectric

cantilevers attached to an inner hub. The developed device was attached to the knee of a walking human where the outer ring is fixed to the thigh and the inner hub is attached to the shank. As a result of the knee movement of a walking human, the harvester produced 2.06 mW using frequency up conversion mechanism.

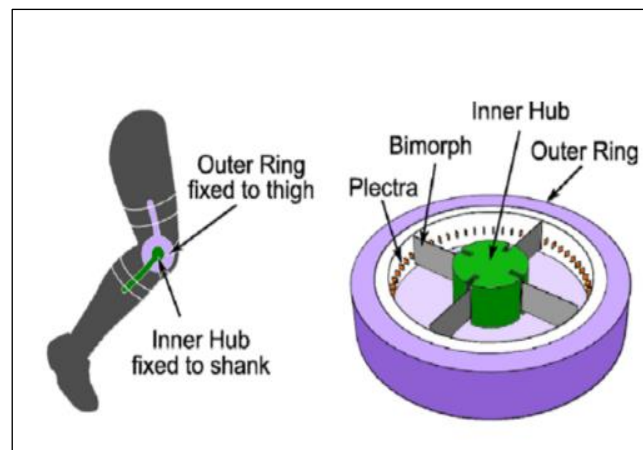


Figure 26: Knee joint piezoelectric harvester. Reproduced with permission from [149]. IOP Publishing, 2012.

Later, in 2016 the same researchers enhanced the knee harvester device to give a higher power output using magnetic plucking mechanism instead of the mechanical plucking mechanism [150]. Results have shown a clear improvement in the power production where the knee joint harvester gave a power of 5.8 mW for a 0.9 Hz of knee joint motion. Some researchers proposed and worked on harvesting energy from the cyclic load of a backpack strap that resulted from human walking activity. Energy harvesting from piezoelectric backpack was proposed first by Granstrom et al. in 2007 [151]. They developed a theoretical model of piezoelectric strap harvester. As shown in Figure 27, straps of PVDF were used and attached to the backpack. Experimental test was done to validate the theoretical model. Results showed that a 444 N load of backpack can produce 45.6 mW power output. In 2008, Feenstra et al. suggested a piezoelectric stack harvester to be installed in a backpack strap. Simulation and

experiment were done and showed that a piezoelectric device of backpack with 220 N can harvest an average power of 0.4 mW [152].



Figure 27: Piezoelectric backpack harvester. Reproduced with permission from [151], IOP Publishing, 2007.

### 2.7.1.2 Implementable devices

Implementable devices have shown immense growth in the medical sector for diagnosing and treating different cases. The limitation of implementable devices lies in their battery life. A periodical need of battery changing can be critical due to the sensitive places where these devices are implemented in such as human heart or knee. The risk of performing a surgery to change the implementable device's battery have caught the researcher's attention to invest and develop in piezoelectric implementable devices.

Zhang et al. utilized a piezoelectric film harvester to generate energy from heart pulses [153]. A sealed flexible PVDF film was used to build the device and implement it in a human heart as clarified in Figure 28. Results were extracted from tests done in labs and tests of a devices being implemented in a human body. Power output of 681 nW and 30 nW were harvested respectively.



Figure 28: Implementable piezoelectric harvester in the heart. Reproduced with permission from [153], Elsevier, 2015.

### 2.7.2 Energy harvested from infrastructure and automobiles

Peigney and his colleagues studied the idea of harvesting energy from traffic vibration on bridges [154]. The case study was based on one of the bridges where they measure the vibration of the bridge by placing accelerometer in different areas of the bridge. The results showed that vibrations at the bridges as a result of moving vehicles had low frequency of less than 15 Hz and small amplitudes. They then placed a bimorph piezoelectric cantilever with a tip mass of 12 g. The results showed that using one harvester can give 0.03 mW power output at the peak of traffic. Jung and his fellows proposed in 2017 a PVDF harvester to be used in the roadway and harvest energy from moving vehicles [155]. The piezoelectric device consists of 6 sets of bimorph harvesters with an overall dimension of  $150 \times 150 \times 90 \text{ mm}^3$  (Figure 29). An experimental work was conducted by mimicking the roadway in a laboratory. Findings showed that for a single vehicle moving 8 km/h and a load of 490.5, 200 mW power was generated.

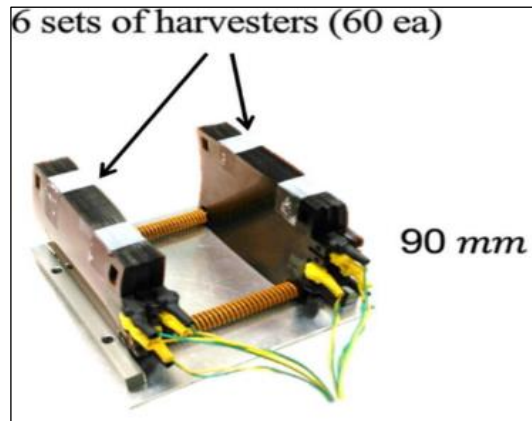


Figure 29: Piezoelectric roadway harvester. Reproduced with permission from [155], Elsevier, 2017.

In 2018, Zhang and his colleagues worked on harvesting energy from a single vehicle moving at 8.3 km/hr [156]. They used a PZT-5H bimorph cantilever at a size of  $100 \times 30 \times 1.4 \text{ mm}^3$ . They found that up to 0.53 mW power can be harvested using this harvester. Gatti et al. conducted a study on another interesting application of harvesting energy from the vibration of the train rail that is caused by a passing train [157]. Numerical and analytical studies were performed. One of the highlighted results in this work is that the harvested energy per mass is proportion to the square of the input base acceleration and the square of the input duration. For frequency of 17 Hz and damping ratio of 0.0045, it was found that the maximum energy per unit mass was about 0.25 J/kg. Furthermore, harvesting energy from aircraft structure has caught the focus of the researchers lately. The dynamic strain produced by the aircraft structure can be utilized in powering the structural health monitoring systems through piezoelectric harvesters. M R Pearson and his colleagues conducted some numerical studies where they showed that optimizing the position and orientation of the piezoelectric harvester can increase the power produced from the aircraft structure [158]. Experimental work was conducted in this study based on different frequency ranges that depend on different conditions of the aircraft like taking off, landing and



cruising. For frequency ranges between 20 to 400 Hz, results showed that the power harvested is in the ranges of 1-1000  $\mu\text{W}$  and RMS power of 0.5-400  $\mu\text{W}$ . The paper stated that the power produced depends on the frequency and the internal resistance of the harvester.

### **2.7.3 Energy harvested from environmental sources**

In 2015, Nan Wu and his colleagues proposed a smart design that can increase the power output of energy harvested from ocean waves [159]. The setup of the harvester consists of a horizontal piezoelectric cantilever attached to the buoy structure as clarifies in Figure 30. The setup works for intermediate to deep ocean levels. A numerical model was developed in their work to obtain the power generated from the buoy harvester. Their results showed that the harvested power increases when the floater in the buoy is thinner and longer and when the sinker is larger. Another important outcome is that the power decreases in a nonlinear pattern with the ratio of the wavelength to the length of the cantilever. The researchers showed that based on their proposed design, 24 W of electrical energy was harvested using 1 m of piezoelectric cantilever and 20 m of buoy length.

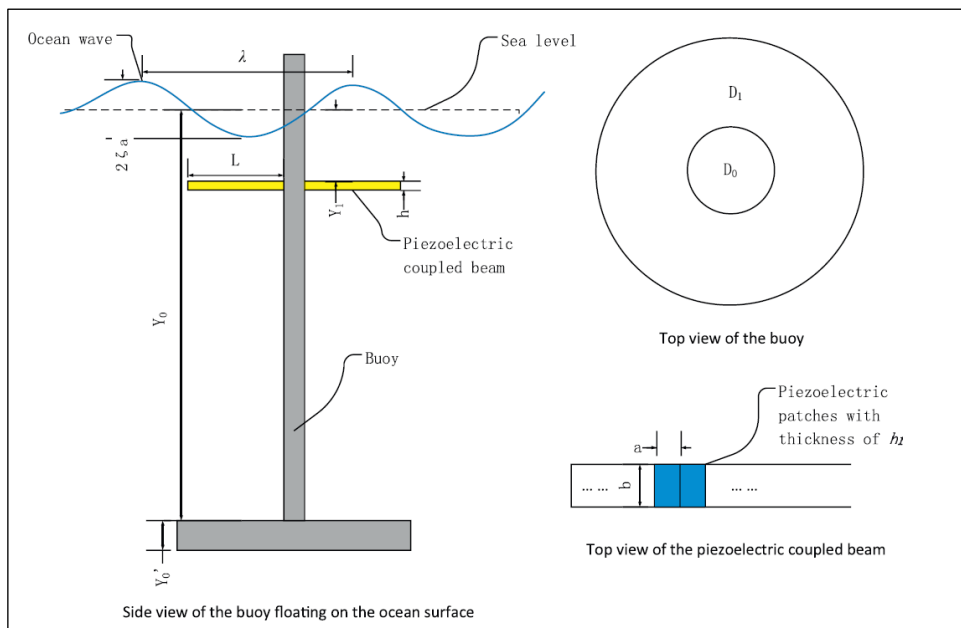


Figure 30: Ocean energy piezoelectric harvester setup. Reproduced with permission from [159], Elsevier, 2015.

### Chapter 3: Mathematical Model

Modeling of the piezoelectric harvesting system is the foundation step to analyze and investigate the harvester performance. Understanding the vibration response behavior through different model approaches assists in improving the harvested power. Thus, this chapter presents the mathematical model developed for a non-uniform piezoelectric harvester with a tip mass using the lumped parameter model (LPM). The electromechanical coupling of a bimorph piezoelectric beam is derived. Static deflection of the LPM is also determined. Lumped parameters like equivalent stiffness, mass and damping are defined. Moreover, the electrical part of the piezoelectric cantilever harvester is presented. A new dimensionless parameter called “power factor” is derived and to be used as a key parameter for designing the optimal piezoelectric harvester. Furthermore, relative tip displacement transmissibility function of the LPM and the DPM for rectangular piezoelectric cantilever is presented for comparison purposes with the Finite element model FEM developed in Chapter 5.

Figure 31 presents a typical bimorph piezoelectric cantilever harvester with tip mass and the corresponding LPM representation. Where  $C$  is the damping,  $K$  is the stiffness and  $V$  is the voltage output from the piezoelectric element. Also,  $y_m$  is the absolute displacement of the mass and  $y$  is the base displacement. The relative tip displacement  $z$  is defined as  $z = y_m - y$ .

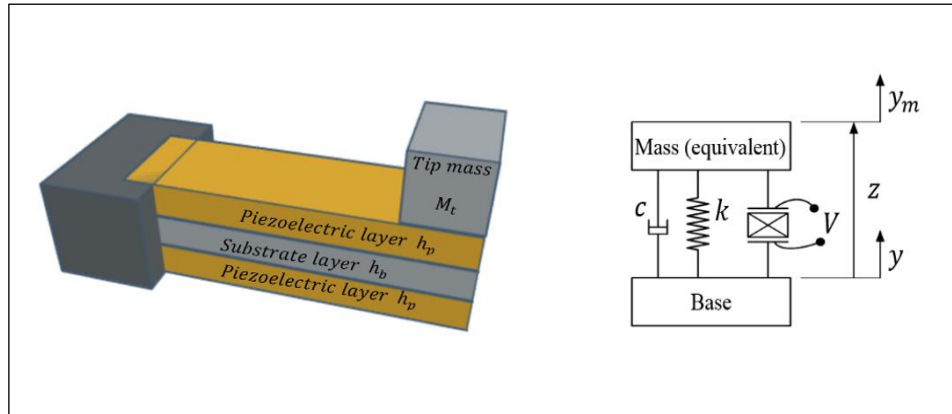
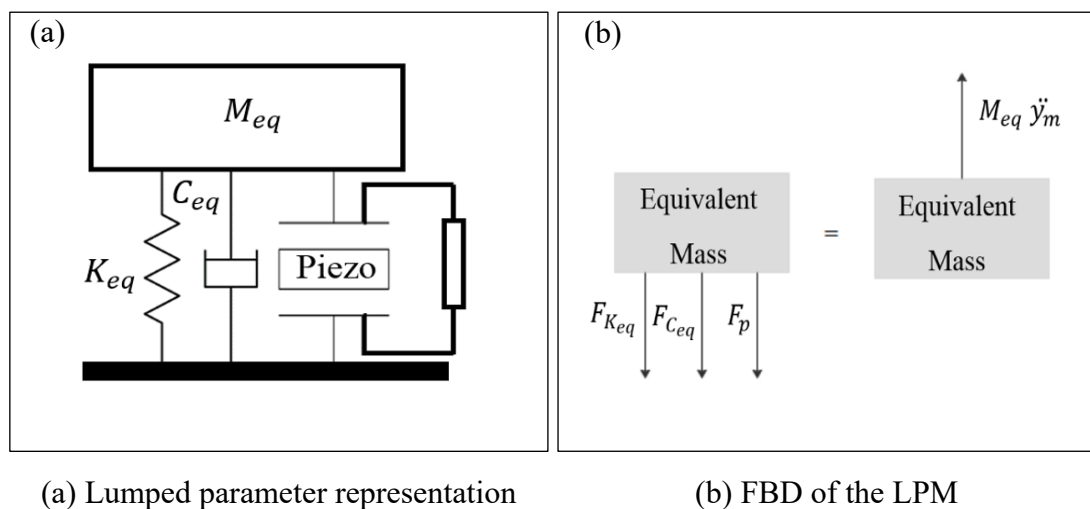


Figure 31: Bimorph piezoelectric cantilever harvester with tip mass and its corresponding mass spring damper model representation

### 3.1 LPM for linearly tapered piezoelectric cantilever

The LPM technique is based on analyzing the dynamics at the tip of the cantilever beam in terms of the lumped parameters [109]. The lumped parameters are equivalent stiffness  $K_{eq}$ , equivalent mass  $M_{eq}$  and equivalent damping  $C_{eq}$  as shown in Figure 32(a). The equivalent stiffness  $K_{eq}$  is determined from the static deflection of the cantilever which results from the load at the tip of the beam. The equivalent mass  $M_{eq}$  is found by presenting the kinetic energy in terms of the beam tip velocity.



(a) Lumped parameter representation

(b) FBD of the LPM

Figure 32: LPM of a piezoelectric cantilever harvester

From the free body diagram (FBD) shown in Figure 32(b), the equation of motion of the LPM is described as:

$$-F_{K_{eq}} - F_{C_{eq}} - F_p = M_{eq}\ddot{y}_m \quad (4)$$

Where  $F_{K_{eq}}$ ,  $F_{C_{eq}}$ ,  $F_p$  are the spring, damping and piezo forces, respectively.  $\ddot{y}_m$  is the acceleration response of mass in the LPM.

Expanding equation (4) results in:

$$-K_{eq}(y_m - y) - C_{eq}(\dot{y}_m - \dot{y}) - F_p = M_{eq}\ddot{y}_m \quad (5)$$

$K$  is the stiffness,  $C$  is the damping,  $y_m$  is the absolute displacement of the mass (at the tip of the cantilever) and  $y$  is the base displacement.

Using the relative tip displacement  $z$  as the following:

$$z = y_m - y$$

$$\dot{z} = \dot{y}_m - \dot{y} \quad (6)$$

$$\ddot{z} = \ddot{y}_m - \ddot{y}$$

Substituting equation (6) in equation (5) results in:

$$-K_{eq}z - C_{eq}\dot{z} - F_p = M_{eq}(\ddot{z} + \ddot{y}) \quad (7)$$

Rearranging equation (7) results in:

$$M_{eq}\ddot{z} + C_{eq}\dot{z} + K_{eq}z + F_p = -M_{eq}\ddot{y} \quad (8)$$

The piezoelectric force  $F_p$  is defined as:

$$F_p = \alpha V \quad (9)$$

Where  $\alpha$  is the electromechanical coupling and  $V$  is the voltage output.

The equation of the electrical system of the piezoelectric harvester is:

$$i = \alpha \dot{z} - C_p \dot{V} \quad (10)$$

Where  $C_p$  is the piezo capacitance.

By rearranging equation (9), the mechanical system equation of the piezoelectric cantilever beam is:

$$M_{eq} \ddot{z} + C_{eq} \dot{z} + K_{eq} z + \alpha V = -M_{eq} \ddot{y} \quad (11)$$

By rearranging equation (10), the electrical system equation of the piezoelectric cantilever beam is:

$$C_p \dot{V} + \frac{V}{R_{eq}} = \alpha \dot{z} \quad (12)$$

Where  $R_{eq}$  is the overall equivalent load resistance.

Equations (11) and (12) are rearranged for state space representation as the following:

$$\ddot{z} = -\frac{C_{eq}}{M_{eq}} \dot{z} - \frac{K_{eq}}{M_{eq}} z - \frac{\alpha}{M_{eq}} V - \ddot{y} \quad (13)$$

$$\dot{V} = -\frac{V}{R_{eq} C_p} + \frac{\alpha}{C_p} \dot{z} \quad (14)$$

Defining a new variable as:

$$u = \dot{z} \quad (15)$$

$$\dot{u} = \ddot{z}$$

Substituting equation (15) in equation (13) gives:

$$\dot{u} = -\frac{C_{eq}}{M_{eq}}u - \frac{K_{eq}}{M_{eq}}z - \frac{\alpha}{M_{eq}}V - \ddot{y} \quad (16)$$

Substituting equation (15) in equation (14) gives:

$$\dot{V} = -\frac{1}{R_{eq}C_p}V + \frac{\alpha}{C_p}u \quad (17)$$

The state space representation of the electromechanical piezoelectric harvester is given by:

$$\begin{bmatrix} \dot{z} \\ \dot{u} \\ \dot{V} \end{bmatrix} = \begin{bmatrix} 0 & 1 & 0 \\ -\frac{K_{eq}}{M_{eq}} & -\frac{C_{eq}}{M_{eq}} & -\frac{\alpha}{M_{eq}} \\ 0 & \frac{\alpha}{C_p} & -\frac{1}{R_{eq}C_p} \end{bmatrix} \begin{bmatrix} z \\ u \\ V \end{bmatrix} + \begin{bmatrix} 0 \\ -1 \\ 0 \end{bmatrix} \ddot{y} \quad (18)$$

$$\begin{bmatrix} z \\ u \\ V \end{bmatrix} = \begin{bmatrix} 1 & 0 & 0 \\ 0 & 1 & 0 \\ 0 & 0 & 1 \end{bmatrix} \begin{bmatrix} z \\ u \\ V \end{bmatrix} + \begin{bmatrix} 0 \\ 0 \\ 0 \end{bmatrix} \ddot{y} \quad (19)$$

### 3.1.1 Electromechanical coupling

The performance of the piezoelectric harvesters depends primarily on the electromechanical coupling effect. The derivation of an electromechanical coupling of a non-uniform piezoelectric cantilever beam is described below. Figure 33 shows a representation of a piezoelectric element.

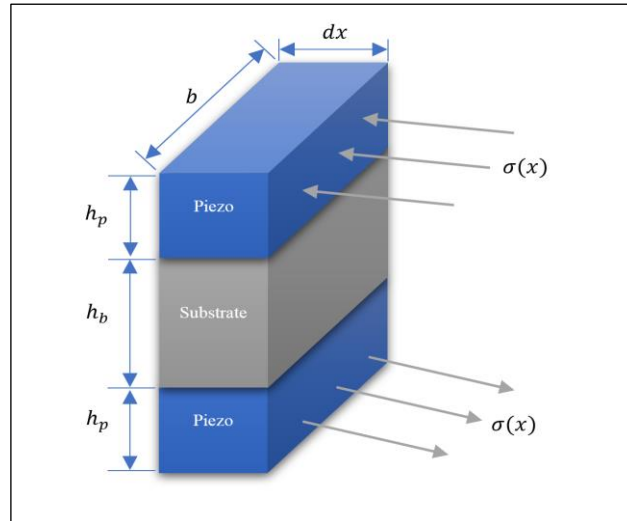


Figure 33: A schematic of a piezoelectric element

Recall the definition of electric displacement of the piezoelectric element is given as:

$$D = d_{31}\sigma_p + \varepsilon_{33}^T E_3 \quad (20)$$

Where  $d_{31}$  is a piezoelectric constant and  $\sigma_p$  is the piezo stress.  $\varepsilon_{33}^T$  is the permittivity at a constant stress and  $E_3$  is the electric field.

$\varepsilon_{33}^T$  is defined as:

$$\varepsilon_{33}^T = \varepsilon_{33}^S + d_{31}E_p \quad (21)$$

Where  $\varepsilon_{33}^S$  is the permittivity at a constant strain and  $E_p$  is the piezoelectric modulus of elasticity. Rearranging equation (20) in terms of  $\varepsilon_{33}^S$  gives [125]:

$$D = d_{31}\sigma_p + \varepsilon_{33}^S E_3 \quad (22)$$

Where  $E_3$  is given for a parallel connection as:

$$E_3 = -\frac{V(t)}{h_p} \quad (23)$$



For an element in a piezoelectric cantilever beam, the displacement charge becomes:

$$dD(x) = d_{31}\sigma_p(x) - \varepsilon_{33}^s \frac{V(t)}{h_p} \quad (24)$$

Where  $\sigma_p(x)$  is the stress of piezo element at  $x$  position and is defined as:

$$\sigma_p(x) = \frac{M(h_b + h_p)}{2I_{tot}(x)} \quad (25)$$

Where  $M$  is the bending moment,  $h_b$  is the beam thickness  $h_p$  is the piezoelectric thickness.

$I_{tot}$  is the total area moment of inertia of the cantilever beam cross-section which is given by:

$$I_{tot} = \frac{b(x)(h_b + 2h_p)^3}{12} \quad (26)$$

Where  $b(x)$  is the width function varying along the length of the tapered piezoelectric cantilever beam.

For static deflection curvature assumption, the bending moment  $M$  can be assumed due to an applied force  $F$  as:

$$M = F(L - x) \quad (27)$$

Equation (24) can be rewritten as:

$$\frac{dQ}{dx \cdot b(x)} = d_{31} \cdot \frac{F(L - x)(h_b + h_p)}{2I_{tot}} - \varepsilon_{33}^s \frac{V(t)}{h_p} \quad (28)$$

Where  $Q$  is the electric charge of the piezoelectric element. Substituting  $I_{tot}$  (equation (26)) gives the following expression:

$$\frac{dQ}{dx \cdot b(x)} = \frac{6d_{31}(h_b + h_p)}{b(x)(h_b + 2h_p)^3} \cdot F(L - x) - \varepsilon_{33}^s \frac{V(t)}{h_p} \quad (29)$$

Rearranging equation (29) gives:

$$dQ = \frac{6d_{31}(h_b + h_p)}{(h_b + 2h_p)^3} \cdot F(L - x)dx - \varepsilon_{33}^s \frac{V(t)}{h_p} b(x)dx \quad (30)$$

The total electric charge  $Q$  for the two piezoelectric layers is described as:

$$Q = 2 \int_L dQ = \left[ \frac{6d_{31}(h_b + h_p)}{(h_b + 2h_p)^3} \right] \cdot F \int_0^L (L - x) dx - 2\varepsilon_{33}^s \frac{V(t)}{h_p} \int_0^L b(x) dx \quad (31)$$

$$Q = \frac{6d_{31}(h_b + h_p)L^2}{(h_b + 2h_p)^3} \cdot F - V(t) \frac{2\varepsilon_{33}^s}{h_p} \int_0^L b(x) dx \quad (32)$$

Where the  $\frac{2\varepsilon_{33}^s}{h_p} \int_0^L b(x) dx$  term represents the capacitor of the piezoelectric element.

Considering an equivalent model and tip displacement,  $F$  is defined as:

$$F = K_{eq} \cdot z \quad (33)$$

Substituting  $F$  in equation (32) gives:

$$Q = \frac{6d_{31}(h_b + h_p)L^2}{(h_b + 2h_p)^3} \cdot K_{eq} \cdot z - V(t) \frac{2\varepsilon_{33}^s}{h_p} \int_0^L b(x) dx \quad (34)$$

Differentiating the electric charge with relative to time results in current which is defined as:

$$i = \frac{6d_{31}(h_b + h_p)L^2}{(h_b + 2h_p)^3} \cdot K_{eq} \cdot \dot{z} - \dot{V}(t) \frac{2\varepsilon_{33}^S}{h_p} \int_0^L b(x) dx \quad (35)$$

The above current equation matches equation (10). Thus, the electromechanical coupling equation  $\alpha$  is defined by:

$$\alpha = \frac{6d_{31}(h_b + h_p)}{(h_b + 2h_p)^3} \cdot L^2 K_{eq} \quad (36)$$

### 3.1.2 Static deflection and equivalent stiffness $K_{eq}$

In modeling the piezoelectric cantilever using the LPM, the equivalent stiffness  $K_{eq}$  is determined from the static deflection. The following equations represent the derivation of the static deflection.

For a cantilever beam, the bending moment is given as:

$$M = EI(x) \frac{\partial^2 y}{\partial x^2} \quad (37)$$

Where  $EI(x)$  is the bending stiffness and  $y$  is the displacement in the beam lateral direction.

Recalling equation (27) and substituting it in equation (37) gives:

$$\frac{d^2 y}{dx^2} = \frac{M}{EI(x)} = \frac{12F(L-x)}{Eb(x)(h_b + 2h_p)^3} \quad (38)$$

Rearranging equation (38) results in:

$$\frac{d^2y}{dx^2} = \frac{12F}{E(h_b + 2h_p)^3} \cdot \left[ \frac{L-x}{b(x)} \right] \quad (39)$$

Defining  $f(x)$  as:

$$f(x) = \frac{(L-x)}{b(x)} \quad (40)$$

Substituting equation (40) in equation (39) gives:

$$\frac{d^2y}{dx^2} = \frac{12F}{E(h_b + 2h_p)^3} \cdot f(x) \quad (41)$$

Integrating  $\frac{d^2y}{dx^2}$  results in:

$$\frac{dy}{dx} = \int_0^x \frac{12F}{E(h_b + 2h_p)^3} \cdot f(x) dx \quad (42)$$

Then, the equation of the beam lateral displacement in  $y$  direction at  $x$  position from the fixed end of the piezoelectric cantilever beam is:

$$y(x) = \frac{12F}{E(h_b + 2h_p)^3} \iint_0^x f(x) dx \cdot dx \quad (43)$$

The deflection at the tip of the cantilever is defined as:

$$y_{tip} = y(L) \quad (44)$$

and  $F$  is defined as:

$$F = K_{eq} \cdot y_{tip} \quad (45)$$

Substituting equations (44) and (45) in equation (43) gives:

$$y_{tip} = \frac{12 \cdot K_{eq} y_{tip}}{E(h_b + 2h_p)^3} \int_0^L \int_0^x f(x) dx \cdot dx \quad (46)$$

The equation of equivalent stiffness  $K_{eq}$  is given by:

$$K_{eq} = \frac{E(h_b + 2h_p)^3}{12} \cdot \frac{1}{\int_0^L \int_0^x \frac{(L-x)}{b(x)} dx \cdot dx} \quad (47)$$

The equation of average modulus of elasticity is given by:

$$E = \frac{12 \left[ \frac{E_b h_b^3}{12} - \frac{2E_p}{3} \left( \frac{h_b^3}{8} - \left( \frac{h_b}{2} + h_p \right)^3 \right) \right]}{(h_b + 2h_p)^3} \quad (48)$$

Where  $E_b$  and  $E_p$  are the modulus of elasticity of beam and piezoelectric layer respectively.

### 3.1.3 Equivalent mass $M_{eq}$

The equivalent mass  $M_{eq}$  is determined from the velocity of the element at the tip of the cantilever beam. This subsection will show the derivation of the total kinetic energy to find the equivalent mass parameter. It is important to highlight that the static deflection is going to be presented here in a simpler form than the previous section for the completeness and clarity of the content.

Equation (42) can be presented as the slope of the free vibration equation given by:

$$\theta = \int_0^x \frac{F(L-x)}{EI(x)} dx \quad (49)$$

Where bending stiffness equation is expressed by [15] as:

$$EI(x) = b(x) \left[ E_b \left( \frac{h_b^3}{12} \right) + \frac{E_p}{3} \left( \left( \frac{h_b}{2} + h_p \right)^3 - \frac{h_b^3}{8} \right) \right] \quad (50)$$

The width function of the tapered piezoelectric cantilever is given by:

$$b(x) = b_0 + \left( \Delta b \left( \frac{x}{L} \right) \right) \quad (51)$$

Where  $b_0$  is the width at the root of the cantilever and  $\Delta b$  is defined by:

$$\Delta b = (r b_0) - b_0 \quad (52)$$

Where  $r$  is the beam taper ratio which is defined as:

$$r = \frac{b_l}{b_0} \quad (53)$$

Where  $b_l$  is the width at the tip of the cantilever.

The slope at the tip of the cantilever beam when  $x=L$  is:

$$\theta_l = \int_0^L \frac{F(L-x)}{EI(x)} dx \quad (54)$$

Integrating (49) will give the deflection at any section of the beam in terms of  $x$  as:

$$y(x) = \iint_0^x \frac{F(L-x)}{EI(x)} dx \cdot dx \quad (55)$$

Integrating (54) will give the deflection at the tip of the beam when  $x=L$  as:

$$y_{tip} = \iint_0^L \frac{F(L-x)}{EI(x)} dx \cdot dx \quad (56)$$

Normalized deflection is expressed by:

$$y_n = \frac{y(x)}{y_{tip}} \quad (57)$$

The equation of mass per unit length of the piezoelectric beam is:

$$m(x) = b(x)(2\rho_p h_p + \rho_b h_b) \quad (58)$$

Where  $\rho_p$  is the piezoelectric density  $\rho_b$  is the beam density.

To find the equivalent mass  $M_{eq}$ , the velocity of small element is determined by:

$$v(x) = \frac{dy(x)}{dt} \quad (59)$$

The kinetic energy “KE” of the piezoelectric cantilever element is:

$$d(KE) = \frac{1}{2} m(x) dx \times v(x)^2 \quad (60)$$

Integrating equation (60) to determine the total kinetic energy as:

$$KE = \frac{1}{2} \int_0^L m(x) v(x)^2 dx \quad (61)$$

For the LPM, equivalent beam mass ' $m_b$ ' should have the same beam kinematic energy and as placed at the beam tip position which has the maximum velocity.

Accordingly:

$$KE = \frac{1}{2} m_b v_{max}^2 \quad (62)$$

Rearranging equation (62) defines the equivalent beam mass as:

$$m_b = \frac{\int_0^L m(x) v(x)^2 dx}{v_{max}^2} \quad (63)$$

Using equations (58), (59) and (63), the equivalent beam mass is given as:

$$m_b = \frac{\int_0^L b(x) (2\rho_p h_p + \rho_b h_b) \left( \frac{dy(x)}{dt} \right)^2 dx}{v_{max}^2} \quad (64)$$

Substituting equation (55) of  $y(x)$  in (64) results in:

$$m_b = \frac{(2\rho_p h_p + \rho_b h_b)}{v_{max}^2} \int_0^L b(x) \left[ \frac{d}{dt} \left( \iint_0^x \frac{F(L-x)}{EI(x)} dx \cdot dx \right) \right]^2 dx \quad (65)$$

The total equivalent mass equation  $M_{eq}$  of a piezoelectric cantilever with a tip mass is:

$$M_{eq} = M_t + m_b \quad (66)$$

Where  $M_t$  is the mass placed at the tip of the piezoelectric cantilever beam

### 3.1.4 Equivalent damping $C_{eq}$

The equivalent damping of the LPM can be expressed as:

$$C_{eq} = 2\zeta\omega_n M_{eq} \quad (67)$$



Where  $\zeta$  is the damping ratio and  $\omega_n$  is the natural frequency

### 3.1.5 Natural frequency $\omega_n$

The natural frequency equation of the LPM is given by:

$$\omega_n = \sqrt{\frac{K_{eq}}{M_{eq}}} \quad (68)$$

### 3.2 Electric circuit

There electrical part in the piezoelectric harvester can be connected in series or parallel as shown in Figure 34.

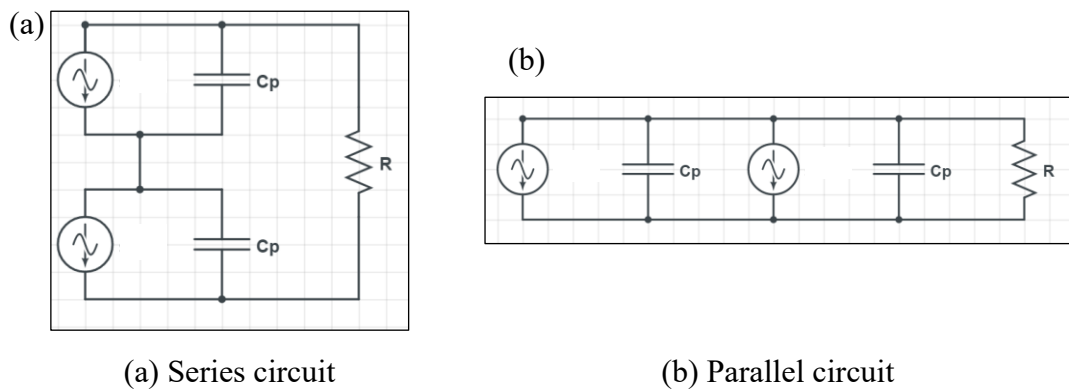


Figure 34: Electric circuit schematics of the piezoelectric harvester

The equation of capacitance is defined as:

$$\text{Parallel: } C_p = 2 \frac{\epsilon_{33}^S \cdot A}{h_p} \quad (69)$$

$$\text{Series: } C_p = \frac{\epsilon_{33}^S \cdot A}{2h_p} \quad (70)$$

Where  $A$  is the cantilever surface area (the piezo material area) and is given as:

$$A = \int_0^L b(x) dx \quad (71)$$

Substitute “ $A$ ” in equations (69) and (70) yields,

$$\text{Parallel: } C_p = \frac{2\varepsilon_{33}^S}{h_p} \int_0^L b(x) dx \quad (72)$$

$$\text{Series: } C_p = \frac{\varepsilon_{33}^S}{2h_p} \int_0^L b(x) dx \quad (73)$$

The equivalent load resistance  $R_{eq}$  of the piezoelectric harvester is obtained by deriving the power output with respect to the load resistance.  $R_{eq}$  is defined as:

$$R_{eq} = \frac{1}{\omega_n C_p} \quad (74)$$

### 3.3 Power factor

To analyze the performance of different piezoelectric harvesters' configurations, an accurate comparison parameter should be chosen. Developing the right key parameter for the comparison process gives a credibility to the study. In this section, a comparison parameter named as “power factor (PF)” is developed and used for different investigations carried throughout the thesis.

The power output of the piezoelectric cantilever beam is given as:

$$P = I^2 R_{eq} \quad (75)$$

Substituting equations (35) and (74) into (75) gives the exact solution of the power output for a piezoelectric cantilever harvester as:

$$P = \frac{M_{eq}^2 R_{eq} \omega_n^2 \alpha^2}{(R_{eq} \omega_n \alpha^2 + C_{eq} \omega_n)^2 + C_p^2 C_{eq}^2 R_{eq}^2 \omega_n^4} \quad (76)$$

In order to understand the performance of different piezoelectric cantilever configurations, a dimensionless parameter called power factor 'PF' is developed. The power factor parameter will be used as a key parameter in developing and reaching the optimal piezoelectric harvester.

The power factor parameter is defined as:

$$PF = P \left( \frac{\omega_n}{M_{eq}} \right) \quad (77)$$

Substituting equations (74) and (76) in equation (77) and rearranging results in:

$$PF = \frac{M_{eq} \omega_n^2 \alpha^2}{C_p \left[ \left( \frac{\alpha^2}{C_p} + C_{eq} \omega_n \right)^2 + C_{eq}^2 \omega_n^2 \right]} \quad (78)$$

Considering that  $\frac{\alpha^2}{C_p}$  is a very small value that can be ignored. Thus, the power factor will be reduced to the following expression:

$$PF = \frac{\mu_{eq} \alpha^2}{2 C_p C_{eq}^2} \quad (79)$$

Substituting the equivalent capacitance  $C_{eq}$  in equation (79) gives:

$$PF = \frac{\alpha^2}{8 K_{eq} \zeta^2 C_p} \quad (80)$$

Substituting the electromechanical coupling  $\alpha$  (equation (36)) and capacitance  $C_p$  (equation (69)) in equation (80) gives:

$$PF = \frac{\left[ \frac{3 d_{31}(h_b + h_p)}{(h_b + 2h_p)^3} \right]^2 L^4 K_{eq}^2}{8k_{eq}\zeta^2 \left( \frac{2\varepsilon_{33}^S}{h_p} \right) \cdot \int_0^L b(x) dx} \quad (81)$$

Substitute equivalent stiffness  $k_{eq}$  (equation (47)) in equation (81) gives the closed form of the power factor to be as:

$$PF = \frac{9h_p}{16\varepsilon_{33}^S\zeta^2} \cdot \left[ \frac{d_{31}(h_b + h_p)}{(h_b + 2h_p)^3} \right]^2 \cdot \frac{L^4 \cdot E(h_b + 2h_p)^3}{\left[ \int_0^L b(x) dx \right]^2 \cdot 12 \int_0^L \int_0^x f(x) dx \cdot dx} \quad (82)$$

To understand the effect of the thickness on the power factor of different piezoelectric harvesters' shapes, A power factor expression was developed in terms of the piezoelectric harvesters' thickness ratio.

The thickness ratio is defined as:

$$t_p = \frac{h_p}{h_b} \quad (83)$$

Substituting the thickness ratio in the power factor equation (82) gives:

$$PF = \frac{3E d_{31}^2}{64\varepsilon_{33}^S\zeta^2} \cdot \left[ \frac{t_p h_b (h_b + t_p h_b)^2}{(h_b + 2t_p h_b)^3} \right] \cdot \frac{L^4}{\left[ \int_0^L b(x) dx \right] \left[ \int_0^L \int_0^x f(x) dx \cdot dx \right]} \quad (84)$$

Rearranging the equation gives the closed form of the power factor in terms of the thickness ratio to be as:

$$PF = \frac{3E d_{31}^2}{64\varepsilon_{33}^s \zeta^2} \cdot \left[ \frac{t_p (1 + t_p)^2}{(1 + 2t_p)^3} \right] \cdot \frac{L^4}{\left[ \int_0^L b(x) dx \right] \left[ \int_0^L \int_0^x f(x) dx \cdot dx \right]} \quad (85)$$

### 3.4 Relative transmissibility function of the piezoelectric cantilever harvester models

In order to understand the role of the correction factor in improving the precision of the LPM, it is important to know the difference between the response of the DPM and LPM models of the piezoelectric cantilever harvesters. As discussed in the literature review, the transmissibility function is used as a comparison tool between the LPM and DPM. This section presents a review of the mathematical expressions of the transmissibility functions for the rectangular and exponentially tapered piezoelectric beams [109], [127]. The steady state response of harmonic base excitation for both LPM and DPM are discussed. Also, representations of the transmissibility functions along with the correction factor estimation are presented.

#### 3.4.1 Rectangular piezoelectric cantilever harvesters

The steady state response of the relative tip displacement under harmonic base excitation for the DPM is given by [109]:

$$z^{DPM}(L, t) = 2\omega^2 Y_0 e^{j\omega t} \sum_{r=1}^{\infty} \frac{\sigma_r [\cos \lambda_r - \cosh \lambda_r + \sigma_r (\sin \lambda_r - \sinh \lambda_r)]}{\lambda_r (\omega_r^2 - \omega^2 + j2\zeta_r \omega_r \omega)} \quad (86)$$

Where  $\omega$  is the excitation frequency,  $\omega_r$  is the undamped natural frequency of the  $r$ th mode shape,  $Y_0$  is the base displacement amplitude,  $\zeta_r$  is the damping coefficient of the  $r$ th mode shape, and  $\lambda_r$  is the dimensionless frequency parameter of the  $r$ th mode.

The dimensionless frequency  $\lambda_r$  is given by the characteristic equation as:

$$1 + \cos \lambda \cosh \lambda = 0 \quad (87)$$

The undamped natural frequency of the  $r$ th mode shape is defined as:

$$\omega_r = \lambda_r^2 \sqrt{\frac{EI}{mL^4}} \quad (88)$$

and,  $\sigma_r$  is defined as:

$$\sigma_r = \frac{\sin \lambda_r - \sinh \lambda_r}{\cos \lambda_r + \cosh \lambda_r} \quad (89)$$

The steady state response of the relative tip displacement for the LPM is expressed by:

$$z^{LPM}(t) = \frac{\omega^2}{\omega_n^2 - \omega^2 + j2\zeta\omega_n\omega} Y_0 e^{j\omega t} \quad (90)$$

Note that  $z^{LPM}(t) = y_m(t) - y(t)$ .  $y(t)$  is given as  $y(t) = Y_0 e^{j\omega t}$ .  $\omega_n$  is the natural frequency of the LPM. The transmissibility function is given by the ratio of the relative tip displacement  $z^{LPM}(t)$  to base displacement  $y(t)$ . The relative tip displacement transmissibility function of the DPM can be expressed as:

$$T_{rel}^{DPM}(\omega, \zeta_r) = 2\omega^2 \sum_{r=1}^{\infty} \frac{\sigma_r [\cos \lambda_r - \cosh \lambda_r + \sigma_r (\sin \lambda_r - \sinh \lambda_r)]}{\lambda_r (\omega_r^2 - \omega^2 + j2\zeta_r \omega_r \omega)} \quad (91)$$

The relative tip displacement transmissibility function of the LPM is given by:

$$T_{rel}^{LPM}(\omega, \zeta) = \frac{\omega^2}{\omega_n^2 - \omega^2 + j2\zeta\omega_n\omega} \quad (92)$$

Reducing equation (91) to consider only the desired first mode gives the following:

$$\hat{T}_{rel}^{DPM}(\Omega, \zeta) = \frac{\mu_1 \omega^2}{\omega_1^2 - \omega^2 + j2\zeta\omega_1\omega} \quad (93)$$

Which can be stated as:

$$\hat{T}_{rel}^{DPM}(\Omega, \zeta) = \frac{\mu_1 \Omega^2}{1 - \Omega^2 + j2\zeta\Omega} \quad (94)$$

Where  $\Omega$  is normalized frequency defined as:

$$\Omega = \frac{\omega}{\omega_1} \cong \frac{\omega}{\omega_n} \quad (95)$$

$\mu_1$  is the estimated correction factor of rectangular piezoelectric cantilever harvester with no tip mass. The correction factor of the first mode shape is given by

$$\mu_1 = \frac{2\sigma_1[\cos \lambda_1 - \cosh \lambda_1 + \sigma_1(\sin \lambda_1 - \sinh \lambda_1)]}{\lambda_1} \cong 1.566 \quad (96)$$

Correction factor estimation in the presence of mass ratio (tip mass/ beam mass) is obtained by [109] as:

$$\mu_1 = \phi_1(L) \left( M_t \phi_1(L) + m \int_0^L \phi_1(x) dx \right) \quad (97)$$

Where ‘ $m$ ’ is the beam mass per unit length and  $\phi_1$  is the eigenfunction of the first mode shape.

The eigenfunctions  $\phi_r$  of a uniform cantilever beam with mass attached at the tip is defined by:

$$\phi_r(x) = A_r \left( \cos \frac{\lambda_r}{L} x - \cosh \frac{\lambda_r}{L} x + \zeta_r \left( \sin \frac{\lambda_r}{L} x - \sinh \frac{\lambda_r}{L} x \right) \right) \quad (98)$$

Where  $\zeta_r$  is expressed by:

$$\zeta_r = \frac{\sin \lambda_r - \sinh \lambda_r + \lambda_r \frac{M_t}{mL} (\cos \lambda_r - \cosh \lambda_r)}{\cos \lambda_r + \cosh \lambda_r - \lambda_r \frac{M_t}{mL} (\sin \lambda_r - \sinh \lambda_r)} \quad (99)$$

The relative error of the uncorrected lumped parameter at the tip is calculated as:

$$\text{Relative Error (\%)} = \frac{1 - \mu_1}{\mu_1} \times 100 \quad (100)$$



## Chapter 4: Experimental Setup

In this chapter, the experimental setup of a bimorph piezoelectric cantilever harvester is presented. Geometric and material properties used in the experiment are listed in Table 7. A detailed explanation of each instrument used in the experiment is covered as well. The chapter concludes with experimental results of a rectangular piezoelectric beam. Results like voltage and power output of analytical and experimental work are validated and shown. Figure 35 shows the experimental setup of the piezoelectric cantilever harvester.

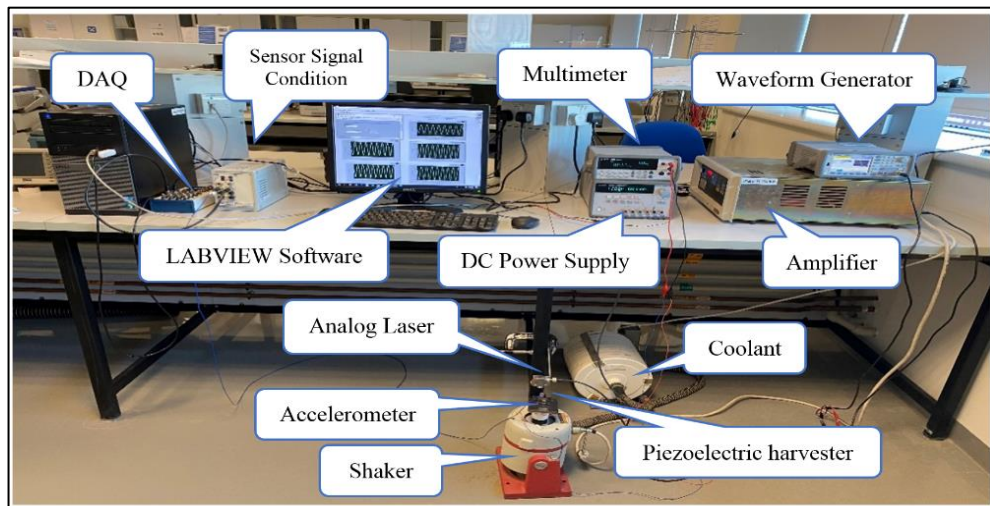


Figure 35: Experimental setup of the piezoelectric cantilever harvester

### 4.1 Experimental process

Figure 36 presents the process flow diagram of the experiment. The vibration source used for the piezoelectric harvester is an LDS shaker from Brüel & Kjær connected to a coolant fan. The input excitation is fed to the shaker using an external waveform generator from Keysight type (33500B series). The external wave generator signal is amplified through the shaker driving amplifier. A PZT-5H bimorph cantilever from PIEZO.com is attached to a fixture and placed on the shaker head. An

accelerometer from PCB Piezotronics.com model (352C04) is attached to the shaker head to measure the cantilever base input acceleration. The accelerometer signal is then amplified using sensor signal condition from PCB Piezotronics.com model (442B104). A Q4X analog laser sensor is placed vertically aligned with the tip of the piezoelectric cantilever to measure the tip displacement of the vibrated beam. The analog laser is powered by a DC power supply from Agilent (model type E3631A). The piezoelectric cantilever output electrodes are connected to a digital multimeter from Agilent type (34405A) which is then connected to the Labview software. The signals coming from the analog laser and the accelerometer are connected to a Data Acquisition System (DAQ) from national instruments type USB (6212). Results of base acceleration, piezoelectric tip displacement and voltages are processed and displayed through LabVIEW software in the computer.

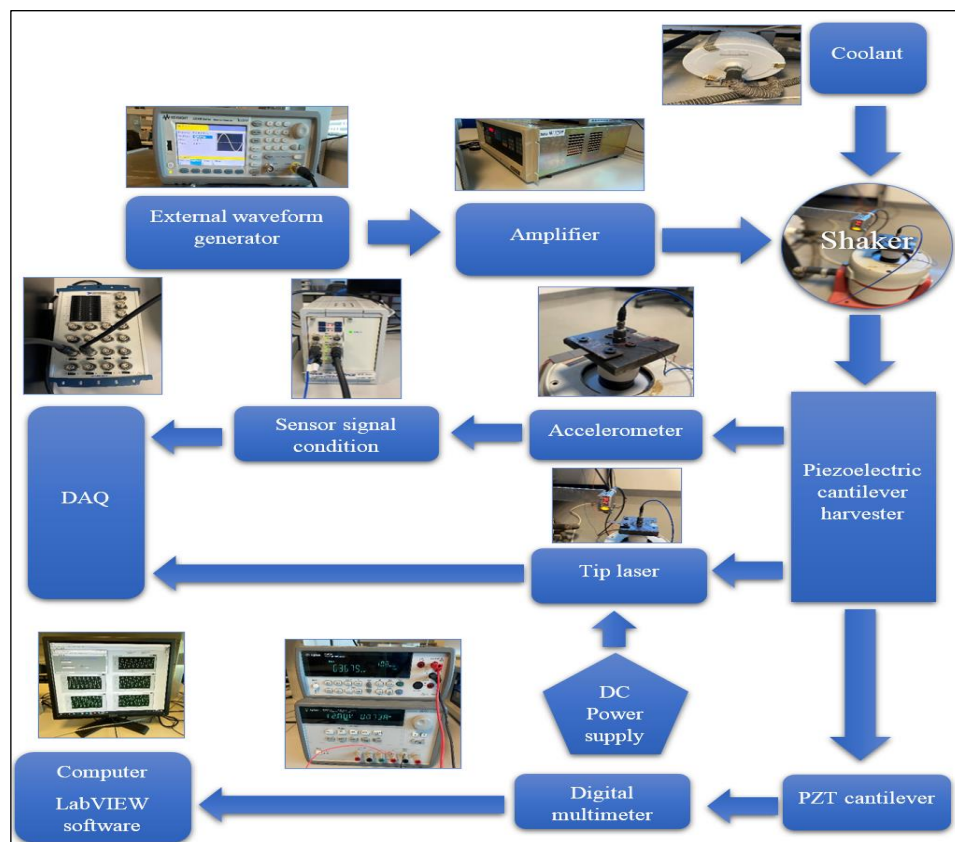


Figure 36: Process flow diagram of experimental piezoelectric energy harvesting

## 4.2 Piezoelectric cantilever beam setup

Figure 37 shows a close-up picture of the piezoelectric cantilever attached to the shaker. The piezoelectric cantilever and the accelerometer are placed on a metal piece that is attached to the shaker head. The piezoelectric bimorph cantilever is placed in a grooved bedding and fixed using a small metal piece and two bolts. An accelerometer is placed in the middle of the metal setup. The analog laser is placed vertically to measure the tip displacement.



Figure 37: Close-up picture of piezoelectric cantilever harvester setup attached to a shaker

Figure 38 shows PZT-5H bimorph cantilever purchased from PIEZO.com part number (Q220-H4BR-1305YB). Table 7 specifies all the geometric and the material properties of the PZT-5H bimorph harvester [160].

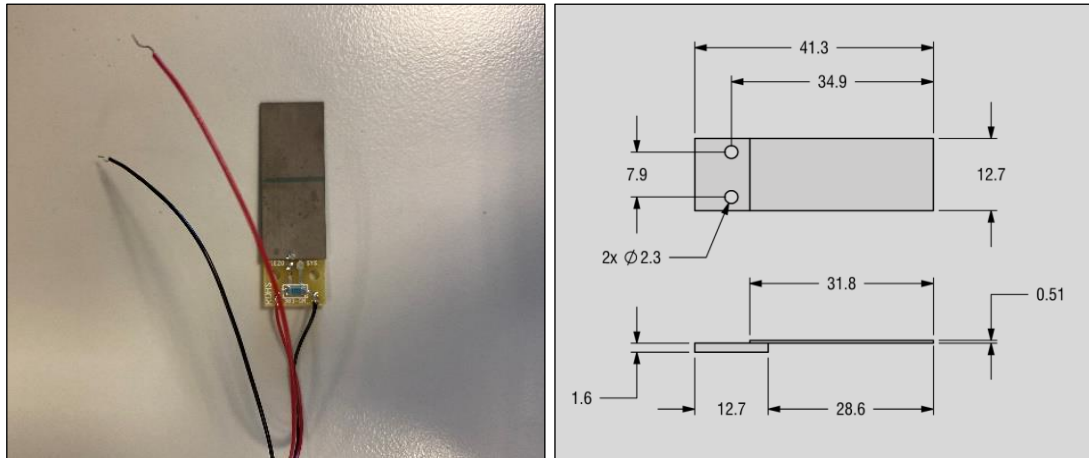


Figure 38: PZT-5H bimorph piezoelectric cantilever and its corresponding dimensions from the factory [160]

Table 7: Geometrical and material properties of PZT-5H bimorph cantilever used in the experiment

Properties	Piezo material	Beam material (Brass)
Modulus of elasticity (Pa)	$62 \times 10^9$	$100 \times 10^9$
Density (kg/m <sup>3</sup> )	7800	8300
Piezo constant coupling (m/V) or (c/N)	$-320 \times 10^{-12}$	-
Length (m)	$31.8 \times 10^{-3}$	$31.8 \times 10^{-3}$
Width (m)	$12.7 \times 10^{-3}$	$12.7 \times 10^{-3}$
Thickness (m)	$0.19 \times 10^{-3}$ (each layer)	$0.13 \times 10^{-3}$
Vacuum Permittivity (F/m) “ $e_0$ ”	$8.854 \times 10^{-12}$	-
Permittivity (F/m)	$3800 \times e_0$	-
Capacitance (F)	$96 \times 10^{-9}$	-
Poisson ratio	-	0.32
Ultimate Tensile Strength (Pa)	-	$800 \times 10^6$
Tensile Yield Strength (Pa)	-	$500 \times 10^6$

### 4.3 Data acquisition system (DAQ)

Data acquisition system is an interface between the computer and the signals coming from the experiment. It is run and controlled using LABVIEW. LABVIEW program is written to accomplish the experiment data collection. In this experiment, two types of signals are connected to the DAQ. The first signal comes from the accelerometer which is the base acceleration and the second signal is the tip mass displacement. Figure 39 shows the LABVIEW program used to measure the base acceleration and tip displacement of the experiment.

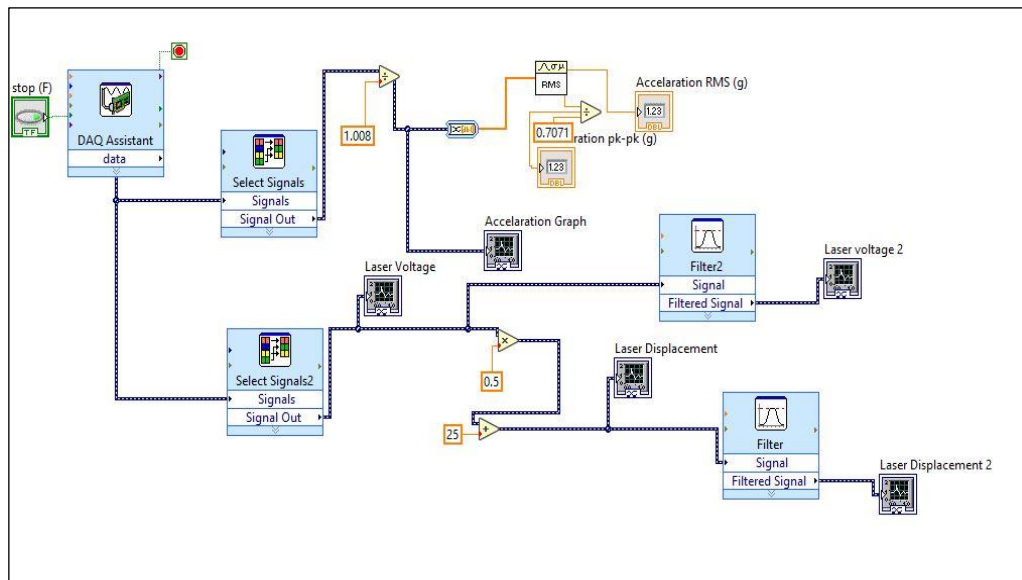


Figure 39: A screenshot of LABVIEW software

### 4.4 Validation using experimental analysis

This section presents the experimental results of rectangular piezoelectric cantilever. Validations between experimental results and analytical results are shown. The frequency response function (FRF) voltage and power are analyzed. The tested piezoelectric beam was in the frequency range of 20-400 Hz where the 1<sup>st</sup> mode of resonance frequency was examined. The experimental results were under an open

circuit condition. The damping coefficient was also measured from an experiment test. The properties of PZT-5H used in the experiment are available in Table 7. It is important to mention that the overhang length of the piezoelectric cantilever is 26.6mm.

The input base acceleration was measured using an accelerometer placed in the middle of the piezoelectric harvester setup. The input excitation acceleration was set at 1g pk-pk as shown in Figure 40.

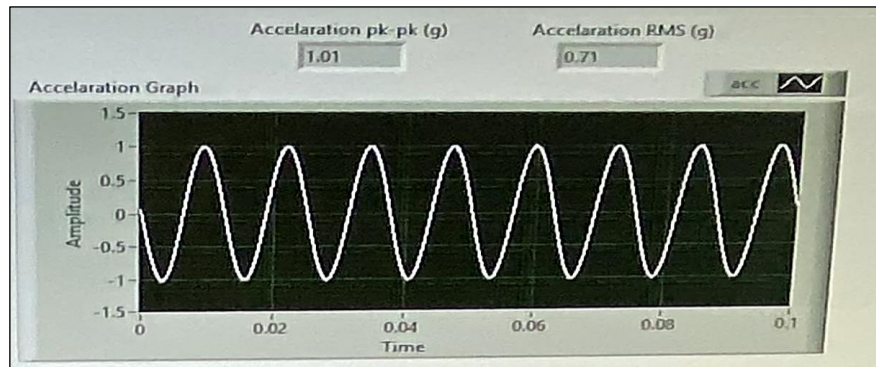


Figure 40: Input peak-peak acceleration of 1g used in the experiment

The mechanical damping was measured from the logarithmic decrement function resulted from applying a small force at the tip of the cantilever beam and plotting the response (Figure 41). The damping ratio was about 1.1% calculated using the following equations [161]:

$$\delta = \frac{1}{n} \left( \frac{x_1}{x_{n+1}} \right) \quad (101)$$

$$\zeta = \frac{\delta}{\sqrt{(2\pi)^2 + \delta^2}} \quad (102)$$

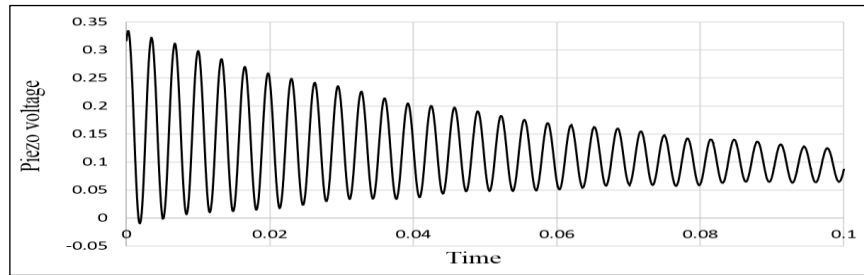


Figure 41: Logarithmic decrement function of rectangular piezoelectric cantilever

For frequency range 20-400 Hz, voltage FRF was measured for rectangular piezoelectric harvester as shown in Figure 42. Under input acceleration of 1g pk-pk, the resonance frequencies of the analytical and experimental measurements are 304.7 Hz and 304.4 Hz respectively. The voltage output for the experimental measurement is 12.25 V/g whereas for the analytical approximation is 12.92 V/g. The error between the experimental and analytical FRF voltage is about 5.5%. This error can be due to the losses that can happen during the experiment. The experiment was done in a normal lab where any vibration may affect the experimental measurements. However, vibration testing precautions were taken to insure minimizing the presence of any surrounding vibration noise.

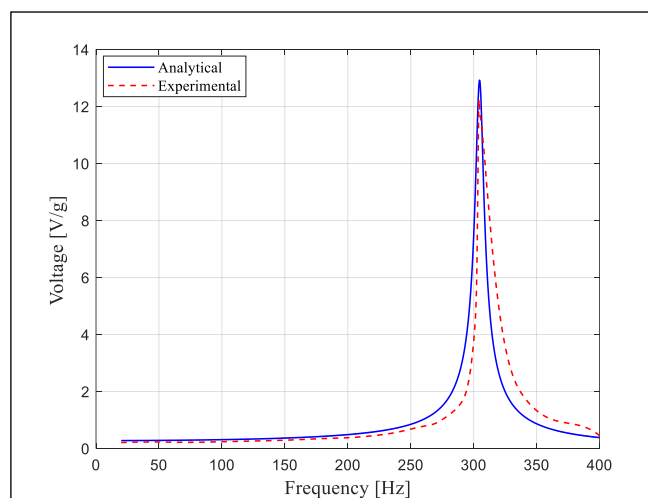


Figure 42: Voltage response to base acceleration of rectangular piezoelectric cantilever with damping ratio 0.011



Figure 43 presents the power FRF to base acceleration of rectangular piezoelectric cantilever. For damping ratio 0.011 under open circuit conditions, the harvested power from the experimental measurements is  $0.0097 \text{ mW/g}^2$  while for the analytical approximations the power is  $0.01085 \text{ mW/g}^2$ . The surface power densities for the experimental and analytical results are 26.61 and  $29.86 \text{ [(mW/g}^2)/\text{m}^2]$  respectively.

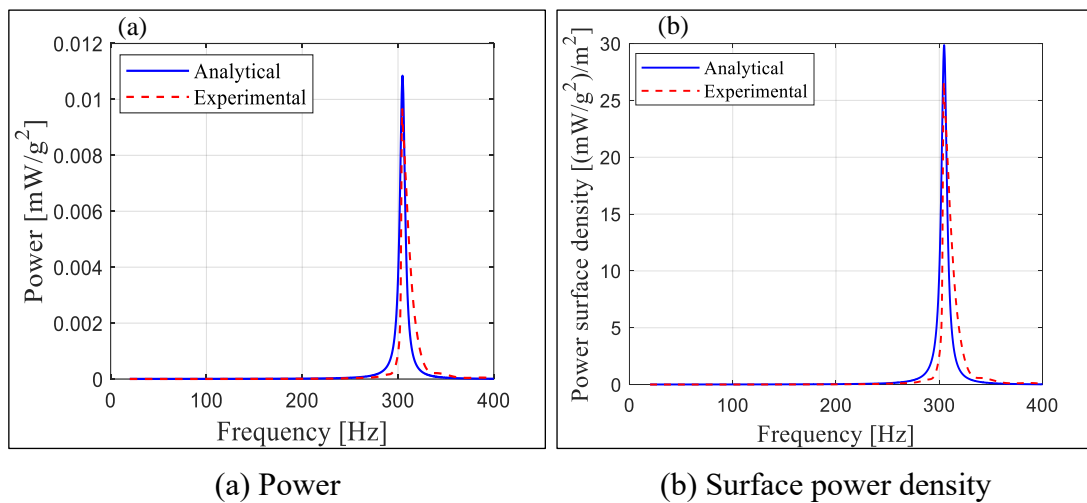


Figure 43: Analytical and experimental results of rectangular piezoelectric cantilever under open circuit conditions

Our initial goal was to continue with the experimental work for the optimally developed design validation. However, due to Covid-19 situation which led to the lockdown, the work has taken a new route where FEM was extensively used to validate the developed work. The integrated piezoelectric cantilever using FEM was used as an alternative to the experiment and presented in the next chapter.



## Chapter 5: Finite Element Analysis (FEA)

One of the goals of this thesis is to investigate the use of LPM in simulating the expected harvested power. As per the literature, the LPM showed limitations due to ignoring higher modes effect. As such correction factors were introduced for the rectangular and exponentially tapered cantilever beams using DPM [19], [127]. However, it is quite mathematically complicated to extend the DPM approach to find the correction factors for other taper beam shapes, e.g., linearly tapered beams. Alternatively, in this chapter, the FEM approach is used to model the linearly tapered piezoelectric beam. The first section of this chapter explains the mechanical modeling of a homogeneous piezoelectric cantilever using Femap with NX Nastran software. The second section describes an electromechanical model of the bimorph piezoelectric cantilever with a resistive load modeled using ANSYS workbench software with piezo & MEMS extension. The reliability of the developed FEM is verified in this chapter using three types of validations based on space domain, frequency domain and experimental work.

### 5.1 Mechanical modeling

The piezoelectric cantilever is modeled using Femap with NX Nastran software. The Average density, Young's Modulus of Elasticity (Equations (48)) are calculated and used in developing an equivalent homogeneous beam.

Average mass density equation is computed as:

$$\rho_{avg} = \frac{2\rho_p h_p + \rho_b h_b}{2h_p + h_b} \quad (103)$$

Figure 44 represents the FEM of linearly tapered piezoelectric cantilever subjected to a tip mass. The tip mass of the modeled beam is a point mass located at the last node of the beam. As shown in the figure representation, the model element is divided into 500 beams to give the highest possible accuracy where each beam has two nodes. Results from the FEM are based on Euler- Bernoulli beam theory.

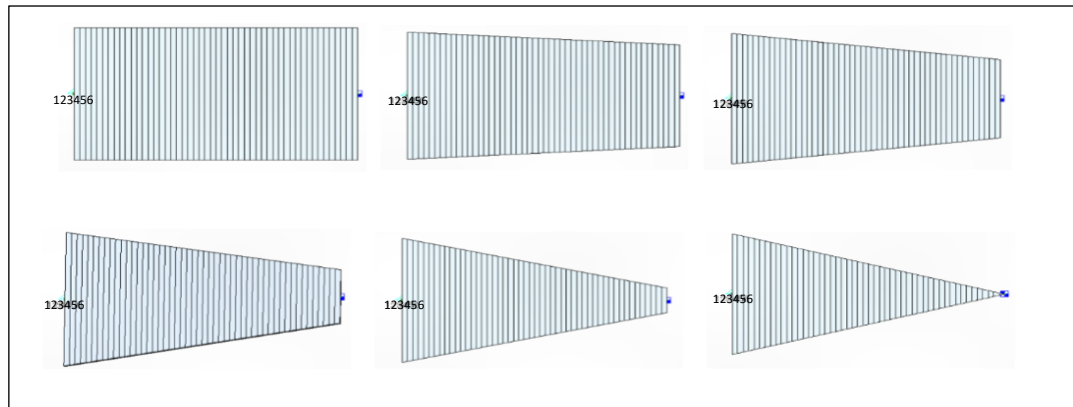


Figure 44: FEM of linearly tapered piezoelectric cantilever beam with tip mass (for taper ratios  $r = 1, 0.8, 0.6, 0.4, 0.2$  and  $0$ )

The correction factor of a linearly tapered piezoelectric harvester using FEM, is defined by:

$$CF = \frac{T_{rel}^{FEM}}{T_{rel}^{LPM}} \quad (104)$$

However, the used software provides only the absolute tip-displacement transmissibility function as a complex numeric data and function of frequency. In fact, the relative tip-displacement transmissibility function is related to the absolute tip-displacement transmissibility function. As per the provided definitions of the relative tip-displacement transmissibility function, the relative tip displacement can be expressed as:

$$z(t) = T_{rel}Y_0e^{j\omega t} \quad (105)$$

Where  $T_{rel}$  is the relative tip-displacement transmissibility function. Similarly, the absolute tip displacement can be expressed as:

$$y_m(t) = T_{abs}Y_0e^{j\omega t} \quad (106)$$

Where  $T_{abs}$  is the absolute tip-displacement transmissibility function. It should be noted here that  $T_{rel}$  and  $T_{abs}$  are both complex functions. As per the definition of the relative displacement,

$$z(t) = y_m(t) - y(t) \quad (107)$$

Using equation (105) and (106), and substitute in equation (107) results in:

$$T_{rel}Y_0e^{j\omega t} = T_{abs}Y_0e^{j\omega t} - Y_0e^{j\omega t} \quad (108)$$

Which is simplified as:

$$T_{rel} = T_{abs} - 1 \quad (109)$$

Hence, the magnitude of the  $T_{rel}$  can be evaluated from the complex numeric data of  $T_{abs}$  by:

$$|T_{rel}| = \sqrt{(\text{Re}(T_{abs}) - 1)^2 + (\text{Im}(T_{abs}))^2} \quad (110)$$

Where Re and Im denote the real and imaginary components of the variable in brackets, respectively. Equation (110) can be applied to the FEM as:

$$|T_{rel}^{FEM}| = \sqrt{(\text{Re}(T_{abs}^{FEM}) - 1)^2 + (\text{Im}(T_{abs}^{FEM}))^2} \quad (111)$$

The mechanical and geometrical specifications of the modeled piezoelectric harvester are taken from Inman [109] for model verification and evaluation. Table 8 and Table 9 present the specifications used in the simulations.

Table 8: Mechanical properties of piezoelectric cantilever beam used in simulation

Property	Piezoelectric (PZT-5A)	Substrate (Brass)
Density ( $kg/m^3$ )	7800	9000
Modulus of Elasticity ( $Gpa$ )	99	105
Poisson Ratio	-	0.3

Table 9: Geometric specifications of piezoelectric cantilever beam used in simulation

Property	Piezoelectric (PZT-5A)	Substrate (brass)
Length ( $mm$ )	50.8	50.8
Root width ( $mm$ )	31.8	31.8
Thickness ( $mm$ )	0.26 (each)	0.14

## 5.2 Electromechanical modeling

An electromechanical model of a bimorph piezoelectric cantilever beam is developed using ANSYS workbench software with the PIEZO & MEMS extension. The extension provides the electromechanical coupling properties of the piezoelectric material. PIEZO & MEMS extension uses SOLID 226 which is a 3D 20 nodes brick used for coupled fields. Figure 45 presents the electromechanical model of a bimorph piezoelectric harvester with the boundary conditions.

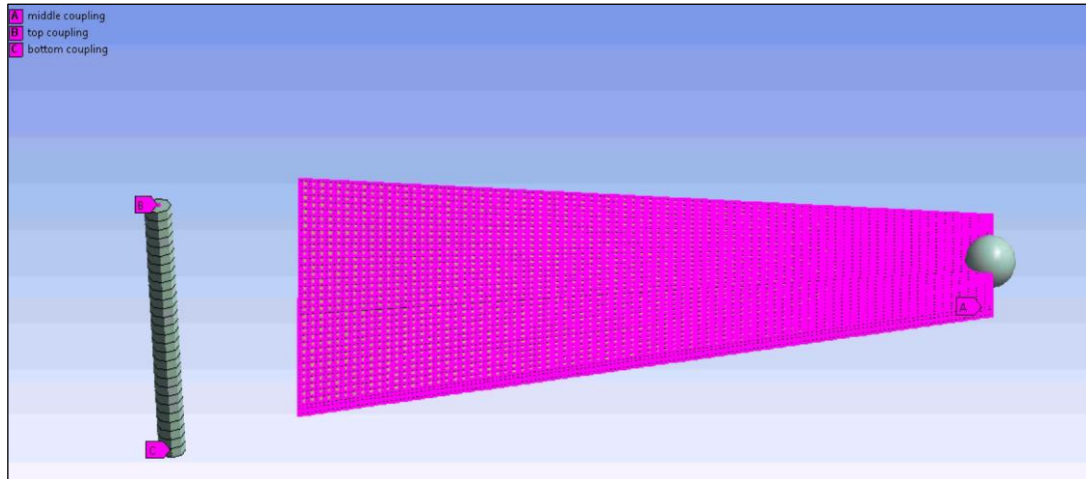


Figure 45: Electromechanical coupling of a tapered piezoelectric cantilever harvester FEM ( $r = 0.4$ )

The following steps show the modeling process of a piezoelectric harvester attached to a load resistance circuit.

- Step 1: Design the piezoelectric harvester
  - Space Claim software is used to model the piezoelectric harvester. The harvester consists of piezoelectric cantilever and a resistor. The piezoelectric cantilever is a substrate sandwiched between two piezoelectric patches. The resistor is designed as a two nodes beam with a circular cross section.
  - The geometrical specifications used are from Table 9.
- Step 2: Assign the material properties
  - The material properties of piezoelectric patches, substrate and the resistive beam are listed in Table 10.
  - The piezoelectric patches are assigned as anisotropic material (SOLID 226)
  - The substrate is assigned as a brass material (SOLID 188).

- The resistive beam is assigned as a material is Polystyrene foam rigid.

Table 10: Material properties of piezoelectric harvester in FEM

Material	Property	Magnitude
Brass (substrate)	Density ( $kg/m^3$ )	9000
Polystyrene foam (resistive load circuit)	Density ( $kg/m^3$ )	20
Piezoelectric PZT-5A	Density ( $kg/m^3$ )	7800
	$C_{11}^E$ (Pa)	$1.2035 \times 10^{11}$
	$C_{12}^E$ (Pa)	$7.5179 \times 10^{10}$
	$C_{13}^E$ (Pa)	$7.509 \times 10^{10}$
	$C_{33}^E$ (Pa)	$1.1087 \times 10^{11}$
	$C_{55}^E$ (Pa)	$2.1053 \times 10^{10}$
	$C_{66}^E$ (Pa)	$2.1053 \times 10^{10}$

Note:  $C_{11}^E = C_{22}^E$ ,  $C_{13}^E = C_{23}^E$ ,  $C_{44}^E = C_{55}^E$ .

- Step 3: Create the model in ANSYS workbench
  - Geometry:
    - Two parts are assigned. One is for the resistive beam and the other is for the cantilever beam.
    - Under the resistor/ beam, an APDL command is embedded to assign a resistive property to the beam.
      - The APDL command for assigning a resistor is:

ET,10, CIRCU94,0      Set up the resistor for the assigned geometry

R,1,470000              Set up the magnitude of the resistance

TYPE,10                 Set the type of the element

E,1,2

Create the resistor between the upper node 1 and the lower node 2 of the beam

- Connections
  - The contacts in the cantilever beam between the upper piezo patch, substrate and the lower piezo patch are merged.
- Mesh
  - The meshing is a quadratic mesh with a resolution of 7.

Figure 46 shows the meshing of a tapered piezoelectric beam.

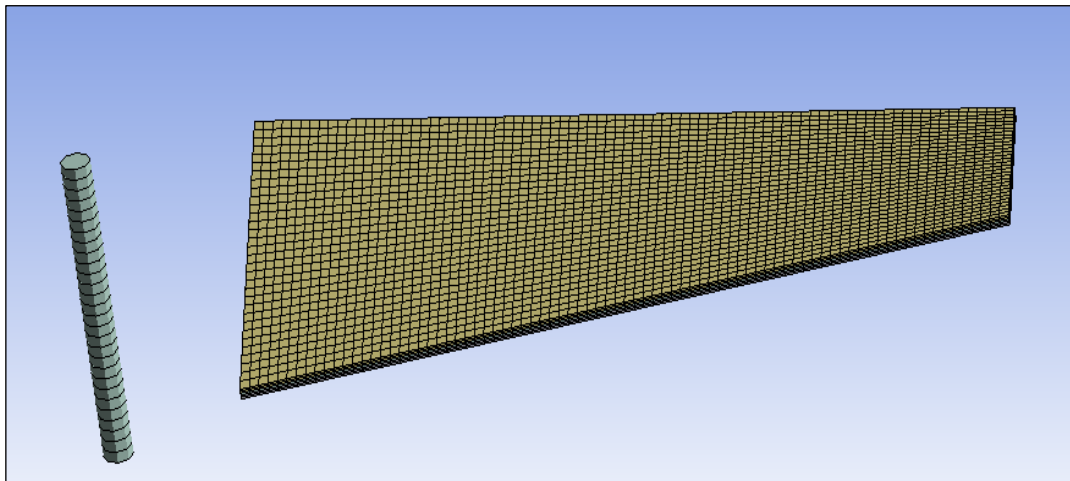


Figure 46: Meshing of tapered piezoelectric beam in ANSYS ( $r = 0.4$ )

- Step 4: Find the mode shapes
  - Executing the model analysis command generates the mode shapes of the piezoelectric harvester.
  - The 1<sup>st</sup> mode shape is the one to take into consideration for the harmonic analysis.

Figure 47 shows the mode shapes of a tapered piezoelectric harvester ( $r = 0.4$ ).

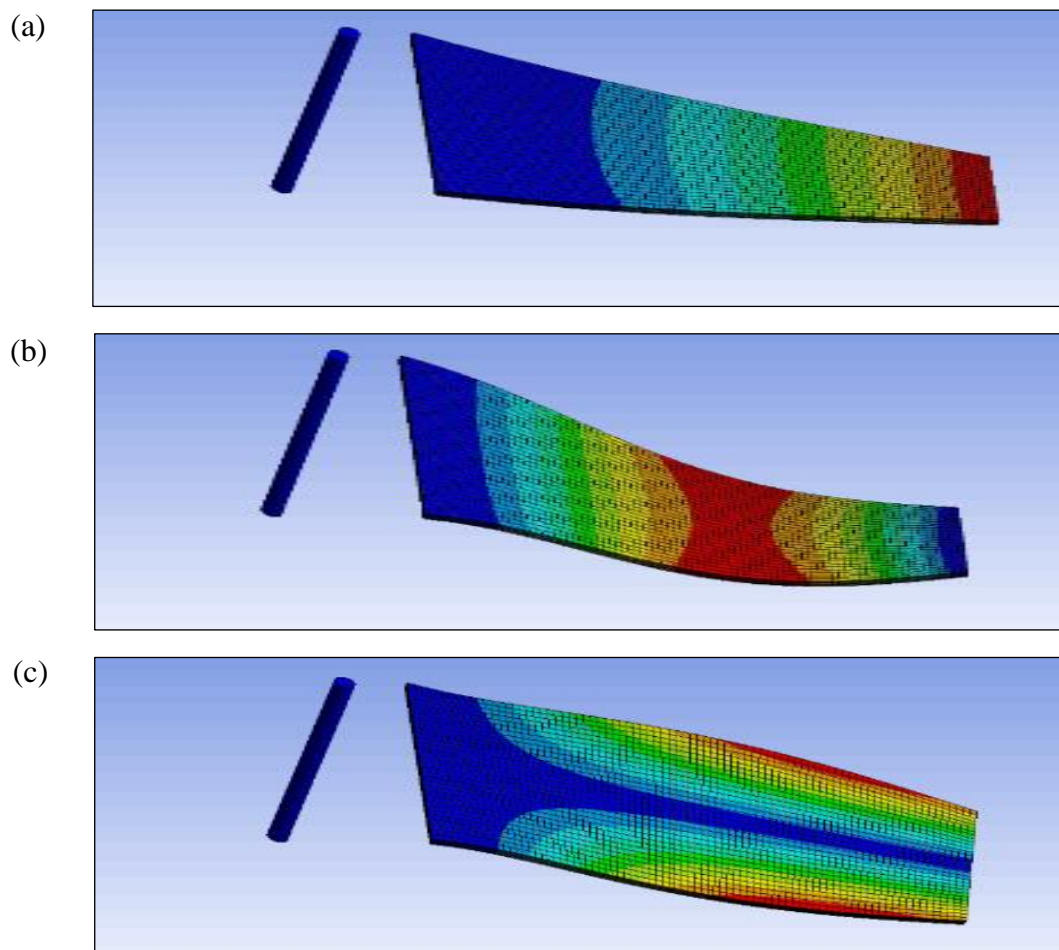


Figure 47: Modes of a tapered piezoelectric cantilever harvester using FE ( $r = 0.4$ )  
 (a) 1<sup>st</sup> mode shape (b) 2<sup>nd</sup> mode shape (c) 3<sup>rd</sup> mode shape

- Step 5: Conduct harmonic analysis
  - In the harmonic analysis, a sinusoidal load is applied to the piezoelectric harvester base which induces a strain in the piezoelectric patches. This strain generates voltage output for a set of frequency range. The harmonic analysis is developed as per the following:
    1. Assign mechanical BC's
      - Choose fixed displacement at the base of the piezoelectric cantilever [0,0,0].



- Choose fixed displacement at the bottom vortex of the resistor [0, 0, 0].
  - Choose fixed rotation at the bottom vortex of the resistor [fixed, fixed, fixed].
2. Assign an input excitation
- Acceleration input is applied to the piezoelectric cantilever [0, 0, 9.81].
3. Assign piezoelectric bodies
- Choose a simplified piezoelectric body for the top and bottom patches of the cantilever.
  - Set the polarization in the z-direction.

Table 11 lists the electromechanical properties of a PZT-5A material used in the FEM.

Table 11: Electromechanical properties used in ANSYS for piezoelectric materials

Property	Parameter	Magnitude
Piezoelectric stress	$e_{31}$	-5.4
Piezoelectric stress	$e_{33}$	15.8
Piezoelectric stress	$e_{15}$	12.3
Permittivity	$\frac{\epsilon_{11}}{\epsilon_0}$	916
Permittivity	$\frac{\epsilon_{33}}{\epsilon_0}$	830

4. Assign electrical BC's
- Assign voltage coupling in the middle faces
  - Assign ground voltage at the bottom vortex of the resistor
  - Assign voltage coupling for the top and bottom faces of the piezoelectric patches

5. Solve the harmonic analysis model
  - Set the frequency range from 30- 60 Hz
  - Set the desired outcomes like:
    - FRF of voltage output

### 5.3 Validation of the FEM

The developed FEM is used as a reference instead of the DPM. Therefore, validation of the FEM is required. Three types of validations for the beam dynamics and electromechanical characteristics are performed in this section. The first validation is a space domain validation where the FEM is verified using the beam deflection of a piezoelectric cantilever. The second type uses the relative tip displacement transmissibility function based on frequency domain analysis to validate the FEM. Finally, the integrated piezoelectric cantilever in FEM is validated with DPM and experimental results taken from the literature [19].

#### 5.3.1 Validation using beam deflection

The FEA's validation is accomplished by comparing the FEM results with the DPM taken from the literature. Two DPM are used in the validation process. The first model is a rectangular piezoelectric beam with tip-mass developed by [19], [109]. The second model is a tapered piezoelectric beam with no tip-mass developed by [162], [163]. It is essential to mention here that the tip mass in this study is considered a point mass.

Figure 48 presents the normalized deflection of FEM and DPM for rectangular piezoelectric beam subjected to different tip mass ratios of  $a = 0, 0.5, 2$  and  $5$ . Tip mass ratio is defined as the tip mass to beam mass ( $a = M_t/mL$ ). The FEM and the

DPM show an excellent agreement with a very small percentage error of less than 0.003% for all chosen tip mass ratios.

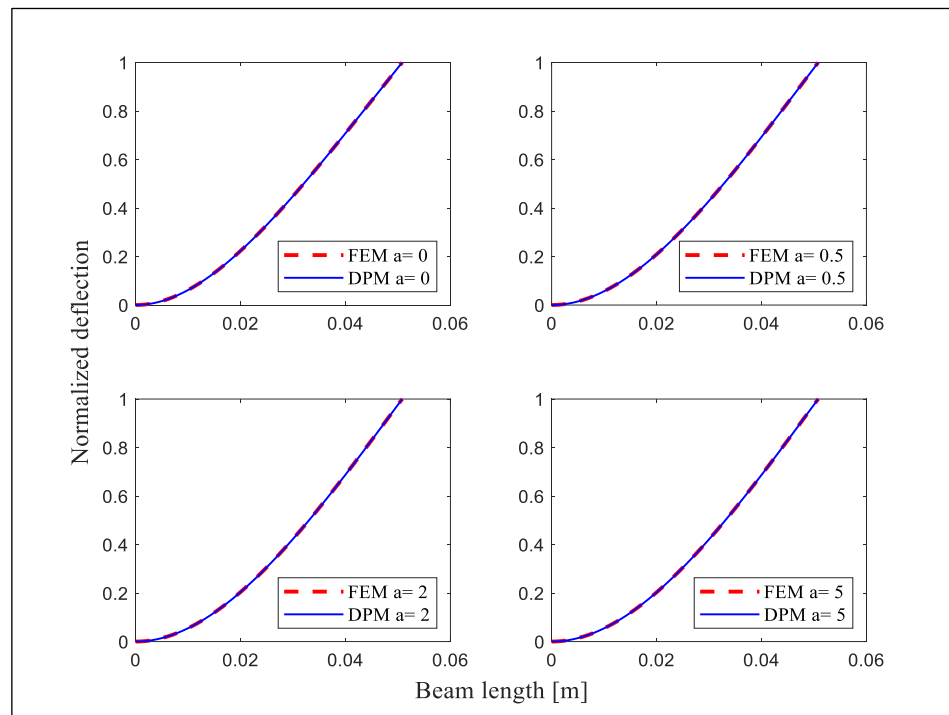


Figure 48: Normalized deflection of EFM and DPM for rectangular piezoelectric cantilever beam with different tip mass ratios of  $a = 0, 0.5, 2$  and  $5$

Figure 49 shows the normalized deflection of the FEM and DPM for tapered piezoelectric beam with taper ratios of  $r = 1, 0.8, 0.6, 0.4, 0.2$  and  $0$ . In this case, the cantilever beam is not subjected to any tip mass. Recall that the taper ratio is defined as  $r = b_t/b_0$ . Results show that for taper ratios of  $1, 0.8$  and  $0.6$ , the normalized deflections of the FEM and DPM are in a very good match with an error of less than 0.2%. For lower taper ratios of  $0.4, 0.2$  and  $0$ , the chart shows a good match, but the error between the FEM and the DPM increases from 0.2% to reach up to 3% for a taper ratio of  $r = 0$ . This percentage error results from the approximation in the analytical solution of the DPM. However, for an overall engineering approach, the error is considered acceptable; thus, the model validation is assumed to be correct. From the

results shown, the validation of FEA is confirmed using the normalized deflection comparison between the FEM and DPM from the literature.

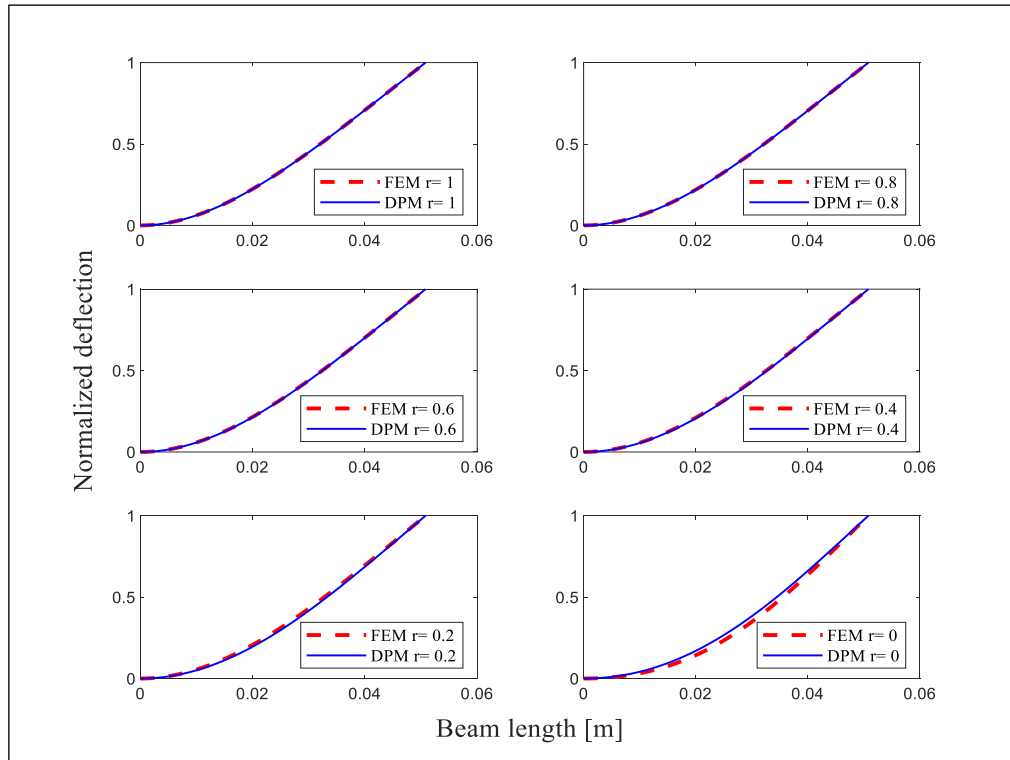


Figure 49: Normalized deflection of FEM and DPM for different tapered piezoelectric cantilever beams of  $r = 1, 0.8, 0.6, 0.4, 0.2$  and  $0$  with no tip mass

### 5.3.2 Validation using beam relative transmissibility function

Validation of the developed FEM using the relative transmissibility function is accomplished utilizing the rectangular piezoelectric analytical model from the literature. The relative tip displacement transmissibility function is defined as the ratio of the relative tip displacement to the base displacement. The reference DPM is a model of a transverse rectangular piezoelectric with a tip mass developed by Inman [109]. The DPM and FEM responses are compared with no tip mass. Figure 50 presents the comparison of the relative tip displacement transmissibility functions for the DPM and the FEM developed in this study using three different values of the

damping ratio. The results showed an excellent agreement between the DPM and the developed FEM for all the damping ratios.

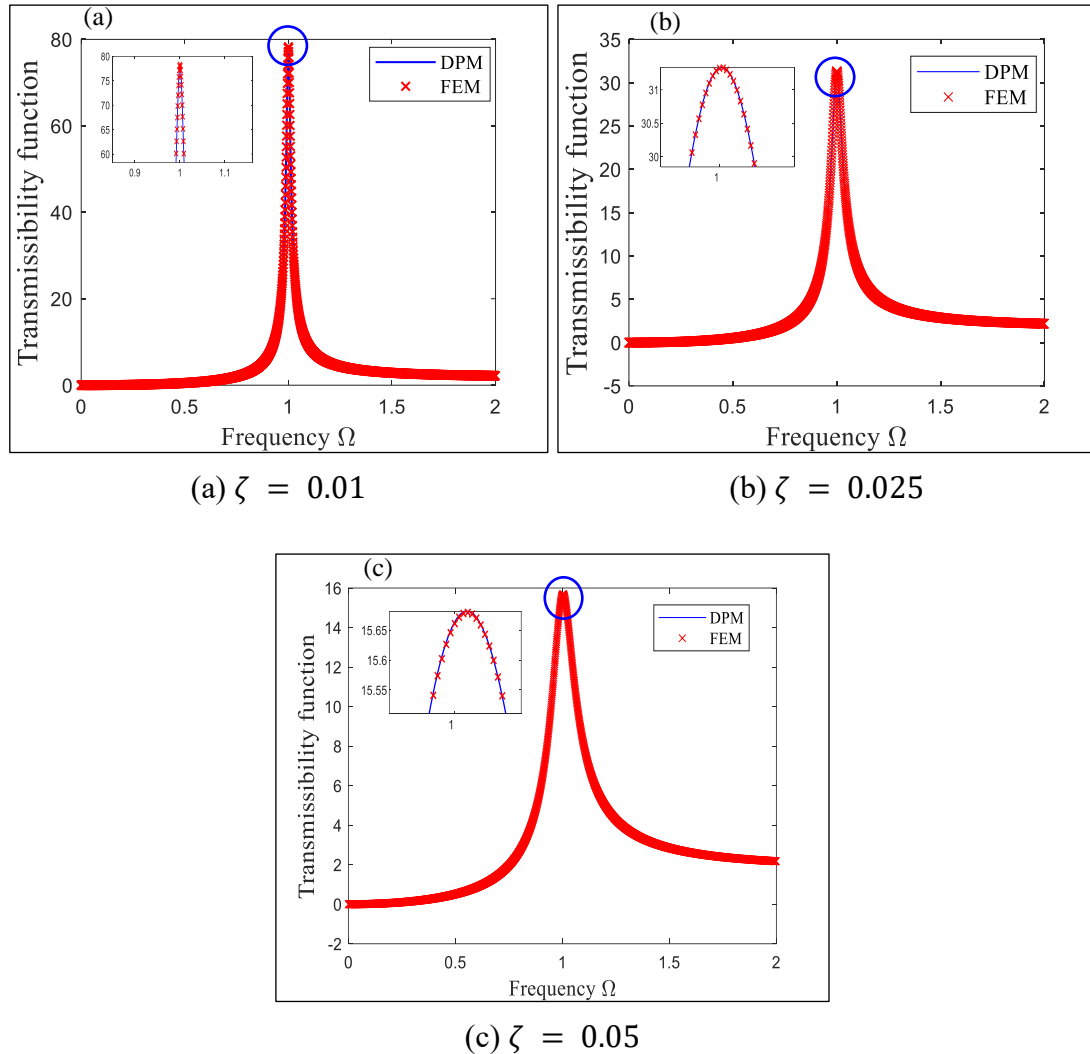


Figure 50: Relative transmissibility functions of DPM and FEM for transverse rectangular piezoelectric cantilever beam with no tip mass

### 5.3.3 Validation using integrated piezoelectric cantilever beam in FEM

The FEM is developed using ANSYS workbench with PIEZO and MEMS extension. All the modeling details are mentioned in Section 5.2. Table 10 and Table 11 list all the properties used in the FEM. The FEM verification is accomplished by comparing the DPM and experimental results taken from the literature [19] with the

developed electromechanical FEM, as shown in Figure 51. The comparison is based on a rectangular piezoelectric beam with load resistance of 33 k $\Omega$ . The resonance frequencies of the FEM, the DPM and the referenced experimental result are 46.5 Hz, 46 Hz and 46 Hz, respectively. The peak value of tip velocity for the FEM, the DPM and the reference experimental result are 0.42, 0.41 and 0.43 [(m/s)/g]. The peak voltage output for the FEM, the DPM and the experimental result are 28.54, 28.75 and 28.25 [V/g]. The error between the DPM and the FEM of the tip velocity and voltage is about 1%, which verifies the use of the FEM.

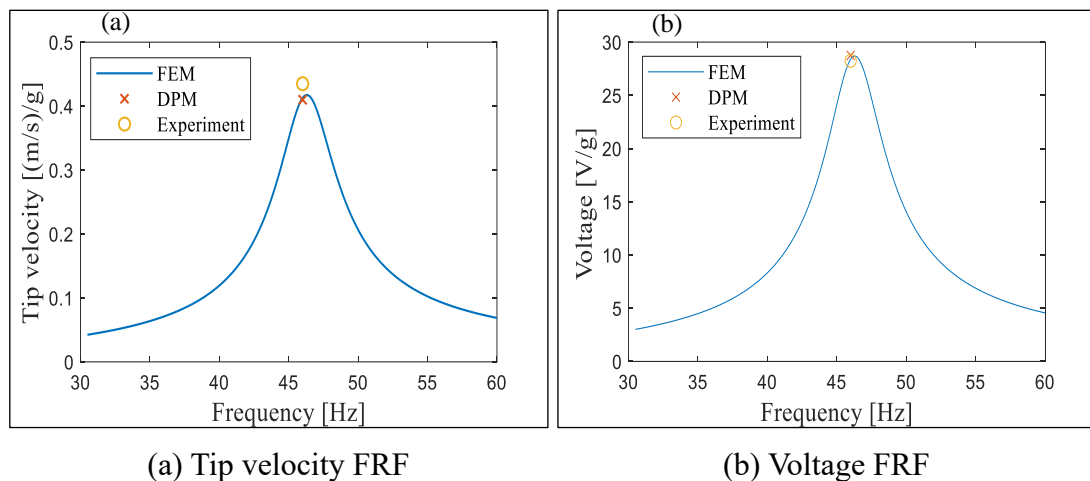


Figure 51: Comparison between the developed FEM and the peak results of DPM and experimental measurements taken from [19] for  $R = 33 \text{ k}\Omega$

Using another load resistance of 470 k $\Omega$ , Figure 52 shows that the frequencies of the FEM, the DPM and the reference experimental result are 48.5 Hz, 48.4 Hz and 48.4 Hz, respectively. The peak value of tip velocity for the FEM, the DPM and the reference experimental results are 0.51, 0.52 and 0.54 [(m/s)/g]. The voltage output for the FEM, the DPM and the reference experiment result are 96.3, 96 and 84 [V/g]. The 0.3% error difference between the FEM and the DPM is quite a small error and hence validates the use of the FEM in this study.

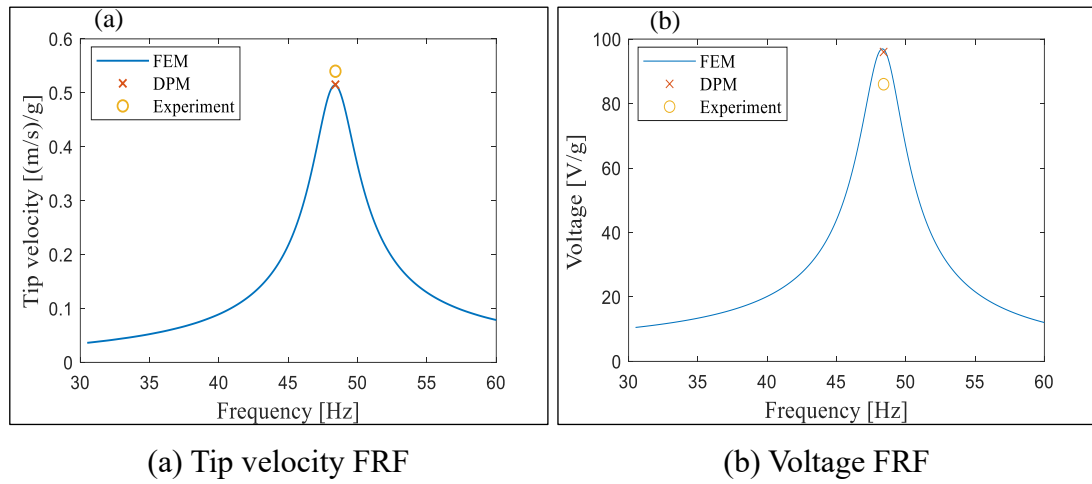


Figure 52: Comparison between the developed FEM and the peak results of DPM and experimental measurements taken from [19] for  $R = 470 \text{ k}\Omega$

## **Chapter 6: Design Optimization and Modeling of a Piezoelectric Harvester; Results and Discussions**

This chapter presents a new approach towards an optimally designed piezoelectric cantilever beam that can maximize the produced power for a given amount of a piezoelectric material. The developed LPM of Chapter 3 is used in reaching the optimal shape through a derived power factor parameter. In order to verify the effectiveness of the developed optimal design, a comparison of surface power density for different configurations is studied using the integrated piezoelectric cantilever in FEM. One of the objectives of the thesis is to scrutinize the use of the LPM in analyzing the power output of different tapered piezoelectric harvester configurations. To fulfill this goal, the LPM accuracy is first investigated. Then, the correction factor is developed to enhance the accuracy of the LPM. Afterward, the corrected LPM (C-LPM) is compared to the developed FEM for different parameters of different tapered piezoelectric harvesters, including the optimal design. Furthermore, a parametric study is conducted about the effect of the resistive load, tip mass and the piezoelectric material on the optimally shaped piezoelectric cantilever. Finally, the Chapter ends with a practical example of the optimal piezoelectric harvester for given inputs where all guidelines and limitations are discussed.

### **6.1 The development of an optimal piezoelectric harvester design**

This section presents a comprehensive level analysis to obtain an optimal configuration of a piezoelectric harvester system. The analysis involves design, modeling and optimization studies. The effect of different geometries on the piezoelectric cantilever's power output is investigated. The optimum design of a piezoelectric cantilever beam with tip mass is first developed based on the Power



Factor dimensionless parameter that was derived in Chapter 3. The behavior of stress distribution along the length of different piezoelectric shapes is also studied. A FEM verification is presented to show the power output per piezo material area of an optimal design in comparison to the other shapes.

### **6.1.1 Design optimization**

The design optimization of a piezoelectric cantilever harvester is conducted using the developed dimensionless Power Factor parameter. Furthermore, the normalized stress of different tapered piezoelectric cantilevers is studied to understand the stress distribution of various piezoelectric configurations.

#### **6.1.1.1 Power factor**

The fundamental tool used for design optimization is the Power Factor parameter (PF), which was derived in the mathematical modeling chapter. It is a dimensionless parameter that evaluates the impact of different geometrical parameters like taper ratio, thickness ratio and aspect ratio on the performance of the piezoelectric cantilever harvester. Where the aspect ratio is defined as the ratio of the cantilever length to width at the base ( $a_r = L/b_0$ ). The thickness ratio is the ratio of the piezoelectric thickness to the substrate thickness ( $t_p = h_p/h_b$ ). The taper ratio is the ratio of width at the tip to the width at the base of cantilever beam ( $r = b_l/b_0$ ). As a practical example, Table 12 lists all the data used in the analytical analysis of designing a bimorph piezoelectric cantilever beam.

Table 12: Material and geometrical parameters of a piezoelectric cantilever harvester taken from [19]

Item	Symbol	Unit	Value
Piezoelectric density	$\rho_p$	$kg/m^3$	7800
Substrate density	$\rho_b$	$kg/m^3$	9000
Piezoelectric stiffness	$E_p$	$Gpa$	66
Substrate stiffness	$E_b$	$Gpa$	105
Strain constant	$d_{31}$	$C/m$	$-190 \times 10^{-12}$
Stress constant	$e_{31}$	$C/m$	-11.5
Vacuum permittivity	$\epsilon_0$	$F/m$	$-8.854 \times 10^{-12}$
Absolute permittivity	$\epsilon_{33}^S$	$F/m$	$1500\epsilon_0$
Beam length	$L$	$mm$	50.8
Beam width	$b$	$mm$	31.8
Piezoelectric thickness	$h_p$	$mm$	0.26
Substrate thickness	$h_b$	$mm$	0.14
Damping ratio	$\zeta$	-	0.027
Tip mass	$M_t$	$kg$	0.012

Figure 53 shows the effect of taper ratio and aspect ratio on the power factor (PF) parameter. It is shown from the 3D plot that the PF increases with the decrease of the taper ratio. Note that taper ratios  $r > 1$  is for reversed tapered piezoelectric beams where the width at the tip is larger than the width at the base. For taper ratios ( $r = 2$ ) the PF is 4.105 whereas for taper ratio ( $r = 0.05$ ) the PF is 6.67 respectively. However, the PF exhibits a constant magnitude when subjected to different aspect ratios. This indicates that the aspect ratio has no effect on the PF.

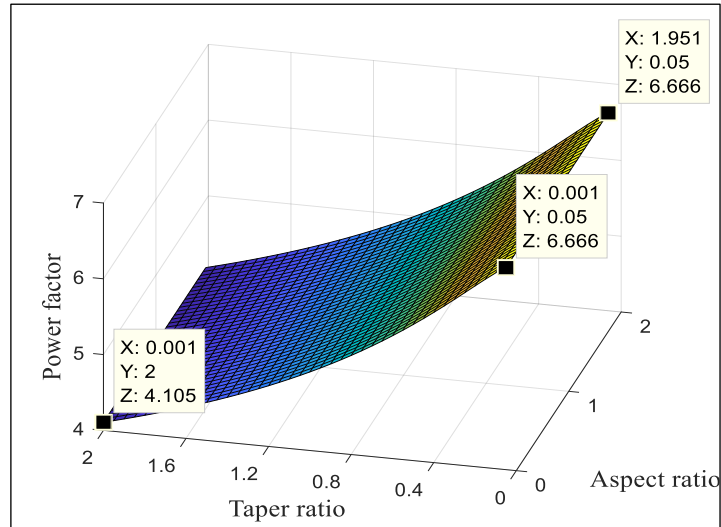


Figure 53: 3D plot of the power factor (PF) for different taper ratios and aspect ratios of a bimorph piezoelectric beam

So far, the PF is computed for linearly tapered beams and the highest PF is for  $r = 0$ , i.e., the beam width at the tip is zero. Now, nonlinear taper beams will be examined but with the width at the tip set to zero. This can be accomplished by just introducing a middle section that divides the beam into a trapezoidal beam joined with a triangular beam, as illustrated in Figure 54 below. The length of the piezoelectric cantilever is indicated by  $l$  whereas  $l_m$  is the length from the base of the cantilever to the middle section.  $b_0$  is the width of the piezoelectric cantilever at the base and  $b_m$  is the width of the middle section.

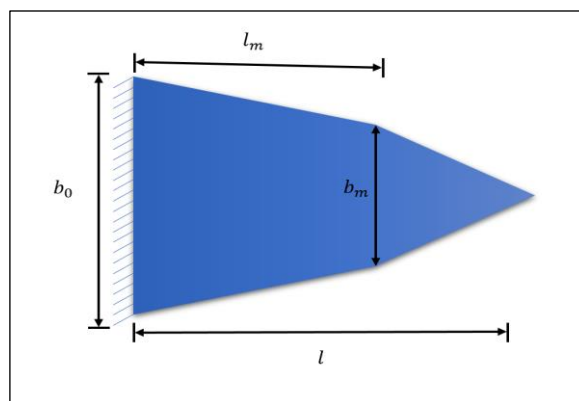


Figure 54: Schematic of a piezoelectric cantilever beam with a middle section

Figure 55 presents the power factor of the nonlinear tapered beam of Figure 54. The 3D plot indicates that the highest power factor is always for the shape that forms a linear tapered beam. It is important to know that although taper ratio  $r = 0$  is an ideal design that gives the maximum power factor, it is an unpractical design when adding a tip mass at the end of the piezoelectric cantilever. Thus, a minimum beam width of  $0.2b_0$  is considered to be a reliable design that can achieve a high-power factor and handle the placement of a tip mass. However, the taper ratio should be set at  $r = 0$  considering the total cantilever beam length  $l$ . Based on the previous conclusion, the chosen optimal middle section point is given by  $l_m = 0.8 l$  and  $b_m = 0.2 b_0$ .

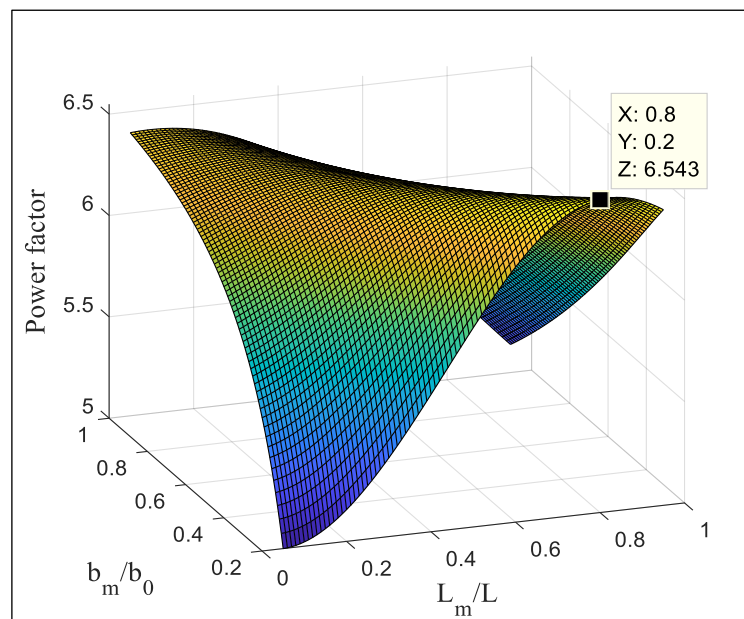


Figure 55: 3D plot of power factor for different middle point positions of a bimorph piezoelectric beam

Figure 56 shows the effect of the thickness ratio and taper ratio on the power factor. As it is shown in the 3D plot, the highest power factor is at a given thickness ratio of  $t_p = 0.7$ .

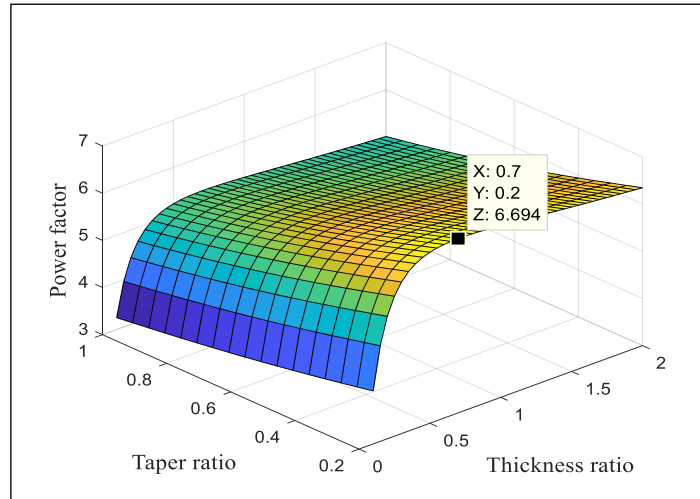
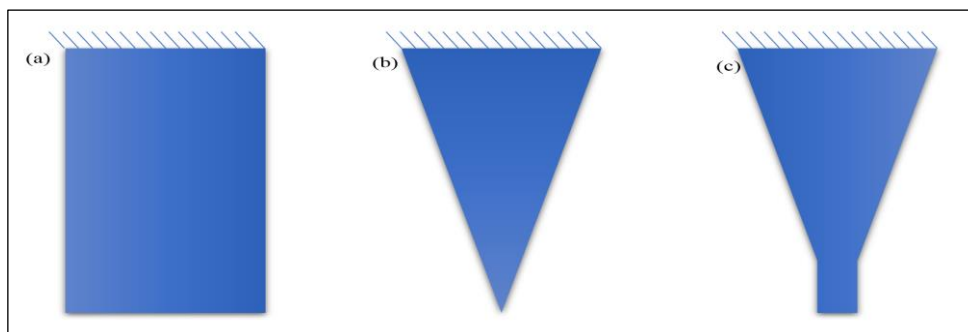


Figure 56: 3D plot of power factor for different thickness ratios and taper ratios of a bimorph piezoelectric beam

From the above-studied parameters, the optimized design is given at a taper ratio of ( $r = 0$ ) with a middle section of  $l_m = 0.8 l$  and  $b_m = 0.2 b_0$  and a thickness ratio of ( $t_p = 0.7$ ). Figure 57 shows a schematic of the optimal design configuration in comparison to other known designs like the rectangular shape ( $r = 1$ ) and the triangular shape ( $r = 0$ ). It is worth mentioning that the developed power factor parameter may not be affected by a certain parameter like aspect ratio. However, it doesn't eliminate the effect of aspect ratio on the power output of the piezoelectric harvester.



(a) Rectangular shape      (b) Triangular shape      (c) Optimal practical shape.

Figure 57: Schematic of different configurations of piezoelectric cantilevers harvesters

### 6.1.1.2 Normalized stress

Another critical parameter that affects the performance of piezoelectric harvester is the stress distribution. Previous studies with analytical, numerical and experimental evidence showed that the more uniformly distributed the stress along the cantilever beam, the higher the power density is harvested [115], [119], [121], [164]. To understand the effect of stress distribution, the normalized stress of different configurations was studied. The normalized stress is defined as:

$$\sigma_n = \frac{\sigma_p(x)}{\sigma_{tip}} \quad (112)$$

Where  $\sigma_p(x)$  is the stress of piezo element at x position defined in equation (25) and  $\sigma_{tip}$  is the stress at the tip of the piezoelectric cantilever beam.

Figure 58 shows the normalized stress of different tapered piezoelectric cantilever beams of ( $r = 1, 0.8, 0.6, 0.4$  and  $0.2$ ) and the optimal design. Taper ratio 1 gives the lowest normalized stress distribution. As the taper ratio decreases, the stress is becoming more distributed evenly along the beam length. The developed optimal design exhibits the most uniform stress distribution in comparison to the rest of the piezoelectric configurations which confirms the studies discussed in the literature.

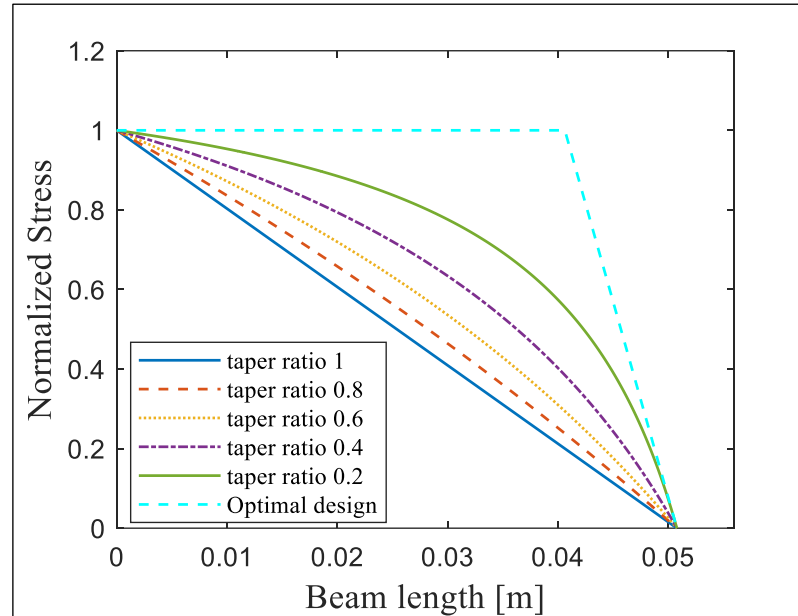


Figure 58: Normalized stress of different taper ratios and optimal design of the piezoelectric cantilever beam

### 6.1.2 FEM verification of the optimal piezoelectric harvester design

In order to verify the optimized piezoelectric cantilever configuration, FEM is used as mimicking tool of the DPM for a piezoelectric harvester. An electromechanical model is developed using ANSYS workbench software for different piezoelectric shapes (Section 5.2). Figure 59 presents the surface power density for different geometrical designs of piezoelectric cantilever harvesters with load resistance of 470 k $\Omega$  using FEM. It is proven from the figure that as the taper ratio decreases from ( $r = 1$ ) to ( $r = 0.2$ ), the surface power density increases significantly. The optimum design gives the maximum surface power density in comparison to the tapered piezoelectric geometries. The best surface power density for a tapered piezoelectric ( $r = 0.2$ ) is  $1.22 \times 10^4$  [(mW/g<sup>2</sup>)/m<sup>2</sup>] whereas the optimum design's surface power density is  $1.46 \times 10^4$  [(mW/g<sup>2</sup>)/m<sup>2</sup>]. Furthermore, the resonance frequency decreases with the decrease of the taper ratios. However, the optimum design has the lowest resonance

frequency of 41.5 Hz. The optimal design shows a noticeable improvement in the harvested power with a small resonance frequency which can be a great potential for different applications.

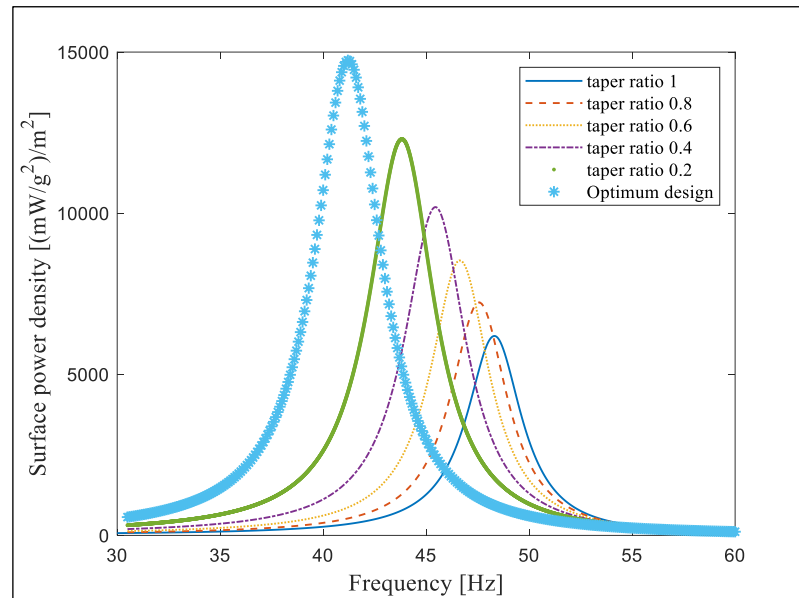


Figure 59: Surface power density for different geometrical designs of piezoelectric cantilever harvester with load resistance of 470 k $\Omega$  using FEM

## 6.2 The accuracy of modeling tapered piezoelectric harvester using LPM

The developed optimal design in Section 6.1 was optimized based on the Power Factor (PF) parameter which is derived from LPM. Thus, modeling the optimal design using the LPM is a significant part of this thesis that will be investigated in this section. Previous studies in Chapter 2 discussed the limitations of the LPM in predicting an accurate vibrational behavior of the piezoelectric cantilever. Thus, the accuracy of the LPM for rectangular piezoelectric cantilever harvesters was discussed in the literature as well as the effect of the tip mass on the LPM precision. However, there has been little discussion on the accuracy of different geometries other than the rectangular piezoelectric cantilever beams. Therefore, this section aims to investigate the accuracy of the LPM for linearly tapered piezoelectric cantilever harvesters as well as the



optimal design developed in the previous section. Furthermore, this study analyzes the effect of tip mass ratio on the LPM approximations. The validated FEM of the linearly tapered piezoelectric cantilever is used in this study as a baseline to investigate the accuracy of the LPM for different piezoelectric cantilever shapes.

In order to understand the accuracy of the LPM of a tapered piezoelectric cantilever, the normalized deflection of the FEM of a tapered beam that accompanied with tip mass is used as a reference. In this study, the normalized deflection of the LPM of the tapered with a tip mass that was developed in Chapter 3 is compared to the normalized deflection of the equivalent FEM beam. The percentage error of the normalized deflection between the LPM and FEM is used as a comparison parameter in this study. A low value of the normalized deflection error indicates that LPM can give a good estimation of the vibration response close to the DPM which is here represented by the FEM. The comparison is conducted for a number of cases of different taper ratios and optimal design to examine the effect of the tip mass on the deflection error.

### **6.2.1 The accuracy of the LPM for linearly tapered piezoelectric cantilever**

Figure 60 shows a comparison between the normalized deflections of the FEM and the LPM for different tapered piezoelectric cantilever of  $r = 1, 0.8, 0.6, 0.4, 0.2$  and  $0$ . Two cases are studied for each tapered piezoelectric cantilever. The first case is the comparison between the FEM and the LPM in the absence of the tip mass. The second case compares the FEM and the LPM with a tip mass ratio of  $a = 2$ . The results show that in the absence of the tip mass, a high dispersion in the normalized deflection between the LPM and FEM occurs. On the other hand, when the piezoelectric cantilever has a tip mass ratio 2, the normalized

deflections of the LPM and the FEM are in an excellent match. Furthermore, the graphs indicate that the gap between the normalized deflection of the LPM and the FEM for no tip mass increases when decreasing the piezoelectric cantilever's taper ratio. This gap represents the deflection percentage error between the two investigated models.

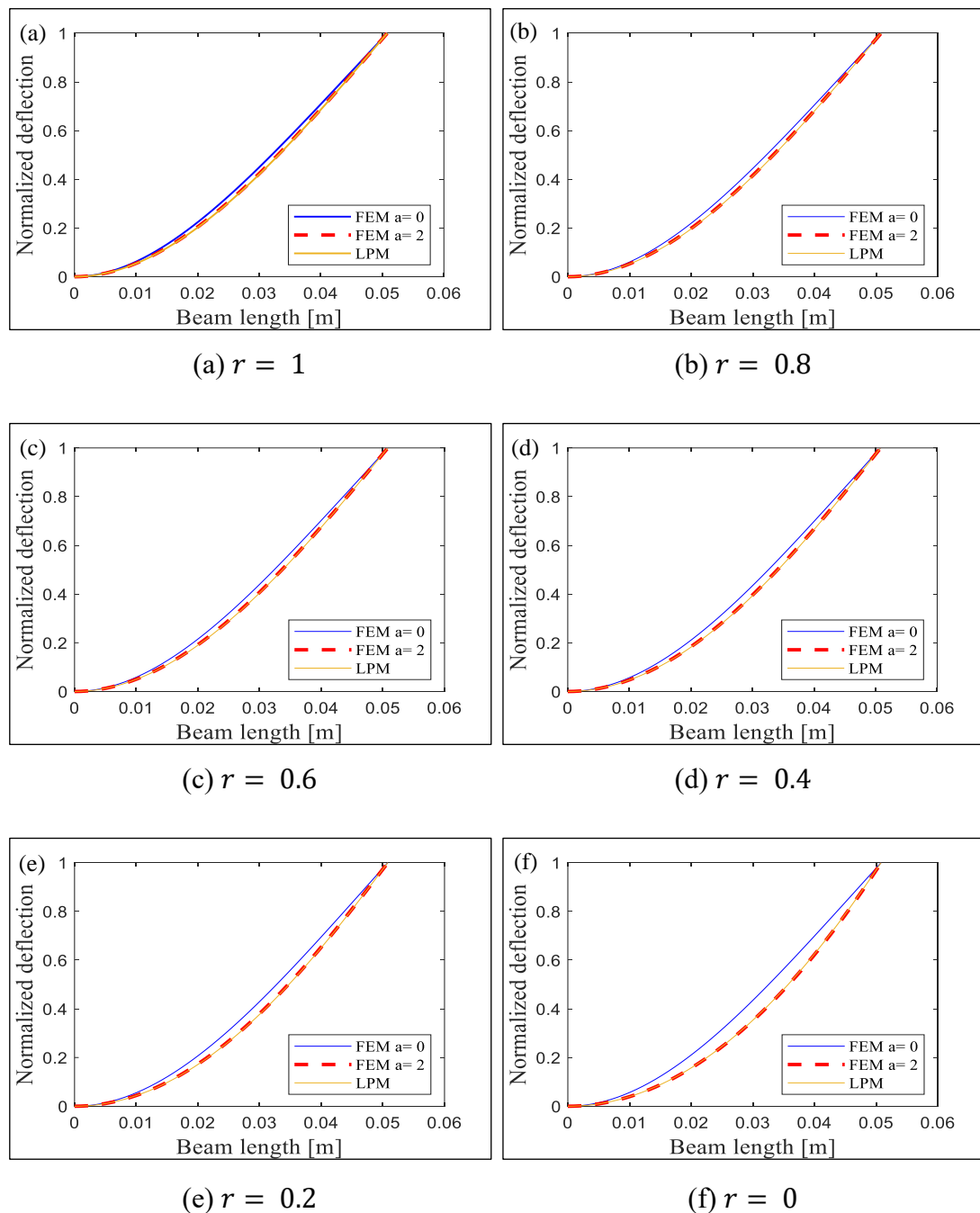


Figure 60: Comparison between the normalized deflection of the FEM and the LPM for different tapered piezoelectric cantilevers

Figure 61 presents the percentage error of the normalized deflection along the beam length for a tapered piezoelectric cantilever beam with a zero taper ratio (triangular beam) and no tip mass. Since percentage error is obtained after normalizing the deflection of both models (the FEM and the LPM), the error should be zero at the fixed end and also at the beam tip. The maximum error is located at about 2/3 of the beam length and with a value of about 9%. The maximum value of the normalized deflection percentage error is considered as the key parameter in quantifying the accuracy of the LPM.

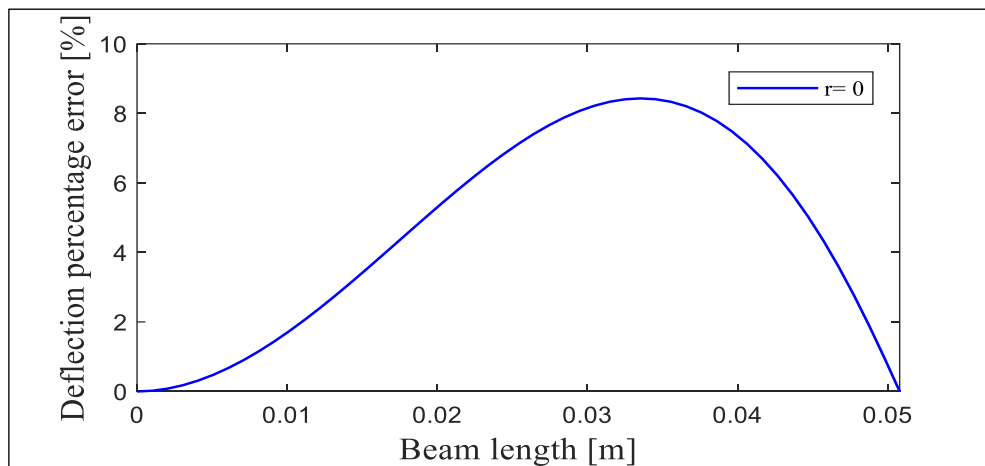


Figure 61: Percentage error of the normalized deflection of a triangular piezoelectric cantilever beam ( $r = 0$ ) with no tip mass

Figure 62 presents the maximum percentage error of the normalized deflection of tapered piezoelectric beams ( $r = 1, 0.8, 0.6, 0.4, 0.2$  and  $0$ ), all with no tip mass. It is quite clear that the rectangular beam has the lowest maximum percentage error (about 3%) as compared with all other tapered beams. As the taper ratio of the piezoelectric beam decreases, the maximum percentage error increases and reaches up to 9% for the taper ratio of  $r = 0$ .

These results indicate that the low accuracy of LPM is associated with the linearly tapered piezoelectric cantilever beams with no tip mass. Next, the tip mass effect on the LPM accuracy is investigated.

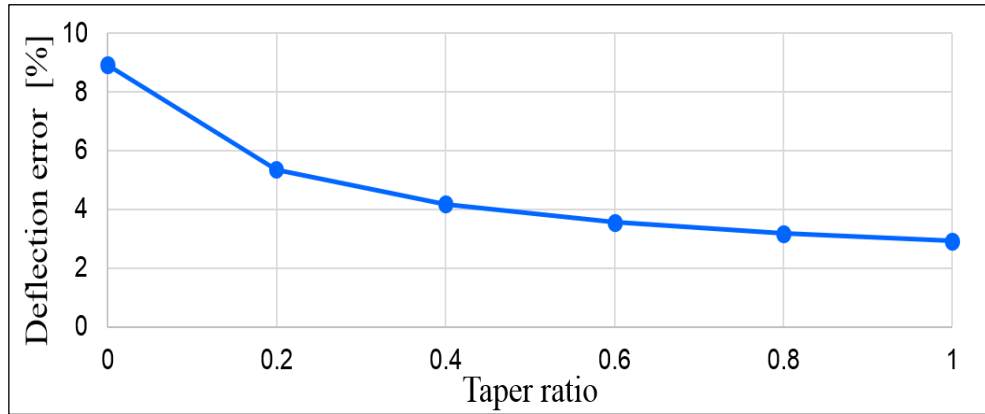


Figure 62: Maximum percentage error of the normalized deflection of different tapered piezoelectric cantilever beams ( $r = 1, 0.8, 0.6, 0.4, 0.2$  and  $0$ ) with no tip mass

Figure 63 shows the maximum percentage error of the normalized deflection of a number of tapered piezoelectric cantilever beams ( $r = 1, 0.8, 0.6, 0.4, 0.2$  and  $0$ ) when each beam is subjected to a number of tip mass ratios ( $a = 0, 0.1, 0.2, 0.5, 1, 2, 3$  and  $5$ ). The charts indicate that the maximum percentage error of the normalized deflection is quite high for small tip mass ratios ( $a < 0.2$ ). As the tip mass ratio increases, the maximum percentage error of the normalized deflection decreases noticeably. The maximum percentage error drops below 0.5% for tip mass ratios higher than 2.

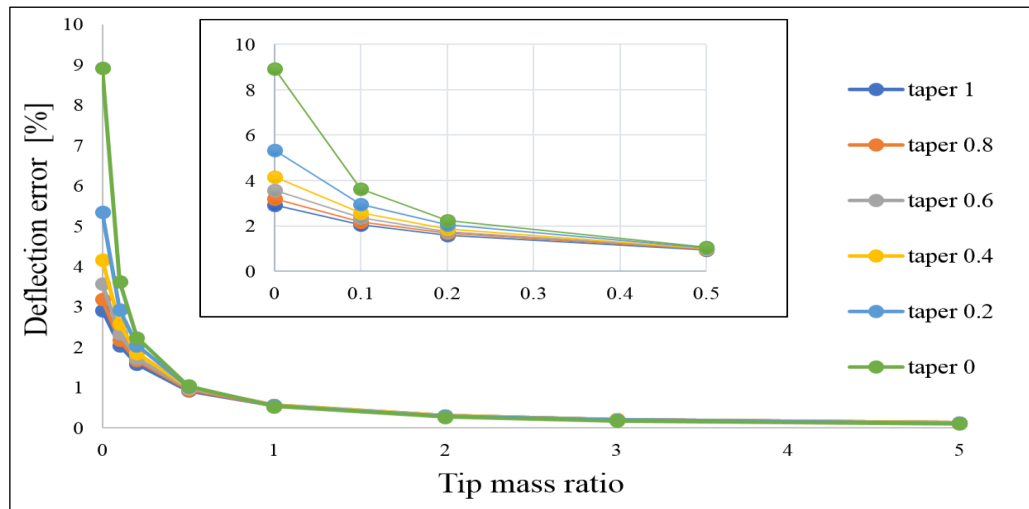


Figure 63: The maximum percentage error of the normalized deflection of different tapered piezoelectric cantilever beams with different tip mass ratios

### 6.2.2 The accuracy of the LPM for optimal piezoelectric cantilever (irregular shape)

This subsection discusses the accuracy of the LPM for the optimized piezoelectric cantilever configuration developed in Section 6.1. Figure 64 illustrates the normalized deflection of the LPM and the FEM. With tip mass ratio of  $a = 2$ , both the LPM and FEM give the same normalized deflection behavior along the beam length. In the absence of the tip mass, the normalized deflection of the two models separated away. This gives an important indication that the LPM of the optimal piezoelectric cantilever has some limitations in displaying the vibrational behavior of the cantilever accurately when no tip mass is subjected to the beam.

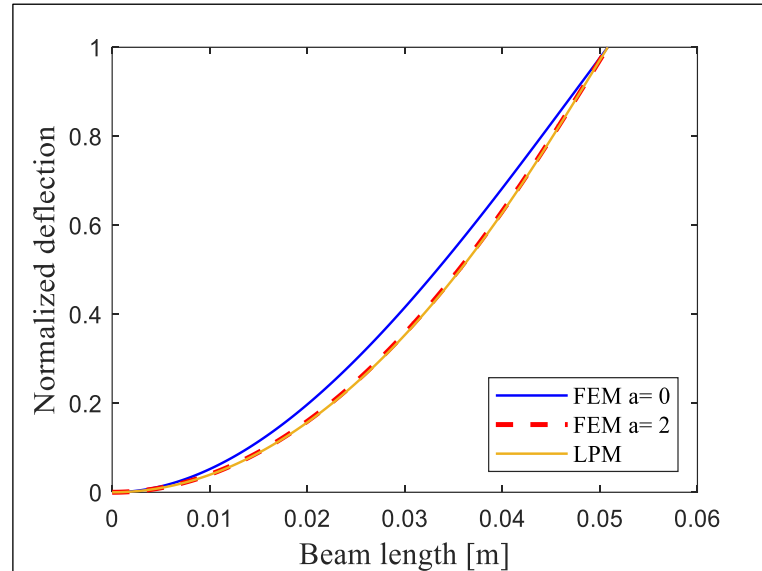


Figure 64: Comparison between the normalized deflection of the FEM and the LPM for the optimal piezoelectric cantilever design

The percentage error of the normalized deflection for the optimal piezoelectric is displayed in Figure 65. The maximum percentage error of the optimal design reaches to around 7%. The percentage error in the deflection reflects the limitation of the LPM in capturing the accurate vibrational behavior of the optimal piezoelectric cantilever beam.

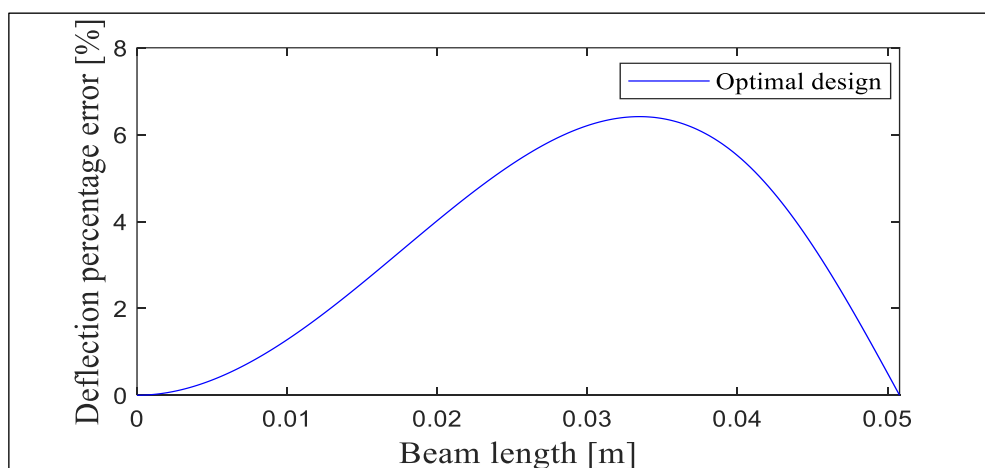


Figure 65: Percentage error of the normalized deflection for the optimal piezoelectric cantilever beam with no tip mass

The effect of the tip mass on the accuracy of the LPM for the optimal design is studied in Figure 66. The figure reveals that the deflection error is at the maximum rate when no tip mass is subjected to the optimal piezoelectric cantilever. A noticeable decrease in the deflection error comes with the increase of the tip mass ratio. This proves that for tip mass ratios of 2 and above, the LPM has a very good accuracy in mimicking the FEM. However, for tip mass ratios less than 2, a correction factor is required to enhance the LPM accuracy.

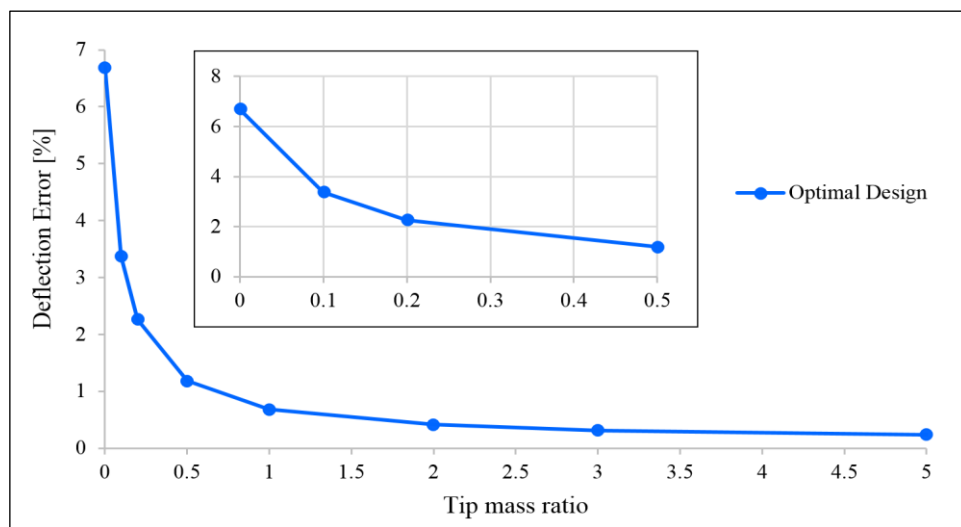


Figure 66: The maximum percentage error of the normalized deflection of the optimal piezoelectric cantilever subjected to different tip mass ratios

### 6.3 The development of correction factor for the LPM of tapered piezoelectric harvester

The previous section concluded that the LPM could be used when a large tip mass is subjected to a piezoelectric cantilever beam. However, for small tip masses, the LPM showed poor accuracy. Thus, a correction factor should be developed to increase the accuracy of the LPM. Researchers developed a correction factor of the LPM for rectangular and exponentially tapered piezoelectric beam [19], [127]. This section presents the development of the correction factor of LPM for tapered

piezoelectric cantilever using the FEM as a reference instead of the DPM. The estimation of the correction factor is based on the relative tip displacement transmissibility function. First, the relative tip displacement transmissibility function of the LPM is produced using equation (92) in the mathematical model chapter. Then the relative tip displacement transmissibility function of the FEM approach is used as a substitute to the DPM (equation (111)). The correction factor is then computed as  $CF = T_{rel}^{FEM} / T_{rel}^{LPM}$ . All the mechanical and geometrical properties are taken from Table 8 and Table 9. The only change is in the tip beam width which is obtained from the taper ratio 'r' definition.

### 6.3.1 Correction factor of linearly tapered piezoelectric cantilever

Figure 67 presents the relative tip displacement transmissibility function of the LPM for linearly tapered piezoelectric cantilever. The relative transmissibility of the LPM is  $\frac{1}{2\zeta}$  meaning that it is the same for any piezoelectric cantilever shape.

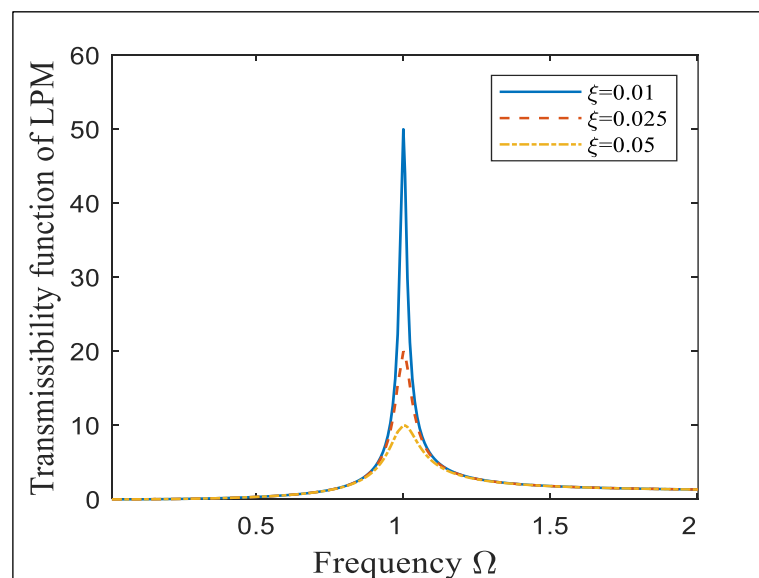


Figure 67: Relative tip displacement transmissibility function of the LPM for linearly tapered piezoelectric cantilever beam with no tip mass



Figure 68 shows the relative tip displacement transmissibility function of the FEM for linearly tapered piezoelectric cantilever beams of ratios ( $r = 0.8, 0.6, 0.4, 0.2$  and  $0$ ). All these tapered cantilever beams have no tip mass. The results show that the LPM in Figure 67 gives less vibration response compared to their equivalent FEM in Figure 68. For example, for taper ratio ( $r = 0.8$ ) given  $\zeta = 0.01$ , the transmissibility function of the LPM is about 50 whereas for FEM is 79.9 as both are measured at resonance. For taper ratio ( $r = 0$ ) given  $\zeta = 0.01$ , the transmissibility functions of the LPM and DPM are 50 and 110, respectively. The results show that as the beam taper ratio decreases, the relative transmissibility functions of the LPM differ significantly from the FEM. Therefore, correction factor estimation is of crucial importance to increase the accuracy of estimating the vibration response of the linearly tapered piezoelectric beam when using the LPM.

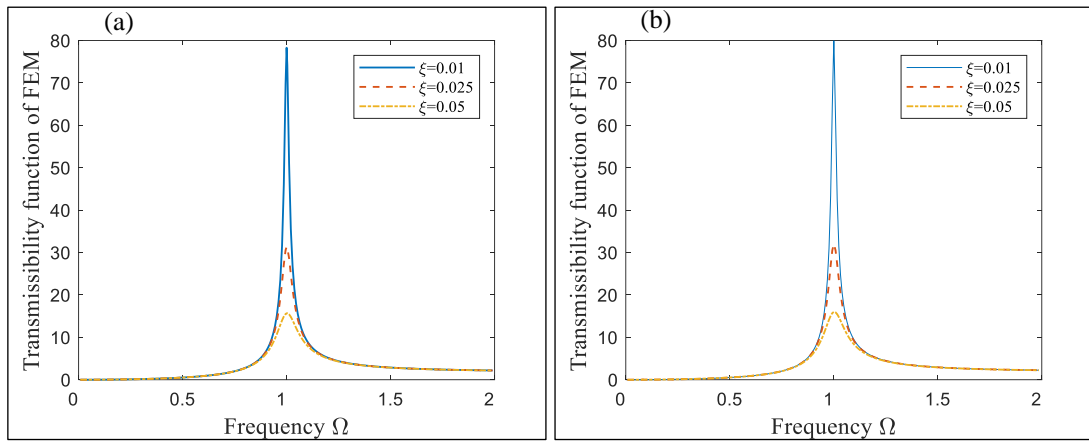
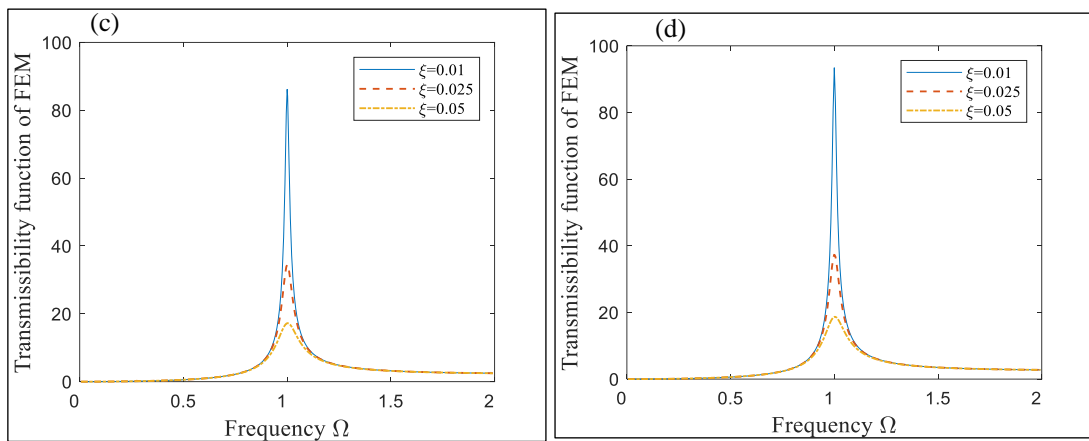
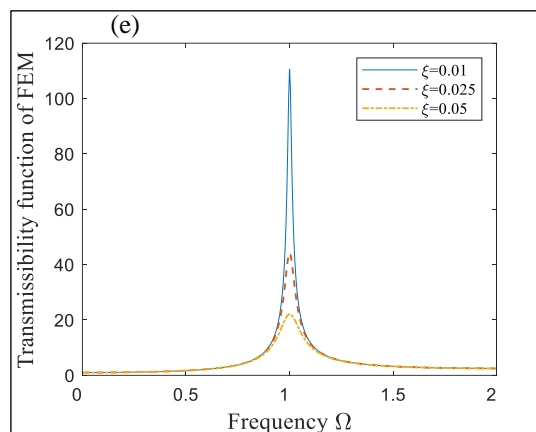
(a)  $r = 0.8$ (b)  $r = 0.6$ (c)  $r = 0.4$ (d)  $r = 0.2$ (e)  $r = 0$ 

Figure 68: Relative tip displacement transmissibility function of the FEM for different tapered piezoelectric cantilever beams with no tip mass

The percentage error in using the LPM to predict the vibration response of linearly tapered piezoelectric cantilever harvester is illustrated in Figure 69. The error is introduced as a relative error given by:

$$\text{Relative Error} = \frac{T_{rel}^{FEM} - T_{rel}^{LPM}}{T_{rel}^{FEM}} \times 100 \quad (113)$$

The relative error of LPM is shown for taper ratios of ( $r = 1, 0.8, 0.6, 0.4, 0.2$  and  $0$ ) with no tip mass for a given  $\zeta = 0.01$ . The figure shows that as the taper ratio decreases to reach  $r = 0$ , which is a triangular shape, the relative error increases radically to reach 55%. The bizarre behavior of the relative error around the resonance is as a result of an error in the natural frequency estimated by the LPM. When the taper ratio decreases, the error in natural frequency prediction increases until it reaches about 8% for taper ratio  $r = 0$  (triangular shape). Table 13 shows the error of predicating the natural frequency using LPM and the one obtained from the FEM.

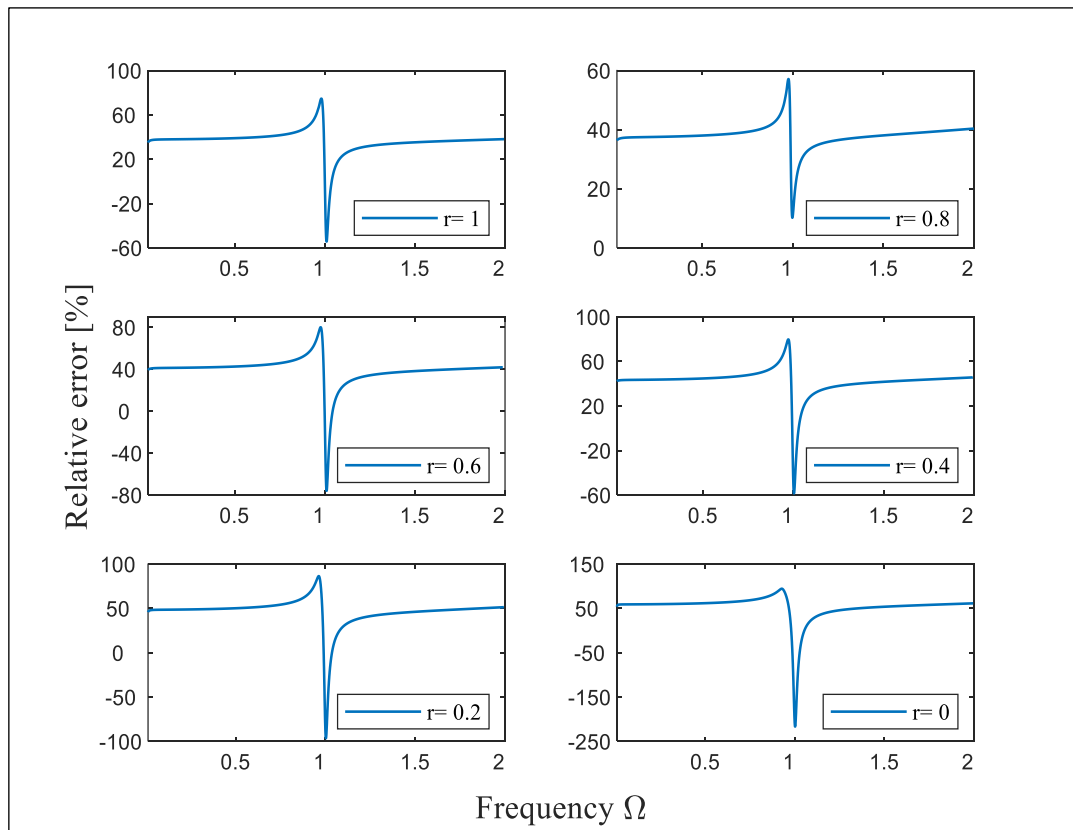


Figure 69: Relative error of LPM for different linearly tapered ratios of a piezoelectric cantilever beam with no tip mass given for  $\zeta = 0.01$

Table 13: Natural frequency of LPM and FEM with the corresponding error between the two models

Taper ratio ( $r$ )	Natural Frequency of LPM (Hz)	Natural Frequency of FEM (Hz)	Relative Error (%)
1	120.3335	118.5852	1.47
0.8	129.0254	126.9071	1.67
0.6	140.8876	138.1746	1.96
0.4	158.4719	154.6429	2.48
0.2	188.6084	182.0342	3.61
0	255.5055	237.122	7.75

Figure 70 shows the correction factor for the first vibration mode of linearly tapered piezoelectric cantilever harvesters. Corrections factors of taper ratio ( $r =$

0, 0.2, 0.4, 0.6, 0.8 and 1) are estimated using the FEM. From the results, the highest correction factor is required for the triangular tapered beam that has no tip mass. The effect of the mass ratio is also analyzed in this study. The graph indicates that for small tip masses ( $a < 0.5$ ), the correction factor decreases as taper ratio increases from 0 to 1. However, for  $a \geq 0.5$  the taper ratio does not show any effect and the correction factor becomes the same for all taper ratios. As the mass ratio further increases the correction factor magnitude decreases asymptotically towards unity. This means that for high mass ratios ( $a \geq 5$ ) the uncorrected LPM can give accurate approximations.

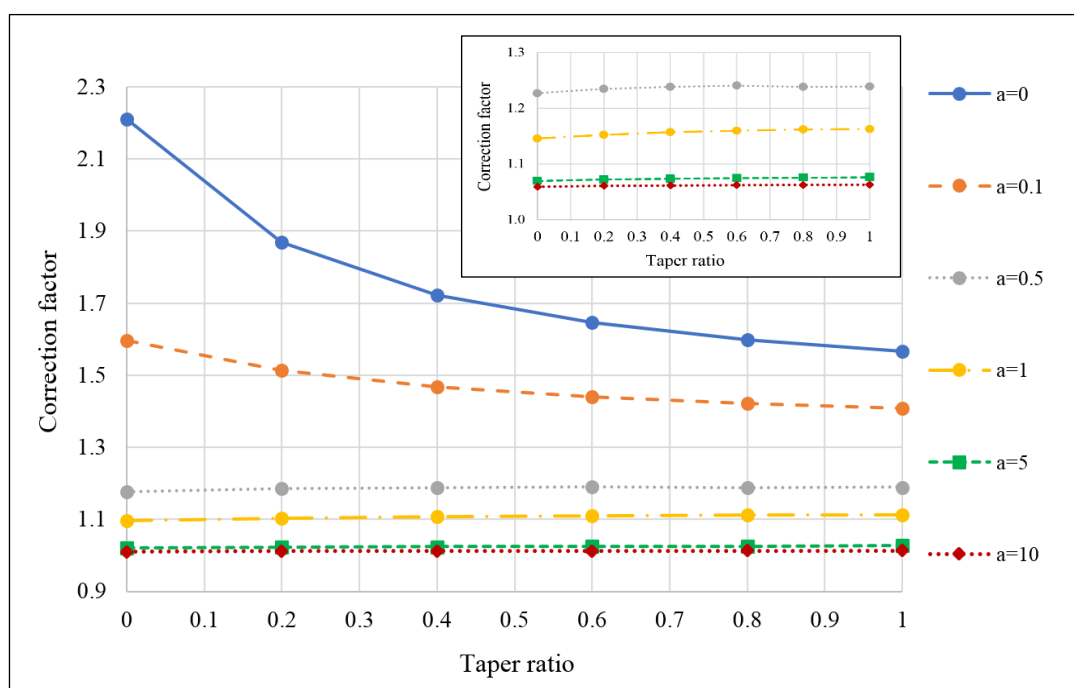


Figure 70: Correction factor for the first mode of different linearly tapered piezoelectric ratios subjected to different mass ratios

Nevertheless, the correction factor must be used for small tip masses and considering the related taper ratio of the linearly tapered piezo beam to get the correct vibration response. Table 14 gives a detailed insight into all the correction factors of different taper ratios and mass ratios along with the associated error.

Table 14: Correction factor for the fundamental vibration mode of linearly tapered piezoelectric beams subjected to different mass ratios

Taper Ratio ( $r$ )	Mass Ratio ( $a$ )											
	0	Error* (%)	0.1	Error* (%)	0.5	Error* (%)	1	Error* (%)	5	Error* (%)	10	Error* (%)
0	2.21180	54.79	1.59686	37.38	1.17703	15.04	1.09573	8.74	1.01962	1.92	1.00948	0.94
0.2	1.86831	46.48	1.51324	33.92	1.18473	15.59	1.10212	9.27	1.02229	2.18	1.01096	1.08
0.4	1.72300	41.96	1.46803	31.88	1.18850	15.86	1.10728	9.69	1.02362	2.31	1.01158	1.14
0.6	1.64625	39.26	1.44033	30.57	1.19045	16.00	1.10936	9.86	1.02479	2.42	1.01214	1.20
0.8	1.59858	37.44	1.42143	29.65	1.18805	15.83	1.11187	10.06	1.02565	2.50	1.01255	1.24
1	1.56593	36.14	1.40761	28.96	1.18899	15.89	1.11263	10.12	1.02625	2.56	1.01285	1.27

Error\*: Error of the uncorrected LPM calculated by  $\frac{1-CF}{CF}$  where  $CF$  is the correction factor

Figure 71 presents the transmissibility functions obtained from the FEM, corrected LPM (C-LPM) and the LPM for piezoelectric cantilever taper ratios of ( $r = 0.8, 0.6, 0.4, 0.2$  and  $0$ ) given the damping ratio  $\zeta = 0.01$ . Results show that the magnitude of the relative transmissibility function of the C-LPM matches the one of the FEM. The results confirm the necessity of using a correction factor when using the LPM to give an accurate vibration response that can predict the power production of the linearly tapered piezoelectric harvesters precisely.

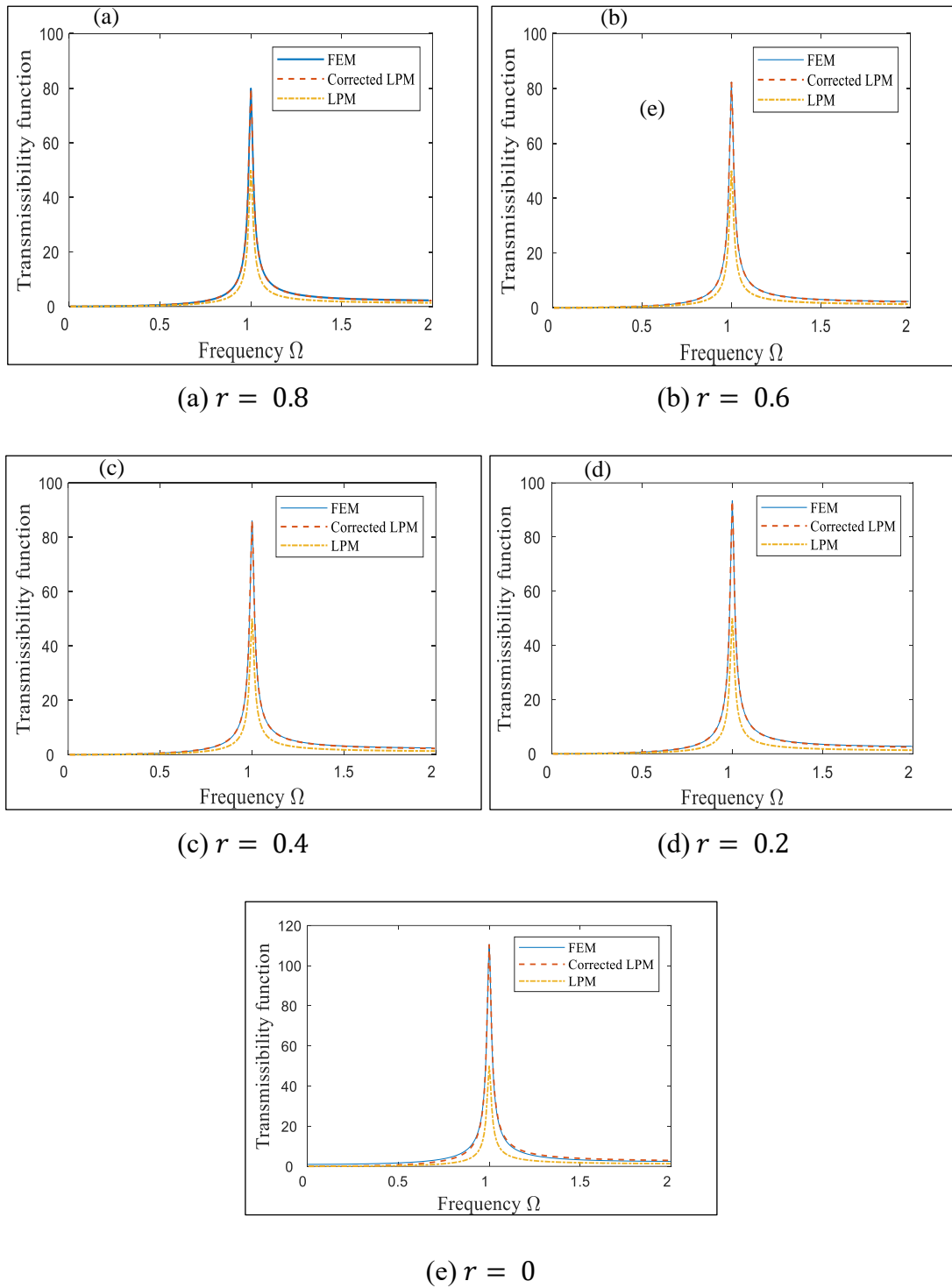


Figure 71: Relative tip displacement transmissibility functions obtained from FEM, C-LPM and LPM for different taper ratios for given  $\zeta = 0.01$



### 6.3.2 Correction factor of optimal piezoelectric cantilever (irregular shape)

This section is a reproduction of the correction factor development process but for the optimal piezoelectric cantilever beam. Figure 72 shows the relative tip displacement transmissibility function of the optimal design when no tip mass is added. The relative transmissibility of the LPM for  $\zeta = 0.01$  is 50 whereas for the FEM is 98.3. The difference between the two models indicates that the LPM cannot capture the tip motion of the optimal cantilever accurately.

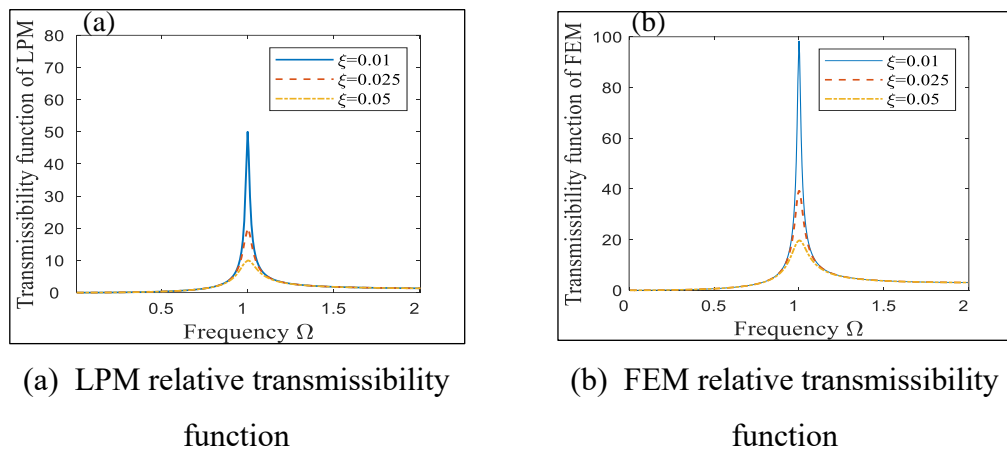


Figure 72: Relative tip displacement transmissibility function for the optimal piezoelectric beam with no tip mass

Figure 73 presents the relative error of using the LPM for the optimal piezoelectric cantilever beam. The relative error reaches 49%. The natural frequencies of the LPM and FEM are 215.2 Hz and 206.3 HZ respectively. The error between the two models in predicting the natural frequency reaches 4.3% for the optimal design. This explains the strange behavior around the normalized frequency in Figure 73.

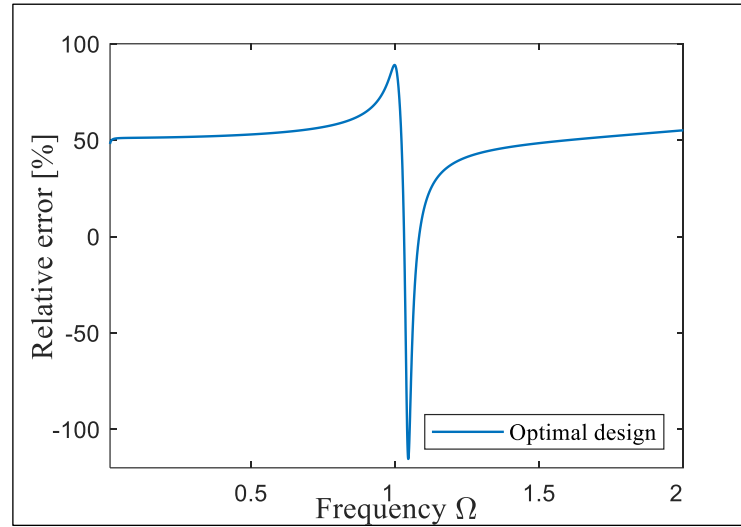


Figure 73: Relative error of LPM for the optimal piezoelectric cantilever beam with no tip mass for  $\zeta = 0.01$

The developed correction factor of the optimal piezoelectric cantilever beam subjected to different tip mass ratios is presented in Figure 74. The correction factors for tip mass ratios of ( $a = 0, 2, 5, 10, 15$  and  $20$ ) are originated using FEM. The highest correction factor is required for the optimal design with no tip masses added ( $CF = 1.95162$ ). As the tip mass ratio increases, the correction factor reaches to unity which means that the LPM is more accurate when large tip masses are added to the piezoelectric cantilever beam. Table 15 gives more details on all the correction factors of different mass ratios for the optimal design along with the percentage error. That data represented in this table for  $T_{rel}^{FEM}$  and  $T_{rel}^{LPM}$  is for given  $\zeta = 0.027$ . However, the CF are valid for the optimal piezoelectric cantilever regardless of the damping ratios.

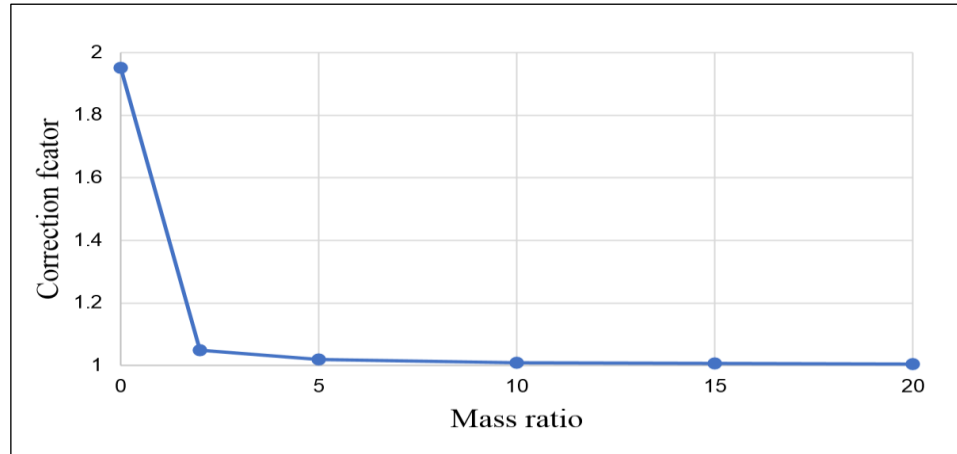


Figure 74: Correction factor of the optimal design for different tip mass ratios developed by FEM

Table 15: Correction factor for the fundamental vibration mode of the optimal design subjected to different mass ratios

$a$	$M_t$	$T_{rel}^{FEM}$	$T_{rel}^{LPM}$	CF	Error*
0	0	36.41061	18.51852	1.95162	48.8%
2	0.0089	19.41028	18.51852	1.04816	4.59%
5	0.0223	18.87917	18.51852	1.01948	1.91%
10	0.045	18.69083	18.51852	1.00930	0.92%
15	0.067	18.62495	18.51852	1.00575	0.57%
20	0.0895	18.58927	18.51852	1.00382	0.38%

Error\*: Error of the uncorrected LPM calculated by  $(1-CF)/CF$  where  $CF$  is the correction factor

Applying the developed correction factor to the LPM increases the accuracy of the LPM in modeling the optimal piezoelectric cantilever beam. This is illustrated clearly in Figure 75 where the relative transmissibility function using the corrected LPM (C-LPM) matches almost exactly the FEM. This validates the importance of using the correction factor

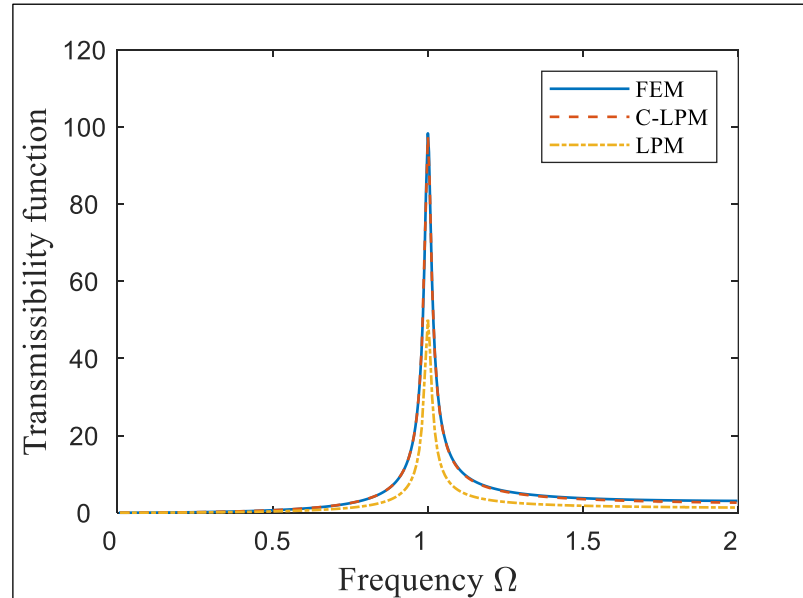


Figure 75: Relative tip displacement transmissibility functions obtained from FEM, C-LPM and LPM for the optimal piezoelectric cantilever design given  $\zeta = 0.01$

#### 6.4 Verification of the C-LPM for an electromechanical piezoelectric harvester

This section shows the comparisons of the corrected LPM (C-LPM) and FEM for different geometries of piezoelectric cantilever beam as well as the optimal design developed earlier in Section 6.1. The comparison between LPM and FEM is based on the study of tip deflection, tip velocity, voltage and surface power density. Surface power density is defined as a power per surface area of the piezoelectric harvester. It is a useful tool that is used to understand the performance of piezoelectric harvester.

##### 6.4.1 Verification of the integrated linearly tapered piezoelectric harvester in FEM

This section presents the validity of the corrected LPM (C-LPM) using an integrated piezoelectric harvester developed in FEM. Comparisons between the C-LPM and FEM are studied for different parameters like voltage and surface power density to give an insight into the power harvested using tapered piezoelectric beams.

Figure 76 presents the FEM and (C-LPM) for rectangular piezoelectric beam of ( $r = 1$ ) with tip mass 0.012 and damping ratio 0.027. for load resistance 470 k $\Omega$ , the voltage output for the FEM is 96.33 V/g, whereas for the C-LPM is 95.56. The surface power density for the FEM and the C-LPM are  $6.11 \times 10^3$  [(mW/g<sup>2</sup>)/m<sup>2</sup>] and  $6.01 \times 10^3$  [(mW/g<sup>2</sup>)/m<sup>2</sup>], respectively. From the stated results, the C-LPM for voltage and surface power density are in very agreement with the FEM. The correction factor used in this model is given by ( $CF = 1.085278$ ).

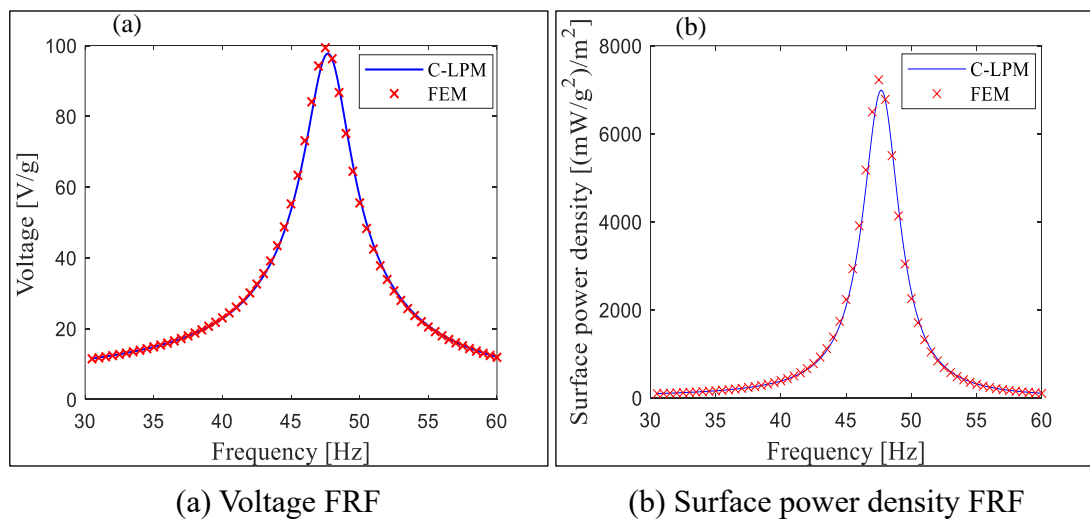


Figure 76: Comparison between C-LPM and FEM for rectangular piezoelectric beam ( $r = 1$ ) with load resistance of 470 k $\Omega$

Figure 77 displays the FEM and the C-LPM for tapered piezoelectric beam of ( $r = 0.8$ ). For load resistance of 470 k $\Omega$ , the voltage output of the FEM is about 99 V/g, whereas for the C-LPM is 97.7 V/g. The surface power density for the FEM is  $7.23 \times 10^3$  [(mW/g<sup>2</sup>)/m<sup>2</sup>] and for C-LPM is  $6.99 \times 10^3$  [(mW/g<sup>2</sup>)/m<sup>2</sup>]. The good match between the FEM and C-LPM of different parameters shows the consistency of the developed model. The correction factor used in this model is given by ( $CF = 1.076599$ ).

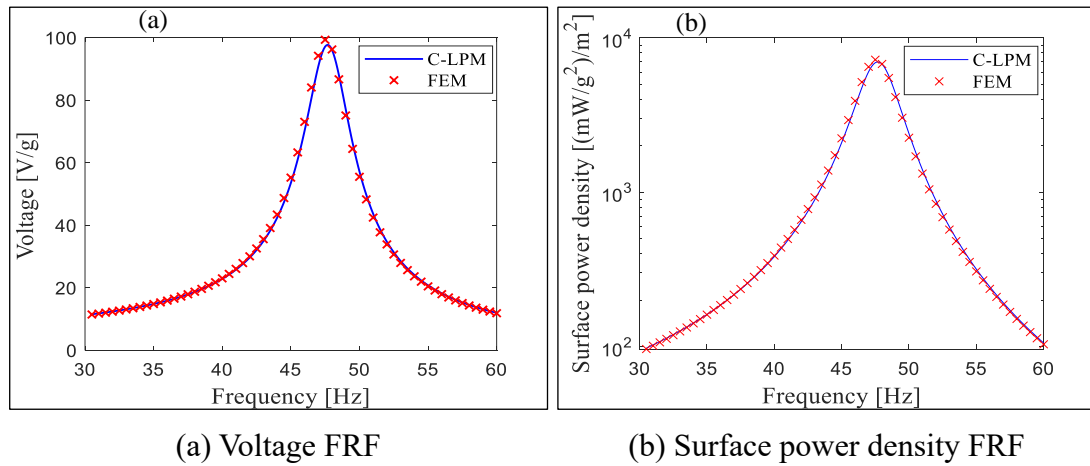


Figure 77: Comparison between C-LPM and FEM for tapered piezoelectric beam of ratio ( $r = 0.8$ ) with load resistance of  $470 \text{ k}\Omega$

The tapered piezoelectric cantilever of ratio ( $r = 0.6$ ) is shown in Figure 78. The frequency of the FEM is  $46.5 \text{ Hz}$ , whereas for C-LPM is  $47 \text{ Hz}$ . The voltage output of the FEM and C-LPM are  $101.52 \text{ V/g}$  and  $99.89 \text{ V/g}$ . The surface power density for the FEM is  $8.48 \times 10^3 \text{ [(mW/g}^2\text{)/m}^2\text{]}$  and for C-LPM is  $8.21 \times 10^3 \text{ [(mW/g}^2\text{)/m}^2\text{]}$ . The error between the FEM and C-LPM for the voltage output is around  $1.6\%$ . The correction factor used in this model is given by ( $CF = 1.06735914$ ).

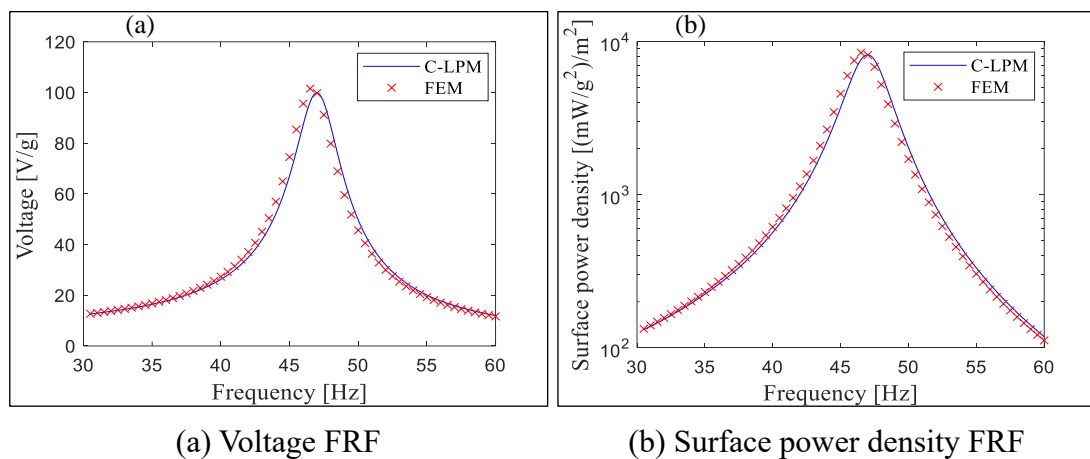


Figure 78: Comparison between C-LPM and FEM for tapered piezoelectric beam of ratio ( $r = 0.6$ ) with load resistance of  $470 \text{ k}\Omega$

Figure 79 illustrates the results of LPM and C-LPM of taper ratio ( $r = 0.4$ ). The frequencies of the FEM and C-LPM are 45.5 Hz and 46.1 Hz. The voltage output of the FEM and C-LPM are 104.03 V/g and 101.82 V/g. The surface power density for of FEM is about  $1.018 \times 10^4$  [(mW/g<sup>2</sup>)/m<sup>2</sup>], whereas for C-LPM is  $9.753 \times 10^3$  [(mW/g<sup>2</sup>)/m<sup>2</sup>]. The error of the voltage between the two models is about 2.1%. The correction factor used in this model is given by ( $CF = 1.057474$ ).

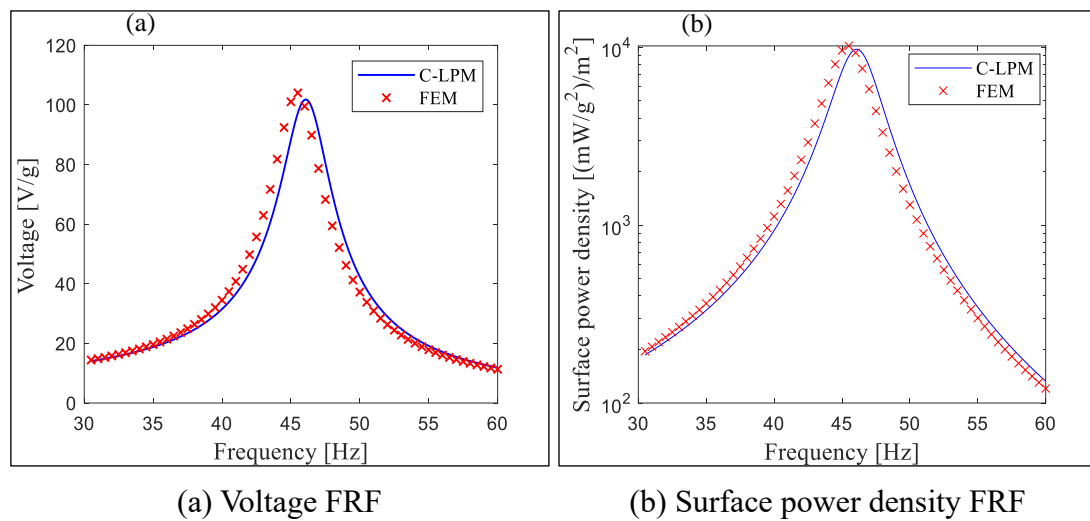


Figure 79: Comparison between C-LPM and FEM for tapered piezoelectric beam of ratio ( $r = 0.4$ ) with load resistance of 470 kΩ

Figure 80 presents a comparison between LPM and C-LPM of taper ratio ( $r = 0.2$ ). The frequencies of the FEM and C-LPM are 44 Hz and 44.8 Hz respectively. The voltage outputs of the FEM and C-LPM are 105.4 V/g and 103.4 V/g respectively. The error is around 2%. The surface power density for of FEM is about  $1.22 \times 10^4$  [(mW/g<sup>2</sup>)/m<sup>2</sup>] whereas for C-LPM is  $1.17 \times 10^4$  [(mW/g<sup>2</sup>)/m<sup>2</sup>]. The correction factor used in this model is given by ( $CF = 1.046802$ ).

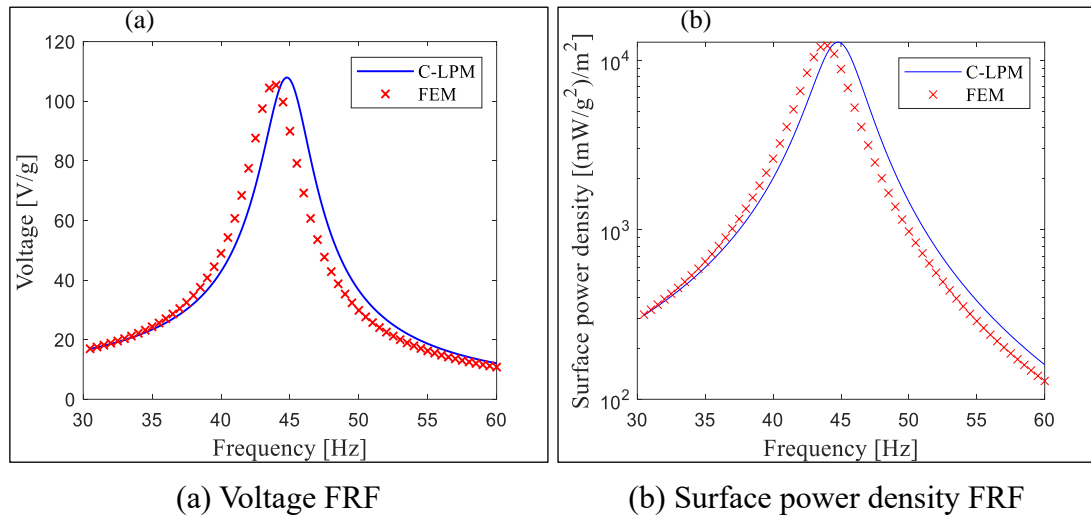


Figure 80: Comparison between C-LPM and FEM for tapered piezoelectric beam of ratio ( $r = 0.2$ ) with load resistance of 470 k $\Omega$

#### 6.4.2 Verification of the integrated optimal tapered piezoelectric harvester in FEM

The comparison of FEM and C-LPM of the developed optimum design is presented in Figure 81. The frequencies of FEM and C-LPM are 41.5 Hz and 42.5 Hz. The voltage of FEM and C-LPM are 107.3 V/g and 105.2 V/g. The error between the C-LPM and FEM is 1.96%. The surface power density of FEM is about  $1.46 \times 10^4$  [(mW/g<sup>2</sup>)/m<sup>2</sup>] whereas for C-LPM is  $1.40 \times 10^4$  [(mW/g<sup>2</sup>)/m<sup>2</sup>]. The correction factor used in this model is given by ( $CF = 1.03549482$ ).



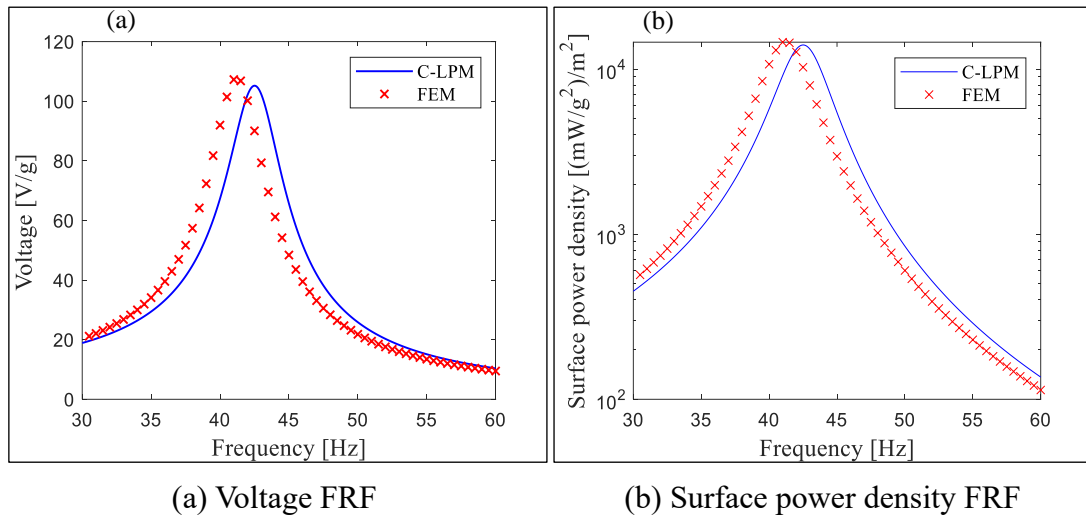


Figure 81: Comparison between C-LPM and FEM for optimal design with load resistance of 470 kΩ

As it is noticed in the previous studied figures that there is a shift in the frequency between the C-LPM and FE. This shift increases as the taper ratio goes from ( $r = 1$ ) up to the optimal design. The literature indicated that there is an error of 1.5% between the natural frequency of the DPM and LPM for the rectangular piezoelectric harvester [109]. Furthermore, Table 16 shows that the error in predicting the natural frequency between the LPM and FEM can reach up to 7% for triangular piezoelectric beam. Figure 82 studies the voltage output of FEM and C-LPM for optimal design subjected to different tip mass ratios. The results showed that as you increase the tip mass ratio the error in the frequency between C-LPM and FEM decreases. The error in the frequency for taper ratio ( $a = 2.67$ ) reaches 3.68% (Table 16). At taper ratio ( $a = 20$ ) the frequency dropped to 2.8%. The effect of the tip mass on the frequency shift might be minor. However, this study is an attempt to understand the behavior of the two models taken in consideration different parameters.

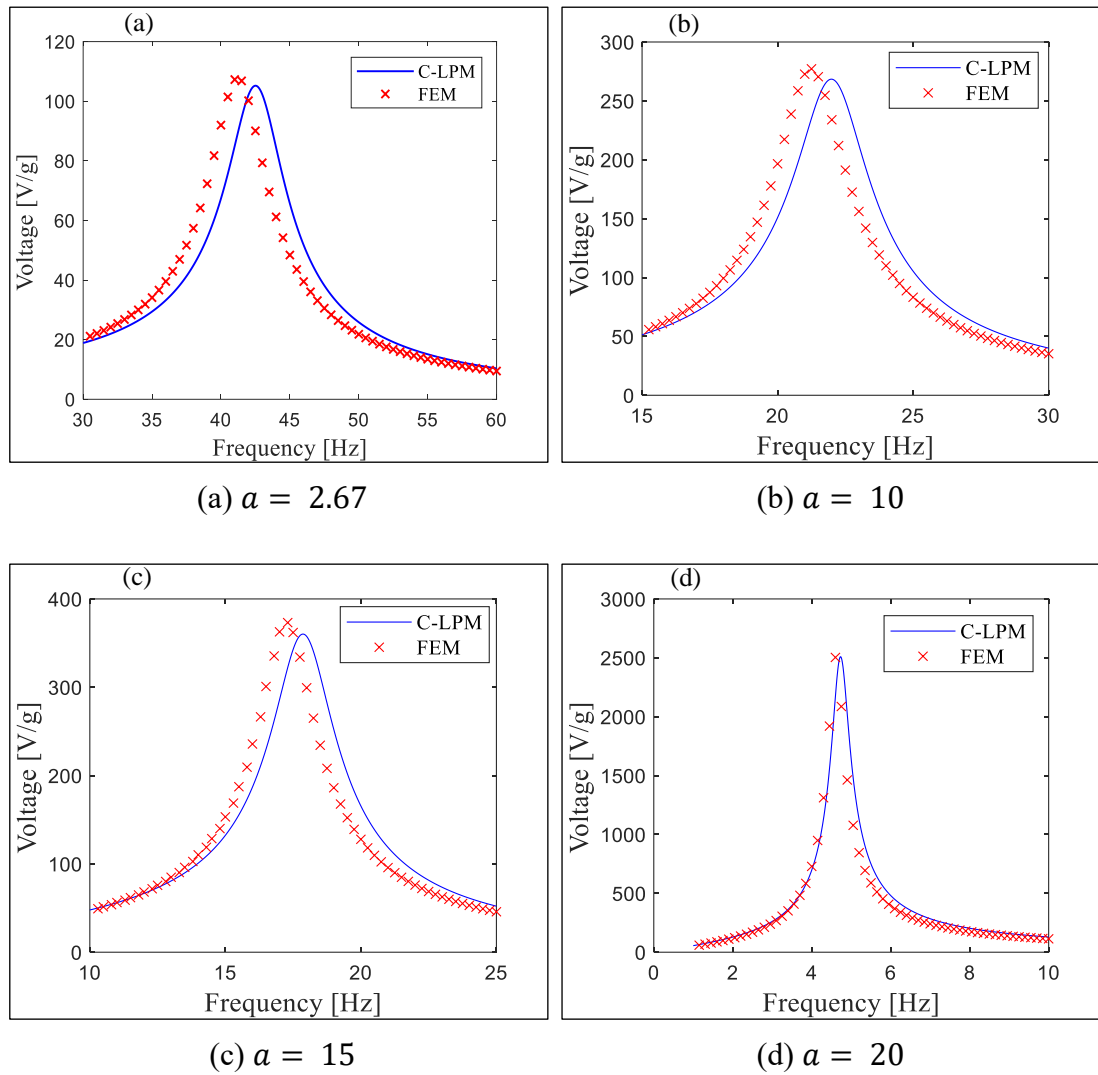


Figure 82: Comparison between voltage output of FEM and C-LPM for optimal design with load resistance of 470 k $\Omega$  subjected to different tip mass ratios

Table 16: Error of FEM and C-LPM frequencies for optimal design with load resistance of 470 k $\Omega$  subjected to different tip mass ratios

Tip mass ratio ( $a$ )	Frequency [Hz]		Error (%)
	FEM	C-LPM	
2.67	41	42.51	3.7
10	21.25	21.99	3.5
15	17.30	17.86	3.1
20	4.6	4.73	2.8

This section studied the C-LPM for different tapered piezoelectric cantilever beams and the optimized design. The aim of the comparison between the C-LPM and FEM was to measure how accurate and precise is the LPM when using the developed correction factor. Results showed as the taper ratio increases from the rectangular shape ( $r = 1$ ) up to the optimal shape, the error between the C-LPM and FEM increased in voltage and surface power density to reach up to 2% and 4% respectively. This error can be due to limitations in meshing FEM of the piezoelectric cantilever. However, despite the resulted errors, the accuracy of the C-LPM showed a great improvement in predicting the power harvested of different tapered piezoelectric cantilever beams.

### **6.5 Parametric study on optimal piezoelectric harvester**

The parametric study in this section included three main studies. The first study was on the effect of the load resistance on the performance of the optimal design piezoelectric harvester. Several load resistances were investigated. The optimum resistance was also included for two extreme conditions of short and open circuits excitation frequencies. The peak power and surface power density of an optimal design with an optimum load resistance were then stated. The second study scrutinized the effect of tip mass ratios defined as  $\left(a = \frac{M_t}{ml}\right)$  on the optimal design harvester. The third study looked at the effect of different types of piezoelectric materials (PZT-5A, PZT-5H and PZT-5J) on the power production of the optimal piezoelectric cantilever harvester. It is important to highlight that the parametric study is done for an optimal design without changing the width ratio of the piezoelectric cantilever (kept the same as Table 12).

### 6.5.1 Load resistance effect

The effect of load resistance on the optimal design is studied in Figure 83. Eight different magnitudes of load resistance are investigated ( $R = 1, 6, 12, 22, 33, 47, 100$  and  $470 \text{ k}\Omega$ ). Figure 83(a) & (b) show the tip velocity and voltage for each load resistance value. The direction of increasing  $R$  is displayed in the figure. The tip velocity doesn't exhibit a steady behavior with increasing the load resistance value. For frequency  $39.92 \text{ Hz}$  the tip velocity is  $0.7391 \text{ [(m/s)/g]}$ . As the load resistance increases, the tip velocity decreases until it reaches to frequency  $42.51 \text{ Hz}$  for load resistance of  $470 \text{ k}\Omega$  where it increases back to reach to  $0.4024 \text{ [(m/s)/g]}$ . The voltage, unlike the tip velocity, increases with the increase of the load resistance at each resonance frequency. In Figure 83(b) the voltage strikes from  $1.18 \text{ [V/g]}$  in close circuit at resonance  $39.92 \text{ Hz}$  to  $105.26 \text{ [V/g]}$  in open circuit at resonance  $42.51 \text{ Hz}$ .

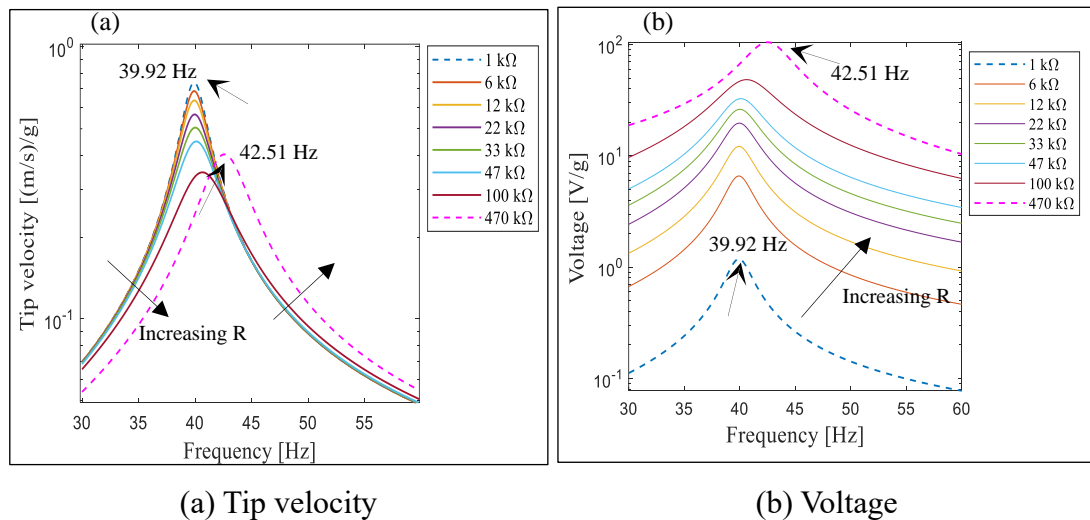


Figure 83: FRF of optimal design with different load resistance magnitudes for damping ratio of  $\zeta = 0.027$  and tip mass  $M_t = 0.012 \text{ kg}$

Figure 84 shows the current FRF and surface power density FRF for different load resistance values of an optimal design. The current decreases as the load resistance value increases. For load resistance of 1 k $\Omega$  the current is 0.84 [mA/g] whereas for load resistance of 460 k $\Omega$  the current is 0.40 [mA/g]. Figure 84(b) depicted the surface power density of three load resistance values (6, 33 and 470 k $\Omega$ ). The surface power densities of frequencies 39.92 Hz, 40.01 Hz and 42.51 Hz are 4320, 12421 and 14031 [(mW/g<sup>2</sup>)/m<sup>2</sup>] respectively. Results show that the surface power density increases with the increase of the load resistance magnitudes.

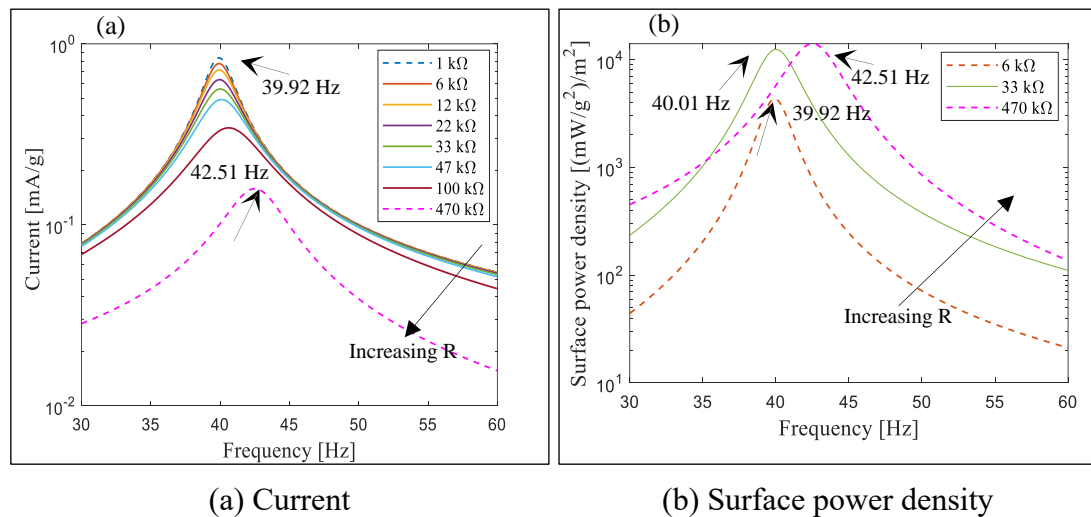


Figure 84: FRF of the optimal design with different load resistance magnitudes for damping ratio of  $\zeta = 0.027$  and tip mass  $M_t = 0.012$  kg

### 6.5.1.1 Optimum load resistance

For each excitation frequency there is a maximum power output of the piezoelectric cantilever harvester at a certain load resistance. This load resistance is defined as the optimum load resistance. Figure 85 shows the effect of load resistance on peak voltage, current and power. Two extreme conditions of excitation frequencies are studied. First is the short circuit excitation frequency of 39.92 Hz when  $R \rightarrow 0$  is investigated and then the open circuit excitation frequency of 42.51 Hz when  $R \rightarrow \infty$ . The

same damping ratio and tip mass ratio are used in this study. The peak voltage output in Figure 85(a) increases with the increase of load resistance for both resonance frequencies. The maximum peak voltage for resonance frequency 39.92 Hz is 73.96 [V/g] and for resonance frequency 42.51 Hz is 191.2 [V/g]. At a load resistance of 161 k $\Omega$  both short and open circuit resonance frequencies give the same voltage output of 55.2 V/g. Figure 85(b) illustrates the current output behavior with different load resistance. Opposite to the voltage, the current decreases as the load resistance increases. For both resonance frequency cases of 39.92 Hz and 42.51 Hz, the maximum peak currents are 1.18 and 0.47 [mA/g] respectively. At load resistance of 161 k $\Omega$  the peak current is the same for both short and open circuit resonance frequencies with a magnitude of 0.3376 [mA/g]. The peak powers of different load resistances are presented in Figure 85(c). The intersect between the two circuit conditions is at load resistance 161 k $\Omega$  with a peak power magnitude of 18.35 [mW/g<sup>2</sup>]. However, each circuit condition has an optimum load resistance. For short circuit resonance frequency of 39.92 Hz, the maximum power is 22.99 [mW/g<sup>2</sup>] given at 61 k $\Omega$  load resistance. For open circuit resonance frequency of 42.5 Hz, the maximum power is 23.64 [mW/g<sup>2</sup>] given at 411 k $\Omega$  load resistance. Note that the peak power presented in the previous figure is defined as  $P = \frac{|V|}{R}$  which is different from the average power that is defined as  $P_{avg} = \frac{|V_{rms}|}{R}$  where  $V_{rms}$  is  $\frac{|V|}{\sqrt{2}}$ .

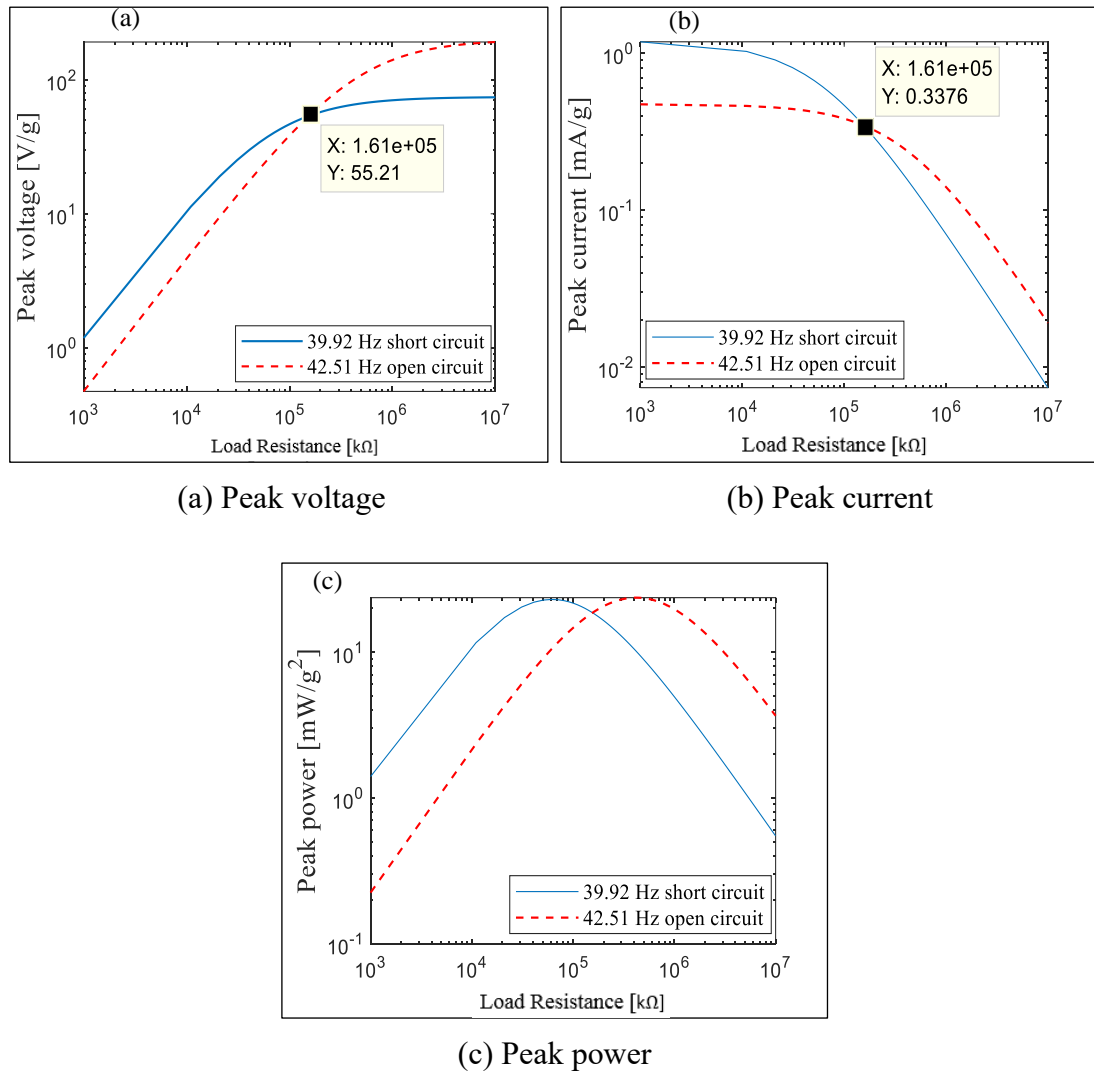


Figure 85: FRF of the optimal design with load resistance for short and open circuit resonance frequencies

The optimum load resistance of an optimal design with tip mass of  $M_t = 0.012$  is determined from equation (74) to be 186 kΩ which is between the two extreme conditions of short and open circuits studied previously in Figure 85. Figure 86 study the FRF of the optimal piezoelectric cantilever beam for voltage, current, power and surface power density at the optimal load resistance  $R_{opt}$ . The resonance frequency is 41.48 Hz and the natural frequency is 39.92 Hz. The peak voltage, current and power

are 75.58 [V/g] and 0.35 [mA/g] and 23.15 [mW/g<sup>2</sup>] respectively. The surface power density is  $1.38 \times 10^4$  [(mW/g<sup>2</sup>)/m<sup>2</sup>].

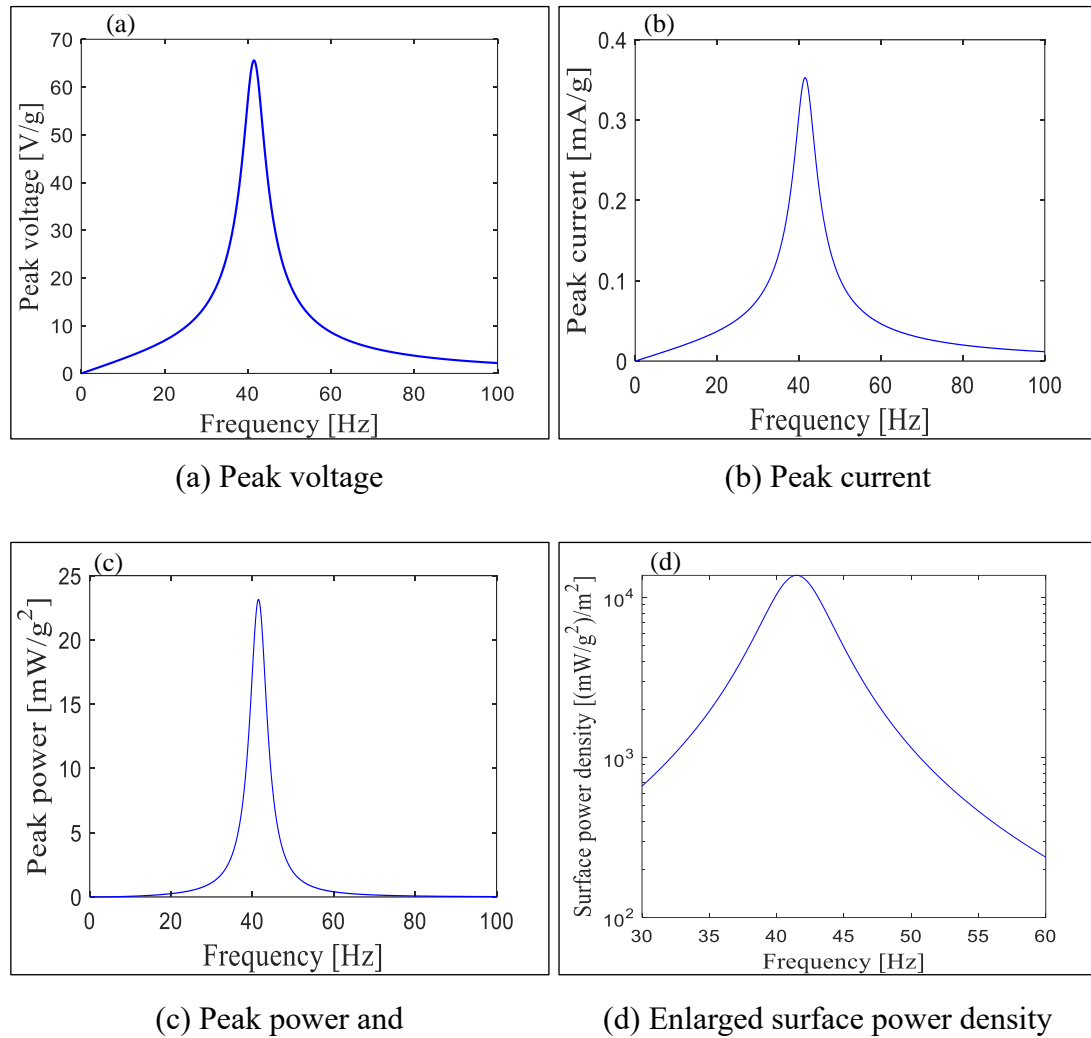


Figure 86: FRF of the optimal piezoelectric cantilever design with tip mass of  $M_t = 0.012$  at  $R_{opt}$

### 6.5.2 Tip mass ratios effect

Figure 87 shows the effect of different tip mass ratios ( $a = 0, 2, 5, 10, 15$  and  $20$ ) on tip deflection, tip velocity, voltage and surface power density of the optimal design. For each tip mass ratio, the compatible optimum load resistance  $R_{opt}$  is used. The figure shows that as the tip mass ratio increases the output



of tip deflection, tip velocity, voltage and surface power density increase accordingly. The highest values of the four investigated parameters are at tip mass ratio of ( $a = 20$ ). The maximum power and voltage are  $2.52 \times 10^5$  [(mW/g<sup>2</sup>)/ m<sup>2</sup>] and 459 [V/g] for resonance frequency 15.42 Hz and load resistance 500 k $\Omega$ . The lowest performance of the optimal piezoelectric harvester is when no tip mass is subjected to the harvester ( $a = 0$ ). As the tip mass ratio increases the resonance frequency decreases. The resonance frequencies of the studied tip mass ratios ( $a = 0, 2, 5, 10, 15$  and  $20$ ) are  $\omega_r = 223.6, 47.88, 30.68, 21.77, 17.14$  and  $15.42$  Hz. Due to the inverse relationship between the frequency and the optimal load resistance as in equation (74), the optimal resistance increases with the decrease of the frequency. As the tip mass ratio increases (which results in a decrease in the frequency), The optimal load resistance increases. Notice that for each tip mass, the correction factor is used accordingly to obtain the C-LPM. It is important to understand that the very high tip mass ratio may not be practical for actual industrial applications. The compromise between obtaining the best power output of the harvester without violating the practicality of the harvester will be studied in Section 6.6.

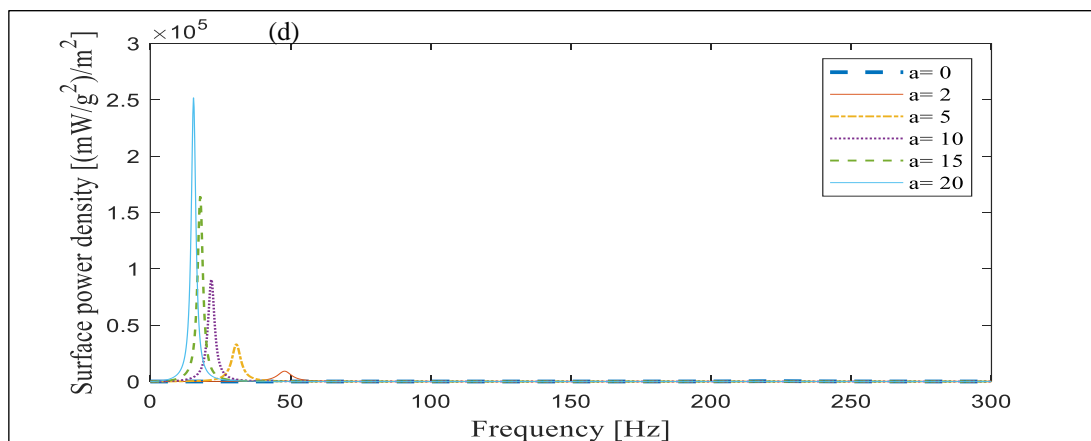
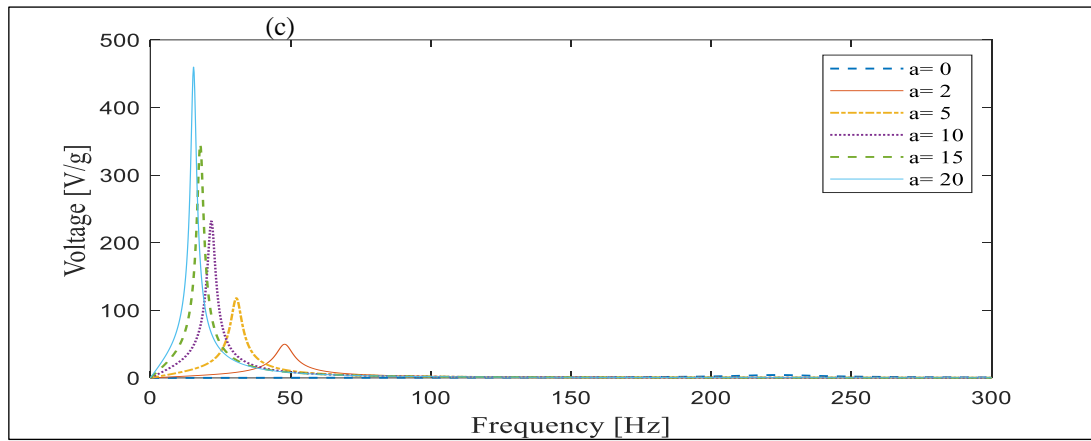
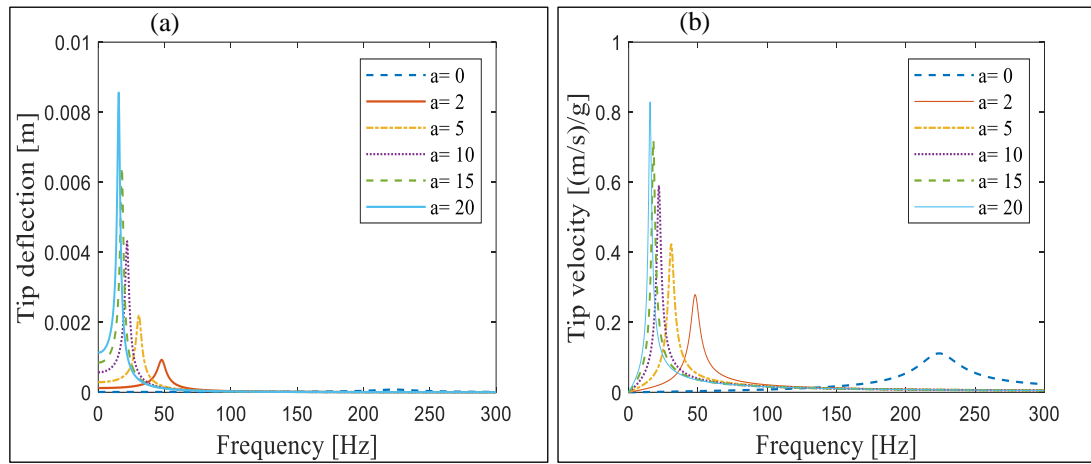


Figure 87: FRF of optimal design subjected to different tip mass ratios at  $R_{opt}$

### 6.5.3 Piezoelectric material effect

The effect of different piezoelectric materials on the performance of the harvester is investigated in this section. Table 17 lists the properties of three different piezoelectric materials PZT-5A, PZT-5H and PZT-5J. The rest of the geometrical and substrate properties are kept the same as in Table 12 except for the tip width which is determined based on the design optimization analysis done previously for an optimum design.

Table 17: Properties of different piezoelectric materials used in the parametric study [165]

Property	PZT-5A	PZT-5H	PZT-5J
Density $\rho_p$	7800	7800	7800
Young Modulus $E_p$	$52 \times 10^9$	$50 \times 10^9$	$51 \times 10^9$
Strain constant $d_{31}$	$-190 \times 10^{-12}$	$-320 \times 10^{-12}$	$-210 \times 10^{-12}$
Absolute permittivity $\epsilon_{33}^S$	$1800\epsilon_0$	$3800\epsilon_0$	$2100\epsilon_0$

Figure 88 shows the effect of three different piezoelectric materials on the voltage and surface power density of the harvester. Open circuit condition of load resistance  $470 \text{ k}\Omega$  is investigated. PZT-5A material gives the maximum voltage and surface power density of  $107.44 \text{ [V/g]}$  and  $1.46 \times 10^4 \text{ [(mW/g}^2\text{)/ m}^2\text{]}$  at resonance frequency of  $37.04 \text{ Hz}$ . PZT-5H has the lowest output of voltage  $100.46 \text{ [V/g]}$  and surface power density of  $1.28 \times 10^4 \text{ [(mW/g}^2\text{)/ m}^2\text{]}$  at resonance frequency of  $36.95 \text{ Hz}$ .

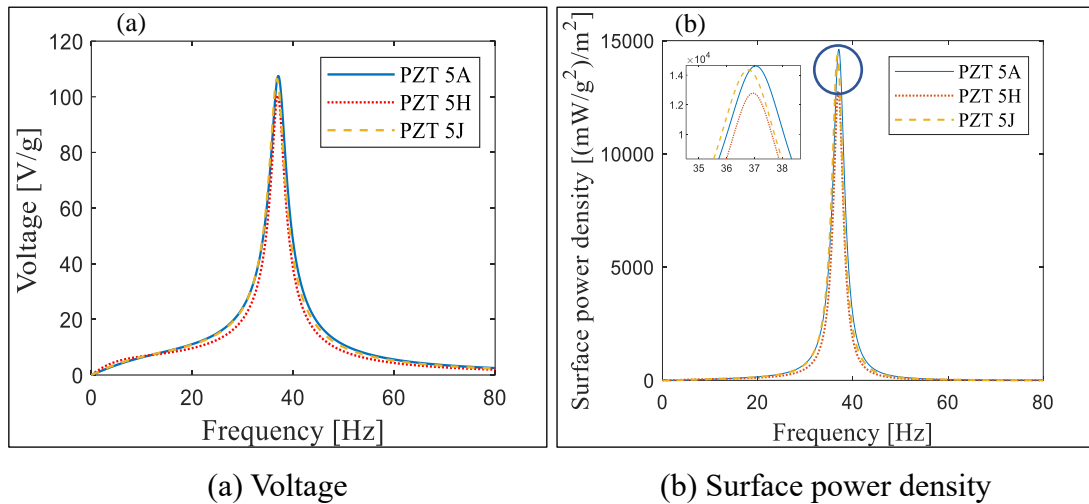


Figure 88: FRF of the optimal design for three different piezoelectric materials with tip mass  $M_t = 0.012$  at load resistance of  $470 \text{ k}\Omega$

In Figure 89, each piezoelectric material is studied at optimum load resistance  $R_{opt}$ . The maximum voltage shown in Figure 89(a) is for PZT-5A material at a value of  $68.03 \text{ [V/g]}$  for resonance frequency  $36.41 \text{ Hz}$ . However, the surface power density is the highest for PZT-5H material at a value of  $1.61 \times 10^4 \text{ [(mW/g}^2\text{)/m}^2\text{]}$  for resonance frequency  $35.99 \text{ Hz}$  and optimum load resistance of  $35 \text{ k}\Omega$ . The lowest surface power density is for PZT-5A at a value of  $1.58 \times 10^4 \text{ [(mW/g}^2\text{)/m}^2\text{]}$  at  $R_{opt} = 174 \text{ k}\Omega$ . The optimum resistance plays an important role in the power output of different piezoelectric materials. The power is inversely proportional with the load resistance ( $P_{avg} = \frac{|V_{rms}|}{R_{opt}}$ ). Table 17 shows that PZT-5H has the highest permittivity among the other materials. The permittivity affects the capacitance which by result affect the  $R_{opt}$  value. Thus, the surface power density at optimal load resistance gives an important insightful into the effect of different materials.

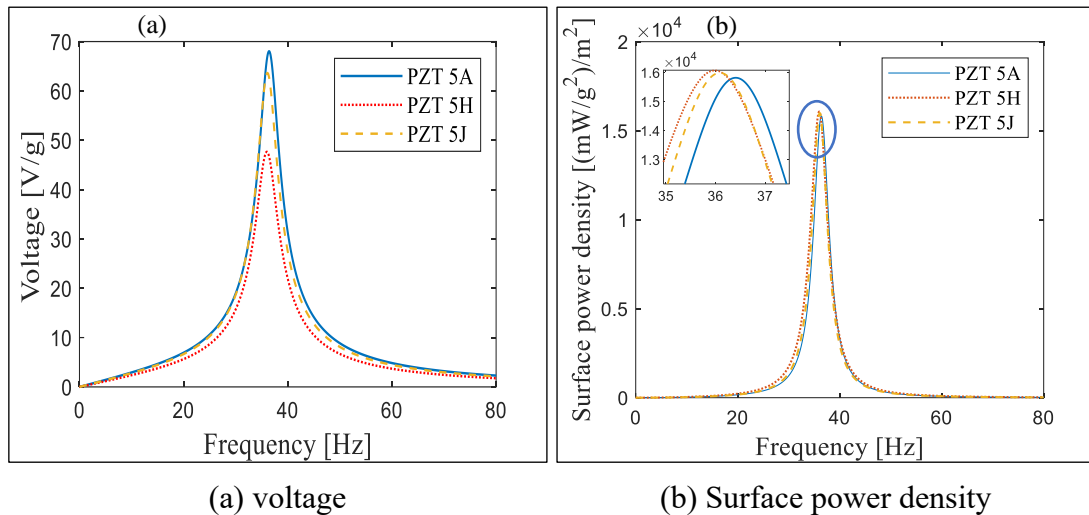


Figure 89: FRF of the optimal design of three different piezoelectric materials with tip mass  $M_t = 0.012$  at  $R_{opt}$

## 6.6 Design criteria and limitations of the optimal piezoelectric harvester

Design criteria are important to assess the performance of a novel piezoelectric harvesting system at different given conditions. This section presents a structured guideline to design an optimal piezoelectric cantilever harvester for a targeted application.

The following steps describe the process of designing an optimum piezoelectric cantilever for a given vibration source.

1. Identifying the vibration environment
  - Knowing the frequency and input excitation is the fundamental step to design a piezoelectric harvester. The following specifications are set for a practical study case:
    - i. Vibration source frequency 100 Hz
    - ii. Acceleration input excitation 1g
2. Applying the optimum ratios and parameters

- From the design optimization, all the optimum parameters should be applied for the best performance of the piezoelectric harvester as the following:

- i. Taper ratio ( $r = 0$ )
- ii. Thickness ratio ( $t_p = 0.7$ )
- iii. Middle section of  $l_m = 0.8 l$  and  $b_m = 0.2 b_0$
- iv. Optimum resistance load  $R_{opt} = 1 / (C_p W_n)$

### 3. Setting limitations

- There are important limitations that are added to the design process to ensure that the piezoelectric harvester design is practical and efficient.
  - i. Beam theory limitation ( $l/h_{tot} > 20$ )
  - ii. Tip mass ratio ( $a < 10$ )
  - iii. Stress limitation (Stress < tensile stress)
    1. Tensile stress for PZT-5A is 140.4 MPa
    2. Safety factor for brittle materials 2.5-3

### 4. Choosing the best aspect ratio

- Aspect ratio is defined as  $a_r = l/b_0$ .

In order to choose the best aspect ratio for the given case, Figure 90 presents the surface power densities of different aspect ratios for a given vibration source (100 Hz and 1g). A wide range of aspect ratios was tested from 0.1 up to 5 (this includes extreme conditions for understanding purposes). However, some of them violated the design criteria mentioned earlier. For very small aspect ratios ( $0.1 < a_r < 0.5$ ) the Euler-Bernoulli beam theory is violated and the stresses are high. Aspect ratios ranges of ( $0.5 < a_r < 0.9$ ) require very high tip mass ratios. Thus, the figure shows the

aspect ratios that conform to the given design specifications in a range of ( $0.9 < a_r < 2.7$ ). The plot illustrates that as the aspect ratio decreases the surface power density increases.

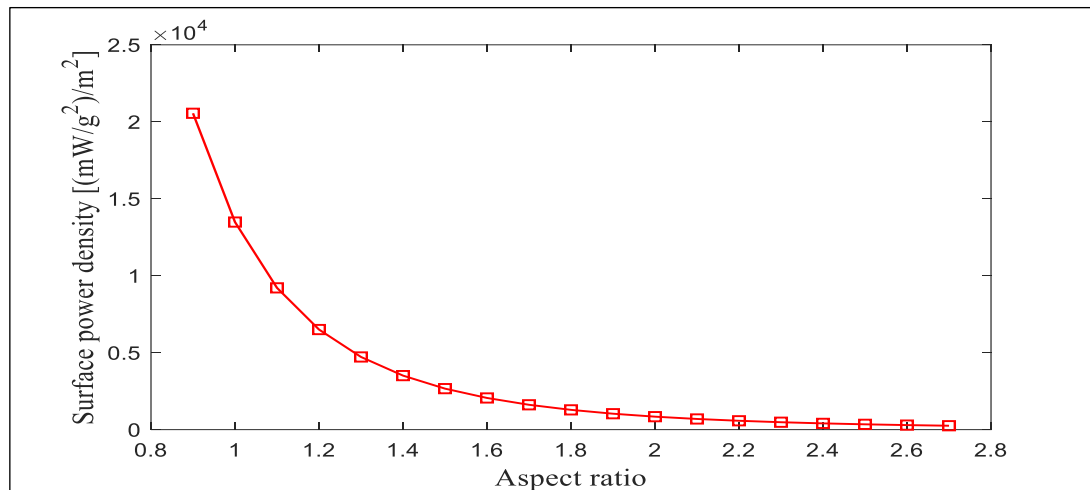


Figure 90: Surface power density for different aspect ratios of the optimal design for a given vibration source

However, in order to choose the most suitable aspect ratio, the dimension of the tip mass should be taken in consideration. The tip mass dimension is chosen based on the following (assuming the tip mass density is  $9000 \text{ kg/m}^3$ ):

Width=  $6.36 \times 10^{-3} \text{ m}$  (which is the width at the tip of the beam)

Length=  $0.2L \text{ m}$  (length depends on the selected aspect ratio)

Thickness= Tip mass volume/ tip mass area

Figure 91 shows the tip mass thickness for each aspect ratio ( $0.9 < a_r < 2.7$ ). The suitable and practical tip mass thickness is around 1 cm. Thus, the best aspect ratio for the optimal design is ( $a_r = 1.5$ ).

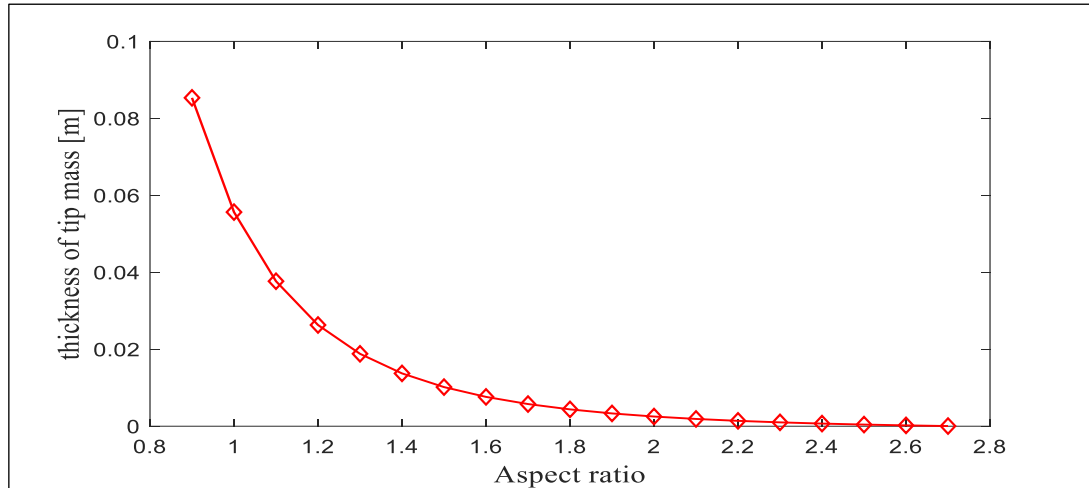


Figure 91: Tip mass thickness for different aspect ratios of the optimal design

Table 18 includes the specifications of the optimal piezoelectric harvester for a given environment (100 Hz and 1 g) under the discussed criteria and limitations. The material properties are the same as Table 12.

Table 18: Specification of the optimal piezoelectric harvester

Item	Symbol	Unit	Value
Beam length	$L$	$mm$	47.7
Beam width base	$b_0$	$mm$	31.8
Beam width tip	$b_l$	$mm$	6.36
Piezoelectric thickness	$h_p$	$mm$	0.26
Substrate thickness	$h_b$	$mm$	0.37
Tip mass	$M_t$	$kg$	0.0056
Tip mass density	$\rho_{m_t}$	$kg/m^3$	9000

Figure 92 presents the voltage and surface power density of an optimal piezoelectric cantilever with tip mass. The voltage output is 27.72 [V/g] and the surface power density is  $6.17 \times 10^3$  [(mW/g<sup>2</sup>)/ m<sup>2</sup>]. The stress and strain are displayed



in Figure 93. The maximum stress and strain are at the tip of the piezoelectric beam at a value of 5.1 MPa and  $5.59 \times 10^{-9}$  respectively.

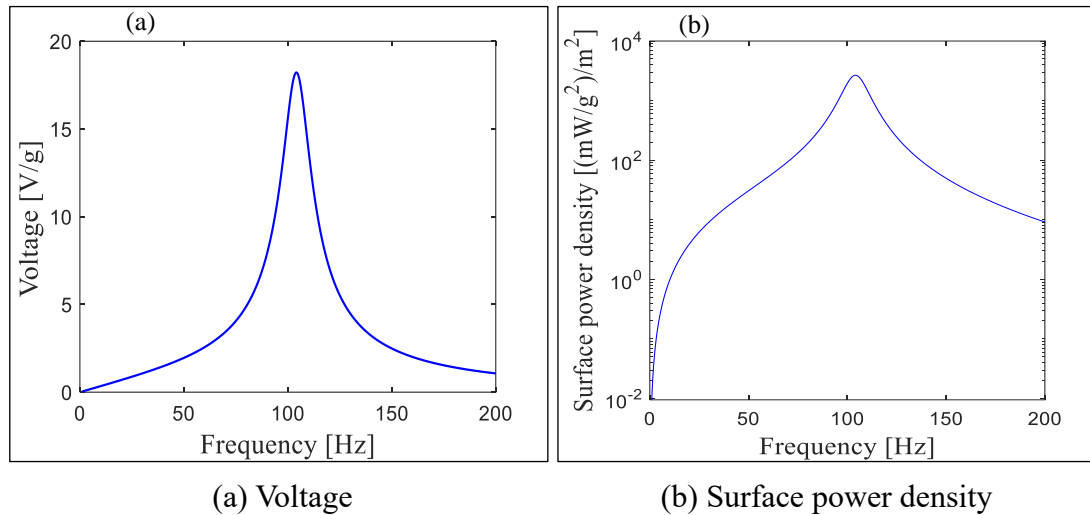


Figure 92: FRF of optimal piezoelectric harvester with tip mass  $M_t = 0.0056$  kg

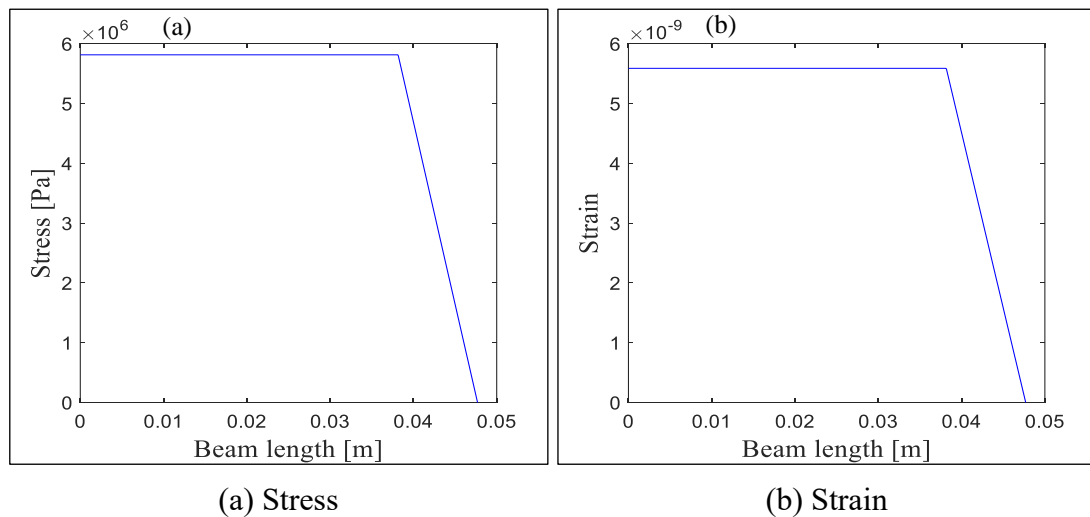


Figure 93: Stress and strain of the optimal piezoelectric harvester with tip mass  $M_t = 0.0056$  kg

The power output of an optimal design with the above specifications can produce about 0.5 W. This harvested energy can power various MEMS applications for a vibration source of 100 Hz and 1 g input excitation.

## Chapter 7: Conclusion and Recommendations

### 7.1 Conclusion

The main objective of the thesis is to design an optimum piezoelectric harvester system by conducting a comprehensive analysis of design modeling and optimization. A developed mathematical model of the LPM was presented to reach the optimal piezoelectric shape that can produce maximum power output for a specific volume. A derived dimensionless parameter was used as a key parameter in optimizing the optimal piezoelectric cantilever design. Experimental validation was carried for a bimorph (PZT-5H) rectangular cantilever beam as a preliminary verification to confirm the derivation process of the LPM. The experiment was done for the frequency range of 20- 400 Hz. The damping coefficient was measured experimentally as 0.011. For input excitation of 1 g pk-pk measured using the accelerometer, the experimental resonance frequency of the piezoelectric cantilever is 304.4 Hz. The analytical resonance frequency is 304.7 Hz. FRF of voltage and power were analyzed. The experimental and analytical voltages are 12.25 and 12.92 [V/g]. The error between the experiment and analytical voltage is 5.5%. Under open circuit conditions, the experimental power output of the rectangular piezoelectric cantilever is 0.0097 mW/g<sup>2</sup> while for analytical results is 0.01085 mW/g<sup>2</sup>.

The development of the design optimization in this thesis was based on the FEM. This approach was devised as an alternative method to overcome the complicated analytical solution of the DPM. Both mechanical and electromechanical models were developed using two FEM programs, Femap by Nastran and ANSYS workbench, respectively. Three types of validations were carried in this work to verify the use of FEM in mimicking the DPM. The validations are based on space and

frequency domains. The first type is the validation of FEM using beam deflection where FEM was developed in Femap by Nastran and two DPMs were tested. The first DPM is a rectangular piezoelectric cantilever beam with different tip mass ratios. The second DPM is a tapered piezoelectric beam with no tip mass. The second type of validation was performed using the relative tip displacement transmissibility function. The FEM was validated with the analytical model of a rectangular piezoelectric harvester taken from the literature. The third type of validation was for the integrated piezoelectric cantilever FEM. In this study, electromechanical characteristics of the piezoelectric material were embedded in the model. The FEM was developed using ANSYS workbench with PIEZO and MEMS extension. The validation was done with the DPM and some experimental results of a rectangular piezoelectric beam with tip mass which were developed earlier by the literature. The results of the three validations gave credibility to the FEM to be used as a baseline in developing the optimal piezoelectric cantilever beam.

Design optimization analysis was then carried in Chapter 6 to reach the optimum piezoelectric cantilever shape that harvests the maximum power output. The Power Factor parameter was developed and used in this process to understand the effect of taper ratio and thickness ratio on the performance of piezoelectric harvesters. The power factor showed an optimum performance at a taper ratio of ( $r = 0$ ) taking the full length of the cantilever, middle section of ( $l_m = 0.8 l$ ,  $b_m = 0.2 b_0$ ) and thickness ratio of ( $t_p = 0.7$ ). Furthermore, the normalized stress distribution of the developed optimal design was compared to other known shapes (rectangular and taper). The study confirmed that the optimal design has a great stress distribution along the beam's length. One of the primary objectives of this thesis was to model the

optimal piezoelectric cantilever beam using LPM and understand the vibration behavior of the harvester. In order to understand the limitations of the LPM, the accuracy of the LPM of a linearly tapered piezoelectric beam and the optimal design were investigated since the literature lacked any studies on tapered configurations. The study used the deflection error percentage in understanding the accuracy of the LPM and explored the effect of the tip mass ratios as well. Results highlighted that as the taper ratio decreases from  $r = 1$  to  $r = 0$ , the deflection percentage error increases to reach up to 9% for no tip mass case. For the optimized shape, the deflection error has reached 7%. Adding a tip mass affirmed that the error decreases to less than 0.5% when the tip mass ratio “ $a$ ” is larger than 2. Extended studies on the accuracy of LPM were conducted using the relative tip displacement transmissibility function. Results showed that as the taper ratio decreases towards zero (triangular shape), the relative percentage error of using the LPM to predict the vibration response increased significantly to 55%. Therefore, correction factors of linearly tapered piezoelectric cantilevers including the optimal design subjected to different tip mass ratios were developed. The developed correction factor for the optimal piezoelectric cantilever beam when no tip mass is  $CF = 1.95162$ . Comparisons between C-LPM and FEM for different linearly tapered piezoelectric beams including the optimal design were tested for voltage and surface power density. The maximum error between the C-LPM and FEM for voltage was around 2%, whereas for the surface power density it was 4%. The error between the C-LPM and the FEM might be from the meshing limitation of the FEM due to the student version program usage.

Moreover, results showed that as the taper ratio decreases from rectangular to the optimal design, the surface power density increases significantly. The developed

optimal design has shown significant growth in voltage and surface power density. The voltage of the optimal design is higher than the known rectangular shape by 10%. The surface power density of the optimal design exhibits a striking increase of 58% higher than the rectangular shape. A parametric study was done to understand the effect of other parameters on the optimal design. The impact of different load resistances was first scrutinized. The optimum resistances for two extreme conditions of short and open circuits excitation frequencies were studied. Peak power and surface power density of an optimal design with an optimum load resistance were then stated. The second parametric study investigated the effect of different tip mass ratios. The increase in the tip mass ratio led to a significant increase in the surface power density. Moreover, piezoelectric cantilevers with big mass ratios have small resonance frequencies, making them suitable for different MEMS applications. The third parametric studied the performance of different types of piezoelectric materials (PZT-5A, PZT-5H and PZT-5J). Finally, a complete structured process was built to design the best piezoelectric harvester for any vibration source. For 100 Hz input excitation frequency and 1 g input acceleration, the optimal design with aspect ratio 1.5 and tip mass 0.0056 kg gave a surface power density of  $6.17 \times 10^3$  [(mW/g<sup>2</sup>)/ m<sup>2</sup>] and a voltage of 27.72 [V/g] at optimum load resistance of 79 k $\Omega$ .

## **7.2 Recommendations for future research**

The developed research on optimum piezoelectric cantilever harvester can be further improved through the following recommendations:

- Analytical development of a correction factor for linearly tapered piezoelectric cantilevers using DPM to validate the FE correction factor.

- Experimental analysis for different tapered piezoelectric harvesters designs under different electric circuit conditions.
- A comprehensive analysis that includes different type of electric circuits and their effects on the optimum piezoelectric harvester.
- Development of the optimum piezoelectric harvester in off-frequency conditions.

## References

- [1] “World Power consumption | Electricity consumption | Enerdata.”  
<https://yearbook.enerdata.net/electricity/electricity-domestic-consumption-data.html> (accessed Mar. 25, 2020).
- [2] “Renewables in Electricity Production | Statistics Map by Region | Enerdata.”  
<https://yearbook.enerdata.net/renewables/renewable-in-electricity-production-share.html> (accessed Mar. 25, 2020).
- [3] M. H. Ahmadi *et al.*, “Renewable Energy Harvesting with the Application of Nanotechnology: A review,” *Int. J. Energy Res.*, vol. 43, no. 4, pp. 1387–1410, 2019, doi: 10.1002/er.4282.
- [4] F. Narita and M. Fox, “A Review on Piezoelectric, Magnetostrictive, and Magnetoelectric Materials and Device Technologies for Energy Harvesting Applications,” *Adv. Eng. Mater.*, vol. 20, no. 5, p. 1700743, 2018, doi: 10.1002/adem.201700743.
- [5] S. Roundy and P. K. Wright, “A Piezoelectric Vibration Based Generator for Wireless Electronics,” *Smart Mater. Struct.*, vol. 13, no. 5, pp. 1131–1142, Oct. 2004, doi: 10.1088/0964-1726/13/5/018.
- [6] S. R. Anton and H. A. Sodano, “A Review of Power Harvesting Using Piezoelectric Materials (2003–2006),” *Smart Mater. Struct.*, vol. 16, no. 3, pp. R1–R21, Jun. 2007, doi: 10.1088/0964-1726/16/3/R01.
- [7] H. Li, C. Tian, and Z. D. Deng, “Energy Harvesting from Low Frequency Applications Using Piezoelectric Materials,” *Appl. Phys. Rev.*, vol. 1, no. 4, p. 041301, 2014, doi: 10.1063/1.4900845.

- [8] Z. Yang, S. Zhou, J. Zu, and D. Inman, “High-Performance Piezoelectric Energy Harvesters and Their Applications,” *Joule*, vol. 2, no. 4, pp. 642–697, 2018, doi: 10.1016/j.joule.2018.03.011.
- [9] N. E. Dutoit, B. L. Wardle, and S.-G. Kim, “Design Considerations for MEMS-Scale Piezoelectric Mechanical Vibration Energy Harvesters,” *Integr. Ferroelectr.*, vol. 71, no. 1, pp. 121–160, 2005, doi: 10.1080/10584580590964574.
- [10] N. G. Stephen, “On Energy Harvesting from Ambient Vibration,” *J. Sound Vib.*, vol. 293, no. 1–2, pp. 409–425, 2006.
- [11] A. Erturk and D. J. Inman, “On Mechanical Modeling of Cantilevered Piezoelectric Vibration Energy Harvesters,” *J. Intell. Mater. Syst. Struct.*, vol. 19, no. 11, pp. 1311–1325, Nov. 2008, doi: 10.1177/1045389X07085639.
- [12] H. A. Sodano, G. Park, and D. J. Inman, “Estimation of Electric Charge Output for Piezoelectric Energy Harvesting,” *Strain*, vol. 40, no. 2, pp. 49–58, 2004, doi: 10.1111/j.1475-1305.2004.00120.x.
- [13] N. E. duToit and B. L. Wardle, “Experimental Verification of Models for Microfabricated Piezoelectric Vibration Energy Harvesters,” *AIAA J.*, vol. 45, no. 5, pp. 1126–1137, May 2007, doi: 10.2514/1.25047.
- [14] F. Lu, H. P. Lee, and S. P. Lim, “Modeling and Analysis of Micro Piezoelectric Power Generators for Micro-electromechanical-systems Applications,” *Smart Mater. Struct.*, vol. 13, no. 1, pp. 57–63, Nov. 2003, doi: 10.1088/0964-1726/13/1/007.
- [15] S.-N. Chen, G.-J. Wang, and M.-C. Chien, “Analytical Modeling of Piezoelectric Vibration-induced Micro Power Generator,” *Mechatronics*, vol. 16, no. 7, pp. 379–387, Sep. 2006, doi: 10.1016/j.mechatronics.2006.03.003.



- [16] J. Ajitsaria, S. Y. Choe, D. Shen, and D. J. Kim, "Modeling and Analysis of a Bimorph Piezoelectric Cantilever Beam for Voltage Generation," *Smart Mater. Struct.*, vol. 16, no. 2, pp. 447–454, Feb. 2007, doi: 10.1088/0964-1726/16/2/024.
- [17] A. Erturk and D. J. Inman, "Issues in Mathematical Modeling of Piezoelectric Energy Harvesters," *Smart Mater. Struct.*, vol. 17, no. 6, p. 065016, 2008, doi: 10.1088/0964-1726/17/6/065016.
- [18] A. Erturk and D. J. Inman, "A Distributed Parameter Electromechanical Model for Cantilevered Piezoelectric Energy Harvesters," *J. Vib. Acoust.*, vol. 130, no. 4, p. 041002, Jun. 2008, doi: 10.1115/1.2890402.
- [19] A. Erturk and D. J. Inman, "An Experimentally Validated Bimorph Cantilever Model for Piezoelectric Energy Harvesting from Base Excitations," *Smart Mater. Struct.*, vol. 18, no. 2, p. 025009, 2009, doi: 10.1088/0964-1726/18/2/025009.
- [20] C. R. Bowen, H. A. Kim, P. M. Weaver, and S. Dunn, "Piezoelectric and Ferroelectric Materials and Structures for Energy Harvesting Applications," *Energy Env. Sci*, vol. 7, no. 1, pp. 25–44, 2014, doi: 10.1039/C3EE42454E.
- [21] K. S. Ramadan, D. Sameoto, and S. Evoy, "A Review of Piezoelectric Polymers as Functional Materials for Electromechanical Transducers," *Smart Mater. Struct.*, vol. 23, no. 3, p. 033001, Jan. 2014, doi: 10.1088/0964-1726/23/3/033001.
- [22] A. Khan, Z. Abas, H. Soo Kim, and I.-K. Oh, "Piezoelectric Thin Films: an Integrated Review of Transducers and Energy Harvesting," *Smart Mater. Struct.*, vol. 25, no. 5, p. 053002, May 2016, doi: 10.1088/0964-1726/25/5/053002.

- [23] D. Guyomar and M. Lallart, "Recent Progress in Piezoelectric Conversion and Energy Harvesting Using Nonlinear Electronic Interfaces and Issues in Small Scale Implementation," *Micromachines*, vol. 2, no. 2, pp. 274–294, Jun. 2011, doi: 10.3390/mi2020274.
- [24] J. Dicken, P. D. Mitcheson, I. Stoianov, and E. M. Yeatman, "Power-Extraction Circuits for Piezoelectric Energy Harvesters in Miniature and Low-Power Applications," *IEEE Trans. Power Electron.*, vol. 27, no. 11, pp. 4514–4529, Nov. 2012, doi: 10.1109/TPEL.2012.2192291.
- [25] G. D. Szarka, B. H. Stark, and S. G. Burrow, "Review of Power Conditioning for Kinetic Energy Harvesting Systems," *IEEE Trans. Power Electron.*, vol. 27, no. 2, pp. 803–815, 2012, doi: 10.1109/TPEL.2011.2161675.
- [26] J. A. Brans, T. W. A. Blad, and N. Tolou, "A review of design principles for improved mechanical reliability of cantilever piezoelectric vibration energy harvesters," in *2019 7th International Conference on Control, Mechatronics and Automation (ICCMA)*, Delft, Netherlands, Nov. 2019, pp. 408–415, doi: 10.1109/ICCMA46720.2019.8988762.
- [27] S. Sojan and R. K. Kulkarni, "A Comprehensive Review of Energy Harvesting Techniques and its Potential Applications," *Int. J. Comput. Appl.*, vol. 139, no. 3, pp. 14–19, 2016.
- [28] S. Kim *et al.*, "Ambient RF Energy-Harvesting Technologies for Self-Sustainable Standalone Wireless Sensor Platforms," *Proc. IEEE*, vol. 102, no. 11, pp. 1649–1666, Nov. 2014, doi: 10.1109/JPROC.2014.2357031.
- [29] M. A. Pillai and E. Deenadayalan, "A Review of Acoustic Energy Harvesting," *Int. J. Precis. Eng. Manuf.*, vol. 15, no. 5, pp. 949–965, May 2014, doi: 10.1007/s12541-014-0422-x.

- [30] R. Ahmed, F. Mir, and S. Banerjee, "A Review on Energy Harvesting Approaches for Renewable Energies from Ambient Vibrations and Acoustic Waves using Piezoelectricity," *Smart Mater. Struct.*, vol. 26, no. 8, p. 085031, Jul. 2017, doi: 10.1088/1361-665X/aa7bfb.
- [31] M. Yuan, Z. Cao, J. Luo, and X. Chou, "Recent Developments of Acoustic Energy Harvesting: A Review," *Micromachines*, vol. 10, no. 1, p. 48, Jan. 2019, doi: 10.3390/mi10010048.
- [32] S.-G. Kim, S. Priya, and I. Kanno, "K. V. A. K. Srikanth, 'State of art: Piezoelectric Vibration Energy Harvesters,' *Mater. Today Proc.*, vol. 4, no. 2, pp. 1091–1098, 2017, doi: <https://doi.org/10.1016/j.matpr.2017.01.124>.
- [33] F. Yildiz, "Potential Ambient Energy-Harvesting Sources and Techniques.," *J. Technol. Stud.*, vol. 35, no. 1, pp. 40–48, 2009.
- [34] H. Xiao and X. Wang, "A Review of Piezoelectric Vibration Energy Harvesting Techniques," *Int. Rev. Mech. Eng.*, vol. 8, no. 3, pp. 139–150, 2014.
- [35] S. Cao and J. Li, "A Survey on Ambient Energy Sources and Harvesting Methods for Structural Health Monitoring Applications," *Adv. Mech. Eng.*, vol. 9, no. 4, pp. 1-14, 2017, doi: 10.1177/1687814017696210.
- [36] S. Wang and S. Wang, "Impacts of Wind Energy on Environment: A Review," *Renew. Sustain. Energy Rev.*, vol. 49, pp. 437–443, Sep. 2015, doi: 10.1016/j.rser.2015.04.137.
- [37] Y. Bai, H. Jantunen, and J. Juuti, "Energy Harvesting Research: The Road from Single Source to Multisource," *Adv. Mater.*, vol. 30, no. 34, p. 1707271, 2018, doi: 10.1002/adma.201707271.

- [38] M. Safaei, H. A. Sodano, and S. R. Anton, “A Review of Energy Harvesting Using Piezoelectric Materials: State-of-the-Art a Decade Later (2008–2018),” *Smart Mater. Struct.*, vol. 28, no. 11, p. 113001, 2019, doi:10.1088/1361-665x/ab36e4.
- [39] B. Edwards, P. A. Hu, and K. C. Aw, “Validation of a Hybrid Electromagnetic–Piezoelectric Vibration Energy Harvester,” *Smart Mater. Struct.*, vol. 25, no. 5, p. 055019, 2016, doi: 10.1088/0964-1726/25/5/055019.
- [40] A. R. M. Siddique, S. Mahmud, and B. Van Heyst, “A Comprehensive Review on Vibration Based Micro Power Generators using Electromagnetic and Piezoelectric Transducer Mechanisms,” *Energy Convers. Manag.*, vol. 106, pp. 728–747, 2015.
- [41] P. Li, S. Gao, and H. Cai, “Modeling and Analysis of Hybrid Piezoelectric and Electromagnetic Energy Harvesting from Random Vibrations,” *Microsyst. Technol.*, vol. 21, no. 2, pp. 401–414, Feb. 2015, doi: 10.1007/s00542-013-2030-6.
- [42] D. P. Arnold, “Review of Microscale Magnetic Power Generation,” *IEEE Trans. Magn.*, vol. 43, no. 11, pp. 3940–3951, 2007.
- [43] Y. Huang, “Packaging and connecting electrostatic transducer arrays,” U.S. Patent No. 8,815,653. Aug. 26, 2014.
- [44] V. Dorzhiev, A. Karami, P. Basset, F. Marty, V. Dragunov, and D. Galayko, “Electret-Free Micromachined Silicon Electrostatic Vibration Energy Harvester with the Bennet’s Doubler as Conditioning Circuit,” *IEEE Electron Device Lett.*, vol. 36, no. 2, pp. 183–185, 2015.

- [45] S. P. Beeby, M. J. Tudor, and N. M. White, “Energy Harvesting Vibration Sources for Microsystems Applications,” *Meas. Sci. Technol.*, vol. 17, no. 12, p. R175, 2006, doi: 10.1088/0957-0233/17/12/R01.
- [46] E. Halvorsen *et al.*, “An electrostatic energy harvester with electret bias,” in *TRANSDUCERS 2009-2009 International Solid-State Sensors, Actuators and Microsystems Conference*, 2009, pp. 1381–1384.
- [47] Y. Zhang, T. Wang, A. Luo, Y. Hu, X. Li, and F. Wang, “Micro Electrostatic Energy Harvester with Both Broad Bandwidth and High Normalized Power Density,” *Appl. Energy*, vol. 212, no. FEB.15, pp. 362–371, 2018, doi: 10.1016/j.apenergy.2017.12.053.
- [48] L. Wang and F. G. Yuan, “Vibration Energy Harvesting by Magnetostrictive Material,” *Smart Mater. Struct.*, vol. 17, no. 4, p. 045009, 2008, doi: 10.1088/0964-1726/17/4/045009.
- [49] H. Jafari, A. Ghodsi, S. Azizi, and M. R. Ghazavi, “Energy Harvesting Based on Magnetostriction, for Low Frequency Excitations,” *Energy*, vol. 124, pp. 1–8, Apr. 2017, doi: 10.1016/j.energy.2017.02.014.
- [50] S. Saadon and O. Sidek, “A Review of Vibration-Based MEMS Piezoelectric Energy Harvesters,” *Energy Convers. Manag.*, vol. 52, no. 1, pp. 500–504, Jan. 2011, doi: 10.1016/j.enconman.2010.07.024.
- [51] R. Calìò *et al.*, “Piezoelectric Energy Harvesting Solutions,” *Sensors*, vol. 14, no. 3, pp. 4755–4790, 2014, doi: 10.3390/s140304755.

- [52] M. R. Sarker, S. Julai, M. F. M. Sabri, S. M. Said, Md. M. Islam, and M. Tahir, "Review of Piezoelectric Energy Harvesting System and Application of Optimization Techniques to Enhance the Performance of the Harvesting System," *Sens. Actuators Phys.*, vol. 300, p. 111634, Dec. 2019, doi: 10.1016/j.sna.2019.111634.
- [53] H. Liu, J. Zhong, C. Lee, S.-W. Lee, and L. Lin, "A Comprehensive Review on Piezoelectric Energy Harvesting Technology: Materials, Mechanisms, and Applications," *Appl. Phys. Rev.*, vol. 5, no. 4, p. 041306, Dec. 2018, doi: 10.1063/1.5074184.
- [54] M. Staworko and T. Uhl, "Modeling and Simulation of Piezoelectric Elements- Comparison of Available Methods and Tools," *Mech. AGH Univ. Sci. Technol.*, vol. 27, no. 4, pp. 161–171, 2008.
- [55] M. Matak and P. Šolek, "Harvesting the Vibration Energy," *Am. J. Mech. Eng.*, vol. 1, no. 7, pp. 438–442, 2013, doi: 10.12691/ajme-1-7-57.
- [56] J. Kaleta, D. Lewandowski, P. Wiewiórski, R. Mech, and K. Kot, "Application of smart materials in energy recovery; Energy harvesting," presented in Wrocław University of Technology, ul. Smoluchowskiego 25, 50-370 Wrocław, Sept. 3, 2013 [*PowerPoint* slides]. Available: <https://kmim.wm.pwr.edu.pl/ssofm/wp-content/uploads/sites/31/2014/09/lsmpl3a07.pdf>, Accessed on: Dec. 8, 2017
- [57] E. Saoutieff, M. Allain, Y.-R. Nowicki-Bringuier, A. Viana, and E. Pauliac-Vaujour, "Integration of Piezoelectric Nanowires Matrix onto a Microelectronics Chip," *Procedia Eng.*, vol. 168, pp. 1638–1641, 2016.
- [58] M. T. Todaro *et al.*, "Piezoelectric MEMS Vibrational Energy Harvesters: Advances and Outlook," *Microelectron. Eng.*, vol. 183–184, pp. 23–36, Nov. 2017, doi: 10.1016/j.mee.2017.10.005.

- [59] T.-C. Yuan, J. Yang, and L.-Q. Chen, “Nonlinear Dynamics of a Circular Piezoelectric Plate for Vibratory Energy Harvesting,” *Commun. Nonlinear Sci. Numer. Simul.*, vol. 59, pp. 651–656, Jun. 2018, doi: 10.1016/j.cnsns.2017.12.010.
- [60] J. Li *et al.*, “Large Electro-Optic Response of Bulk Ferroelectric Crystals Enhanced by Piezoelectric Resonance in the High Frequency Range,” *Mater. Res. Bull.*, vol. 97, pp. 523–529, Jan. 2018, doi: 10.1016/j.materresbull.2017.09.020.
- [61] G. Wang, W.-H. Liao, B. Yang, X. Wang, W. Xu, and X. Li, “Dynamic and Energetic Characteristics of a Bistable Piezoelectric Vibration Energy Harvester with an Elastic Magnifier,” *Mech. Syst. Signal Process.*, vol. 105, pp. 427–446, May 2018, doi: 10.1016/j.ymsp.2017.12.025.
- [62] K. V. Allamraju K.Srikanth, “State of Art: Piezoelectric Vibration Energy Harvesters,” *Mater. Today Proc.*, vol. 4, no. 2, Part A, pp. 1091–1098, Jan. 2017, doi: 10.1016/j.matpr.2017.01.124.
- [63] S. M. Taware and S. P. Deshmukh, “A Review of Energy Harvesting from Piezoelectric Materials,” *IOSR J. Mech. Civ. Eng. IOSR-JMCE*, pp. 43–50, 2013.
- [64] W. Tian, Z. Ling, W. Yu, and J. Shi, “A Review of MEMS Scale Piezoelectric Energy Harvester,” *Appl. Sci.*, vol. 8, no. 4, p. 645, 2018, doi: 10.3390/app8040645.
- [65] S. Chandrasekaran *et al.*, “Micro-Scale to Nano-Scale Generators for Energy Harvesting: Self Powered Piezoelectric, Triboelectric and Hybrid Devices,” *Phys. Rep.*, vol. 792, pp. 1–33, 2019, doi: 10.1016/j.physrep.2018.11.001.

- [66] H. Liu, J. Zhong, C. Lee, S.-W. Lee, and L. Lin, "Energy Harvester Array using Piezoelectric Circular Diaphragm for Rail Vibration," *Appl. Phys. Rev.*, vol. 5, no. 4, p. 041306, 2018, doi: <https://doi.org/10.1063/1.5074184>.
- [67] S. Priya *et al.*, "A Review on Piezoelectric Energy Harvesting: Materials, Methods, and Circuits," *Energy Harvest. Syst. Berl.*, vol. 4, no. 1, pp. 3–39, 2017, doi: <http://dx.doi.org.uaeu.idm.oclc.org/10.1515/ehs-2016-0028>.
- [68] T. Starner and J. A. Paradiso, "Human Generated Power for Mobile Electronics," *Low-Power Electron. Des.*, vol. 45, pp. 1–35, 2004.
- [69] R. Sood, Y. B. Jeon, J. H. Jeong, and S. G. Kim, "Piezoelectric micro power generator for energy harvesting." Technical Digest of the 2004 Solid-State Sensor and Actuator Workshop, Hilton Head, South Carolina 2004.
- [70] N. Chidambaram, A. Mazzalai, and P. Murali, "Measurement of Effective Piezoelectric Coefficients of PZT thin Films for Energy Harvesting Application with Interdigitated Electrodes," *IEEE Trans. Ultrason. Ferroelectr. Freq. Control*, vol. 59, no. 8, pp. 1624–1631, 2012.
- [71] S.-B. Kim, H. Park, S.-H. Kim, H. C. Wickle, J.-H. Park, and D.-J. Kim, "Comparison of MEMS PZT Cantilevers Based on d31 and d33 Modes for Vibration Energy Harvesting," *J. Microelectromechanical Syst.*, vol. 22, no. 1, pp. 26–33, 2012.
- [72] J. Zhao *et al.*, "Investigation of a d15 Mode PZT-51 Piezoelectric Energy Harvester with a Series Connection Structure," *Smart Mater. Struct.*, vol. 21, no. 10, p. 105006, 2012, doi: [10.1088/0964-1726/21/10/105006](https://doi.org/10.1088/0964-1726/21/10/105006).
- [73] D.-A. Wang and N.-Z. Liu, "A Shear Mode Piezoelectric Energy Harvester Based on a Pressurized Water Flow," *Sens. Actuators Phys.*, vol. 2, no. 167, pp. 449–458, 2011, doi: [10.1016/j.sna.2011.03.003](https://doi.org/10.1016/j.sna.2011.03.003).



- [74] C. Majidi, M. Haataja, and D. J. Srolovitz, "Analysis and Design Principles for Shear-Mode Piezoelectric Energy Harvesting with ZnO Nanoribbons," *Smart Mater. Struct.*, vol. 19, no. 5, p. 055027, 2010, doi: 10.1088/0964-1726/19/5/055027.
- [75] H. S. Kim, J.-H. Kim, and J. Kim, "A Review of Piezoelectric Energy Harvesting Based on Vibration," *Int. J. Precis. Eng. Manuf.*, vol. 12, no. 6, pp. 1129–1141, 2011.
- [76] A. Badel, A. Benayad, E. Lefeuvre, L. Lebrun, C. Richard, and D. Guyomar, "Single Crystals and Nonlinear Process for Outstanding Vibration-Powered Electrical Generators," *IEEE Trans. Ultrason. Ferroelectr. Freq. Control*, vol. 53, no. 4, pp. 673–684, 2006.
- [77] C. Mo, L. J. Radziemski, and W. W. Clark, "Analysis of PMN-PT and PZT Circular Diaphragm Energy Harvesters for Use in Implantable Medical Devices," in *Active and Passive Smart Structures and Integrated Systems 2007*, 2007, vol. 6525, p. 652507, doi: 10.1117/12.716663.
- [78] Z. Yang and J. Zu, "Comparison of PZN-PT, PMN-PT Single Crystals and PZT Ceramic for Vibration Energy Harvesting," *Energy Convers. Manag.*, vol. 122, pp. 321–329, 2016.
- [79] X. Wang and F. Jin, "Investigation of properties of PIN-PMN-PT single crystal and its high performance application for a piezoelectric energy harvester," in *2017 Symposium on Piezoelectricity, Acoustic Waves, and Device Applications (SPAWDA)*, 2017, pp. 514–518.

- [80] C.-T. Pan *et al.*, “Significant Piezoelectric and Energy Harvesting Enhancement of Poly (Vinylidene Fluoride)/ Polypeptide Fiber Composites Prepared Through Near-Field Electrospinning,” *J. Mater. Chem. A*, vol. 3, no. 13, pp. 6835–6843, 2015, doi: 10.1039/C5TA00147A.
- [81] S. Harstad *et al.*, “Enhancement of  $\beta$ -phase in PVDF Films Embedded with Ferromagnetic Gd<sub>5</sub>Si<sub>4</sub> Nanoparticles for Piezoelectric Energy Harvesting,” *AIP Adv.*, vol. 7, no. 5, p. 056411, May 2017, doi: 10.1063/1.4973596.
- [82] Y. Hu, L. Lin, Y. Zhang, and Z. L. Wang, “Replacing a Battery by a Nanogenerator with 20 V Output,” *Adv. Mater.*, vol. 24, no. 1, pp. 110–114, 2012, doi: 10.1002/adma.201103727.
- [83] D. L. Churchill, M. J. Hamel, C. P. Townsend, and S. W. Arms, “Strain Energy Harvesting for Wireless Sensor Networks,” in *Smart Structures and Materials 2003: Smart Electronics, MEMS, BioMEMS, and Nanotechnology*, Jul. 2003, vol. 5055, pp. 319–327, doi: 10.1117/12.483591.
- [84] X. Gao, W.-H. Shih, and W. Y. Shih, “Vibration Energy Harvesting using Piezoelectric Unimorph Cantilevers with Unequal Piezoelectric and Nonpiezoelectric Lengths,” *Appl. Phys. Lett.*, vol. 97, no. 23, p. 233503, Dec. 2010, doi: 10.1063/1.3521389.
- [85] A. Jemai, F. Najar, and M. Chafra, “Parametric Analysis of Multilayered Unimorph Piezoelectric Vibration Energy Harvesters,” *J. Vib. Control*, vol. 23, no. 15, pp. 2538–2553, Aug. 2017, doi: 10.1177/1077546315617870.
- [86] M. Han, Y. C. Chan, W. Liu, S. Zhang, and H. Zhang, “Low frequency PVDF piezoelectric energy harvester with combined d<sub>31</sub> and d<sub>33</sub> operating modes,” in *The 8th Annual IEEE International Conference on Nano/Micro Engineered and Molecular Systems*, 2013, pp. 440–443.

- [87] R. Hosseini and M. Hamed, "Improvements in Energy Harvesting Capabilities by using Different Shapes of Piezoelectric Bimorphs," *J. Micromechanics Microengineering*, vol. 25, no. 12, p. 125008, 2015, doi: 10.1088/0960-1317/25/12/125008.
- [88] F. Goldschmidtboeing and P. Woias, "Characterization of Different Beam Shapes for Piezoelectric Energy Harvesting," *J. Micromechanics Microengineering*, vol. 18, no. 10, p. 104013, 2008, doi: 10.1088/0960-1317/18/10/104013.
- [89] H. Kim, S. Priya, and K. Uchino, "Modeling of Piezoelectric Energy Harvesting Using Cymbal Transducers," *Jpn. J. Appl. Phys.*, vol. 45, no. 7R, p. 5836, Jul. 2006, doi: 10.1143/JJAP.45.5836.
- [90] B. Ren, S. W. Or, X. Zhao, and H. Luo, "Energy Harvesting Using a Modified Rectangular Cymbal Transducer Based on 0.71 Pb (Mg 1/3 Nb 2/3) O 3–0.29 PbTiO 3 single crystal," *J. Appl. Phys.*, vol. 107, no. 3, p. 034501, 2010, doi:10.1063/1.3296156.
- [91] J. Palosaari, M. Leinonen, J. Hannu, J. Juuti, and H. Jantunen, "Energy Harvesting with a Cymbal Type Piezoelectric Transducer from Low Frequency Compression," *J. Electroceramics*, vol. 28, no. 4, pp. 214–219, 2012.
- [92] C. Mo, D. Arnold, W. C. Kinsel, and W. W. Clark, "Modeling and Experimental Validation of Unimorph Piezoelectric Cymbal Design in Energy Harvesting," *J. Intell. Mater. Syst. Struct.*, vol. 24, no. 7, pp. 828–836, May 2013, doi: 10.1177/1045389X12463459.
- [93] M. Leinonen, J. Palosaari, J. Juuti, and H. Jantunen, "Combined Electrical and Electromechanical Simulations of a Piezoelectric Cymbal Harvester for Energy Harvesting from Walking," *J. Intell. Mater. Syst. Struct.*, vol. 25, no. 4, pp. 391–400, 2014.

- [94] Y. Kuang, A. Daniels, and M. Zhu, “A Sandwiched Piezoelectric Transducer with Flex End-Caps for Energy Harvesting in Large Force Environments,” *J. Phys. Appl. Phys.*, vol. 50, no. 34, p. 345501, 2017, doi: 10.1088/1361-6463/aa7b28.
- [95] C. Sun, G. Shang, X. Zhu, Y. Tao, and Z. Li, “Modeling for piezoelectric stacks in series and parallel,” in *2013 Third International Conference on Intelligent System Design and Engineering Applications*, Jan. 2013, pp. 954–957, doi: 10.1109/ISDEA.2012.228.
- [96] L. Zhang, X. Xu, Q. Han, Z. Qin, and F. Chu, “Energy Harvesting of Beam Vibration Based on Piezoelectric Stacks,” *Smart Mater. Struct.*, vol. 28, no. 12, p. 125020, Nov. 2019, doi: 10.1088/1361-665X/ab4e09.
- [97] A. Keshmiri, X. Deng, and N. Wu, “New Energy Harvester with Embedded Piezoelectric Stacks,” *Compos. Part B Eng.*, vol. 163, pp. 303–313, Apr. 2019, doi: 10.1016/j.compositesb.2018.11.028.
- [98] Z. Shen, S. Liu, J. Miao, L. S. Woh, and Z. Wang, “Proof mass effects on spiral electrode d 33 mode piezoelectric diaphragm-based energy harvester,” in *2013 IEEE 26th International Conference on Micro Electro Mechanical Systems (MEMS)*, 2013, pp. 821–824.
- [99] W. Wang, R.-J. Huang, C.-J. Huang, and L.-F. Li, “Energy Harvester Array using Piezoelectric Circular Diaphragm for Rail Vibration,” *Acta Mech. Sin.*, vol. 30, no. 6, pp. 884–888, 2014.
- [100] Z. Shen, S. Liu, J. Miao, L. S. Woh, and Z. Wang, “Spiral Electrode d33 Mode Piezoelectric Diaphragm Combined with Proof Mass as Energy Harvester,” *J. Micromechanics Microengineering*, vol. 25, no. 3, p. 035004, 2015, doi: 10.1088/0960-1317/25/3/035004.

- [101] Y. Yang, S. Wang, P. Stein, B.-X. Xu, and T. Yang, "Vibration-Based Energy Harvesting with a Clamped Piezoelectric Circular Diaphragm: Analysis and Identification of Optimal Structural Parameters," *Smart Mater. Struct.*, vol. 26, no. 4, p. 045011, 2017, doi: 10.1088/1361-665x/aa5fda.
- [102] Y. Yang, Y. Li, Y. Guo, B.-X. Xu, and T. Yang, "Improved Vibration-Based Energy Harvesting by Annular Mass Configuration of Piezoelectric Circular Diaphragms," *Smart Mater. Struct.*, vol. 27, no. 3, p. 035004, 2018, doi:10.1088/1361-665x/aaa586.
- [103] L. Zhou *et al.*, "A Model for the Energy Harvesting Performance of Shear Mode Piezoelectric Cantilever," *Sens. Actuators Phys.*, vol. 179, pp. 185–192, Jun. 2012, doi: 10.1016/j.sna.2012.02.041.
- [104] M. H. Malakooti and H. A. Sodano, "Piezoelectric Energy Harvesting Through Shear Mode Operation," *Smart Mater. Struct.*, vol. 24, no. 5, p. 055005, 2015, <https://doi.org/10.1088/0964-1726/24/5/055005>.
- [105] V. Kulkarni, R. Ben-Mrad, S. E. Prasad, and S. Nemana, "A Shear-Mode Energy Harvesting Device Based on Torsional Stresses," *IEEEASME Trans. Mechatron.*, vol. 19, no. 3, pp. 801–807, 2013.
- [106] H. W. Kim, S. Priya, K. Uchino, and R. E. Newnham, "Piezoelectric Energy Harvesting under High Pre-Stressed Cyclic Vibrations," *J. Electroceramics*, vol. 15, no. 1, pp. 27–34, Sep. 2005, doi: 10.1007/s10832-005-0897-z.
- [107] T.-B. Xu *et al.*, "Energy Harvesting Using a PZT Ceramic Multilayer Stack," *Smart Mater. Struct.*, vol. 22, no. 6, p. 065015, 2013, <https://doi.org/10.1088/0964-1726/22/6/065015>.

- [108] X. Zhao, G. Zuo, and J. Chen, “Review on the Design, Geometry and Mechanical Modeling of Piezoelectric Energy Harvesting Structures,” *Arch. Curr. Res. Int.*, vol. 7, no. 4, pp. 1–22, Jan. 2017, doi: 10.9734/ACRI/2017/34019.
- [109] A. Erturk and D. J. Inman, *Piezoelectric Energy Harvesting*. John Wiley & Sons, 2011.
- [110] S. Roundy, P. K. Wright, and J. Rabaey, “A Study of Low Level Vibrations as a Power Source for Wireless Sensor Nodes,” *Comput. Commun.*, vol. 26, no. 11, pp. 1131–1144, Jul. 2003, doi: 10.1016/S0140-3664(02)00248-7.
- [111] G. Wang and Y. Lu, “An Improved Lumped Parameter Model for a Piezoelectric Energy Harvester in Transverse Vibration,” *Shock Vib.*, vol. 2014, p. 12, 2014, doi: 10.1155/2014/935298.
- [112] L. Mateu and F. Moll, “Optimum piezoelectric bending beam structures for energy harvesting using shoe inserts,” *J. Intell. Mater. Syst. Struct.*, vol. 16, no. 10, pp. 835–845, 2005, doi: 10.1177/1045389X05055280.
- [113] S. Paquin and Y. St-Amant, “Electromechanical performances of different shapes of piezoelectric energy harvesters,” in *Proceedings of the Cansmart 2009 International Workshop on Smart Materials and Structures*, 2009, pp. 187–196.
- [114] Z. S. Chen, Y. M. Yang, and G. Q. Deng, “Analytical and experimental study on vibration energy harvesting behaviors of piezoelectric cantilevers with different geometries,” in *2009 International Conference on Sustainable Power Generation and Supply*, 2009, pp. 1–6, doi: 10.1109/SUPERGEN.2009.5348290.
- [115] D. Benasciutti, L. Moro, S. Zelenika, and E. Brusa, “Vibration Energy Scavenging Via Piezoelectric Bimorphs of Optimized Shapes,” *Microsyst. Technol.*, vol. 16, no. 5, pp. 657–668, May 2010, doi: 10.1007/s00542-009-1000-5.

- [116] J. M. Dietl and E. Garcia, "Beam Shape Optimization for Power Harvesting," *J. Intell. Mater. Syst. Struct.*, vol. 21, no. 6, pp. 633–646, Apr. 2010, doi: 10.1177/1045389X10365094.
- [117] S. Ben Ayed, A. Abdelkefi, F. Najar, and M. R. Hajj, "Design and performance of variable-shaped piezoelectric energy harvesters," *J. Intell. Mater. Syst. Struct.*, vol. 25, no. 2, pp. 174–186, 2014.
- [118] M. Rosa and C. De Marqui Junior, "Modeling and Analysis of a Piezoelectric Energy Harvester with Varying Cross-Sectional Area," *Shock Vib.*, pp. 1–9, Jan. 2014, doi: 10.1155/2014/930503.
- [119] S. Kundu and H. B. Nemade, "Simulation of piezoelectric vibration energy harvester based on thickness-tapered cantilever," in *Proc COMSOL Conf Pune*, 2015, pp. 5–7.
- [120] A. G. A. Muthalif and N. H. D. Nordin, "Optimal Piezoelectric Beam Shape for Single and Broadband Vibration Energy Harvesting: Modeling, Simulation and Experimental Results," *Mech. Syst. Signal Process.*, vol. 54–55, pp. 417–426, Mar. 2015, doi: 10.1016/j.ymssp.2014.07.014.
- [121] C. K. Thein, B. L. Ooi, J.-S. Liu, and J. M. Gilbert, "Modelling and Optimisation of a Bimorph Piezoelectric Cantilever Beam in an Energy Harvesting Application," *J. Eng. Sci. Technol.*, vol. 11, no. 2, p. 212–227, 2016.
- [122] A. A. Sarafraz, S. Roknizadeh, and S. Alireza, "Shape and Geometrical Parameter Effects of a Bimorph Piezoelectric Beam on Energy Harvesting Performance," *J. Appl. Comput. Mech.*, vol. 3, no. 2, pp. 92–102, 2017, doi: 10.22055/JACM.2017.21610.1111.

- [123] S. S. Raju, M. Umopathy, and G. Uma, “High-Output Piezoelectric Energy Harvester Using Tapered Beam with Cavity,” *J. Intell. Mater. Syst. Struct.*, vol. 29, no. 5, pp. 800–815, 2018, doi: 10.1177/1045389X17721044.
- [124] N. Aboufotouh and J. Twiefel, “On Developing an Optimal Design Procedure for a Bimorph Piezoelectric Cantilever Energy Harvester Under a Predefined Volume,” *Mech. Syst. Signal Process.*, vol. 106, pp. 1–12, 2018.
- [125] R. Hosseini, O. Zargar, and M. Hamedi, “Improving Power Density of Piezoelectric Vibration-Based Energy Scavengers,” *J. Solid Mech.*, vol. 10, no. 1, pp. 98–109, 2018.
- [126] H. Salmani, G. H. Rahimi, and S. A. Hosseini Kordkheili, “An Exact Analytical Solution to Exponentially Tapered Piezoelectric Energy Harvester,” *Shock Vib.*, vol. 2015, Article ID 426876, 13 pages, 2015, doi: 10.1155/2015/426876.
- [127] O. Fakharian, H. Salmani, and S. A. H. Kordkheili, “A Lumped Parameter Model for Exponentially Tapered Piezoelectric Beam in Transverse Vibration,” *J. Mech. Sci. Technol.*, vol. 33, no. 5, pp. 2043–2048, May 2019, doi: 10.1007/s12206-019-0407-x.
- [128] G. K. Ottman, H. F. Hofmann, A. C. Bhatt, and G. A. Lesieutre, “Adaptive Piezoelectric Energy Harvesting Circuit for Wireless Remote Power Supply,” *IEEE Trans. Power Electron.*, vol. 17, no. 5, pp. 669–676, 2002.
- [129] G. K. Ottman, H. F. Hofmann, and G. A. Lesieutre, “Optimized piezoelectric energy harvesting circuit using step-down converter in discontinuous conduction mode,” *IEEE Trans. Power Electron.*, vol. 18, no. 2, pp. 696–703, 2003.



- [130] W. J. Wu and B. S. Lee, "Piezoelectric MEMS Power Generators for Vibration Energy Harvesting," *Small-Scale Energy Harvest.*, Oct. 2012, doi: 10.5772/51997.
- [131] E. Lefeuvre, A. Badel, C. Richard, and D. Guyomar, "Piezoelectric Energy Harvesting Device Optimization by Synchronous Electric Charge Extraction," *J. Intell. Mater. Syst. Struct.*, vol. 16, no. 10, pp. 865–876, Oct. 2005, doi: 10.1177/1045389X05056859.
- [132] K. Makihara, J. Onoda, and T. Miyakawa, "Low Energy Dissipation Electric Circuit for Energy Harvesting," *Smart Mater. Struct.*, vol. 15, no. 5, p. 1493, 2006, doi:10.1088/0964-1726/15/5/039.
- [133] J. Qiu, H. Jiang, H. Ji, and K. Zhu, "Comparison Between Four Piezoelectric Energy Harvesting Circuits," *Front. Mech. Eng. China*, vol. 4, no. 2, pp. 153–159, 2009.
- [134] J. H. Qiu, H. L. Ji, and H. Shen, "Energy harvesting and vibration control using piezoelectric elements and a nonlinear approach," in *2009 18th IEEE International Symposium on the Applications of Ferroelectrics*, 2009, pp. 1–8.
- [135] D. Guyomar, G. Sebald, S. Pruvost, M. Lallart, A. Khodayari, and C. Richard, "Energy Harvesting from Ambient Vibrations and Heat," *J. Intell. Mater. Syst. Struct.*, vol. 20, no. 5, pp. 609–624, Mar. 2009, doi: 10.1177/1045389X08096888.
- [136] E. Lefeuvre, A. Badel, C. Richard, L. Petit, and D. Guyomar, "A Comparison Between Several Vibration-Powered Piezoelectric Generators for Standalone Systems," *Sens. Actuators Phys.*, vol. 126, no. 2, pp. 405–416, 2006, doi: 10.1016/j.sna.2005.10.043.

- [137] E. Lefeuvre, A. Badel, C. Richard, and D. Guyomar, “High-Performance Piezoelectric Vibration Energy Reclamation,” in *Smart Structures and Materials 2004: Smart Structures and Integrated Systems*, vol. 5390, pp. 379–387, 2004, doi:10.1117/12.532709.
- [138] Y.-Y. Chen and D. Vasic, “Electrical Interfacing Circuit Discussion of Galloping-Based Piezoelectric Energy Harvester,” *Phys. Procedia*, vol. 70, pp. 1017–1021, 2015, doi: 10.1016/j.phpro.2015.08.212.
- [139] M. Lallart, L. Garbuio, L. Petit, C. Richard, and D. Guyomar, “Double Synchronized Switch Harvesting (DSSH): A new energy harvesting scheme for efficient energy extraction,” *IEEE Trans. Ultrason. Ferroelectr. Freq. Control*, vol. 55, no. 10, pp. 2119–2130, 2008, doi: 10.1109/tuffc.912.
- [140] A. D. Elliott and P. D. Mitcheson, “Implementation of a Single Supply pre-Biasing Circuit for Piezoelectric Energy Harvesters,” *Procedia Eng.*, vol. 47, pp. 1311–1314, 2012, doi:10.1016/j.proeng.2012.09.396.
- [141] F. Giusa, A. Giuffrida, C. Trigona, B. Andò, A. R. Bulsara, and S. Baglio, “‘Random Mechanical Switching Harvesting on Inductor’: A novel approach to collect and store energy from weak random vibrations with zero voltage threshold,” *Sens. Actuators Phys.*, vol. 198, pp. 35–45, Aug. 2013, doi: 10.1016/j.sna.2013.04.018.
- [142] T. Starner, “Human-Powered Wearable Computing,” *IBM Syst. J.*, vol. 35, no. 3.4, pp. 618–629, 1996, doi:10.1147/sj.353.0618.
- [143] S. Khalifa, G. Lan, M. Hassan, A. Seneviratne, and S. K. Das, “Harke: Human Activity Recognition from Kinetic Energy Harvesting Data in Wearable Devices,” *IEEE Trans. Mob. Comput.*, vol. 17, no. 6, pp. 1353–1368, 2017, doi:10.1109/tmc.2017.2761744.

- [144] N. S. Shenck and J. A. Paradiso, “Energy Scavenging with Shoe-Mounted Piezoelectrics,” *IEEE Micro*, vol. 21, no. 3, pp. 30–42, May 2001, doi: 10.1109/40.928763.
- [145] K. Ishida *et al.*, “Insole Pedometer with Piezoelectric Energy Harvester and 2 V Organic Circuits,” *IEEE J. Solid-State Circuits*, vol. 48, no. 1, pp. 255–264, Jan. 2013, doi: 10.1109/JSSC.2012.2221253.
- [146] Y. Han *et al.*, “A Self-Powered Insole for Human Motion Recognition,” *Sensors*, vol. 16, no. 9, p. 1502, 2016, doi: 10.3390/s16091502.
- [147] J. Zhao and Z. You, “A shoe-embedded piezoelectric energy harvester for wearable sensors,” *Sensors*, vol. 14, no. 7, pp. 12497–12510, 2014, doi: 10.3390/s140712497.
- [148] L. Xie and M. Cai, “Increased Piezoelectric Energy Harvesting from Human Footstep Motion by Using an Amplification Mechanism,” *Appl. Phys. Lett.*, vol. 105, no. 14, p. 143901, Oct. 2014, doi: 10.1063/1.4897624.
- [149] M. Pozzi, M. S. H. Aung, M. Zhu, R. K. Jones, and J. Y. Goulermas, “The Pizzicato Knee-Joint Energy Harvester: Characterization with Biomechanical Data and the Effect of Backpack Load,” *Smart Mater. Struct.*, vol. 21, no. 7, p. 075023, Jul. 2012, doi: 10.1088/0964-1726/21/7/075023.
- [150] Y. Kuang, Z. Yang, and M. Zhu, “Design and Characterisation of a Piezoelectric Knee-joint Energy Harvester with Frequency Up-conversion Through Magnetic Plucking,” *Smart Mater. Struct.*, vol. 25, no. 8, p. 085029, Aug. 2016, doi: 10.1088/0964-1726/25/8/085029.

- [151] J. Granstrom, J. Feenstra, H. A. Sodano, and K. Farinholt, “Energy Harvesting from a Backpack Instrumented with Piezoelectric Shoulder Straps,” *Smart Mater. Struct.*, vol. 16, no. 5, pp. 1810–1820, Sep. 2007, doi: 10.1088/0964-1726/16/5/036.
- [152] J. Feenstra, J. Granstrom, and H. Sodano, “Energy Harvesting Through a Backpack Employing a Mechanically Amplified Piezoelectric Stack,” *Mech. Syst. Signal Process.*, vol. 22, no. 3, pp. 721–734, Apr. 2008, doi: 10.1016/j.ymsp.2007.09.015.
- [153] H. Zhang *et al.*, “A Flexible and Implantable Piezoelectric Generator Harvesting Energy From the Pulsation of Ascending Aorta: in Vitro and in Vivo Studies,” *Nano Energy*, vol. 12, pp. 296–304, Mar. 2015, doi: 10.1016/j.nanoen.2014.12.038.
- [154] M. Peigney and D. Siegert, “Piezoelectric Energy Harvesting from Traffic-induced Bridge Vibrations,” *Smart Mater. Struct.*, vol. 22, no. 9, p. 095019, Sep. 2013, doi: 10.1088/0964-1726/22/9/095019.
- [155] I. Jung, Y.-H. Shin, S. Kim, J. Choi, and C.-Y. Kang, “Flexible Piezoelectric Polymer-based Energy Harvesting System for Roadway Applications,” *Appl. Energy*, vol. 197, pp. 222–229, Jul. 2017, doi: 10.1016/j.apenergy.2017.04.020.
- [156] Z. Zhang, H. Xiang, Z. Shi, and J. Zhan, “Experimental Investigation on Piezoelectric Energy Harvesting from Vehicle-bridge Coupling Vibration,” *Energy Convers. Manag.*, vol. 163, pp. 169–179, May 2018, doi: 10.1016/j.enconman.2018.02.054.

- [157] G. Gatti, M. J. Brennan, M. G. Tehrani, and D. J. Thompson, “Harvesting Energy from the Vibration of a Passing Train Using a Single-Degree-of-Freedom Oscillator,” *Mech. Syst. Signal Process.*, vol. 66–67, pp. 785–792, Jan. 2016, doi: 10.1016/j.ymssp.2015.06.026.
- [158] M. R. Pearson et al., “Energy Harvesting for Aerospace Structural Health Monitoring Systems,” *J. Phys. Conf. Ser.*, vol. 382, p. 012025, Aug. 2012, doi: 10.1088/1742-6596/382/1/012025.
- [159] N. Wu, Q. Wang, and X. Xie, “Ocean Wave Energy Harvesting With a Piezoelectric Coupled Buoy Structure,” *Appl. Ocean Res.*, vol. 50, pp. 110–118, Mar. 2015, doi: 10.1016/j.apor.2015.01.004.
- [160] “Piezoelectric Bending Transducer (Q220-H4BR-1305YB),” *PIEZO.COM*. <https://piezo.com/products/piezoelectric-bending-transducer-q220-h4br-1305yb> (accessed Sep. 30, 2020).
- [161] S. Rao, *Mechanical Vibrations*, 5th ed. Pearson Education, 2011.
- [162] S. Abrate, “Vibration of Non-uniform Rods and Beams,” *J. Sound Vib.*, vol. 185, no. 4, pp. 703–716, 1995.
- [163] J.-S. Wu and M. Hsieh, “Free Vibration Analysis of a Non-Uniform Beam with Multiple Point Masses,” *Struct. Eng. Mech.*, vol. 9, no. 5, pp. 449–467, May 2000, doi: 10.12989/sem.2000.9.5.449.
- [164] T. S. Ramadoss, H. Alam, and R. Seeram, “Profile Geometric Effect of Cantilever Piezoelectric Device using Flexural Mechanism,” *IJNTR*, vol. 4, no. 9, pp. 39–42, 2018.
- [165] “Material Properties - Piezo Support.” <https://support.piezo.com/article/62-material-properties> (accessed Oct. 26, 2020).

### List of Publications

- [1] M. R. Ismail, F. K. Omar, R. Ajaj and M. Ghodsi, "On the Accuracy of Lumped Parameter Model for Tapered Cantilever Piezoelectric Energy Harvesters with Tip Mass," 2020 Advances in Science and Engineering Technology International Conferences (ASET), Dubai, United Arab Emirates, 2020, pp. 1-6, doi: 10.1109/ASET48392.2020.9118273.
- [2] M. R. Ismail, F. K. Omar, R. Ajaj, and M. Ghodsi, "Correction factor of lumped parameter model for linearly tapered piezoelectric cantilever," Journal of Intelligent Material Systems and Structures, p. 1045389X211018840, 2021, doi: 10.1177/1045389X211018840.